

# Non-classical effects in wave packet dynamics

*A THESIS*

*submitted by*

**C. SUDHEESH**

*for the award of the degree*

*of*

**DOCTOR OF PHILOSOPHY**



**DEPARTMENT OF PHYSICS  
INDIAN INSTITUTE OF TECHNOLOGY MADRAS**

**December 2005**

# THESIS CERTIFICATE

This is to certify that the thesis titled **Non-classical effects in wave packet dynamics**, submitted by **C. Sudheesh** to the Indian Institute of Technology Madras for the award of the degree of **Doctor of Philosophy**, is a bona fide record of the research work done by him under our supervision. The contents of this thesis, in full or in part, have not been submitted to any other Institute or University for the award of any degree or diploma.

**S. Lakshmi Bala**  
Research Guide

Associate Professor  
Dept. of Physics  
IIT Madras

**V. Balakrishnan**  
Research Guide

Professor  
Dept. of Physics  
IIT Madras

Place: Chennai 600 036, India

Date: 26 December 2005

## ACKNOWLEDGMENTS

I take this opportunity to express my sincere gratitude to my principal supervisor, Dr. S. Lakshmi Bala, although a few words cannot do justice to the pivotal role she has had in my life as a graduate student. Her commitment, hard work and attention to detail have set an example I hope to match some day. I have benefited immensely from her encouraging support and constructive criticism. I am greatly indebted to my second supervisor, Dr. V. Balakrishnan, for insightful comments and valuable discussions throughout the course of my doctoral research. His dedication, excellence in teaching, and exemplary academic standards have always inspired me to strive hard for perfection.

Special words of appreciation go to Dr. Suresh Govindarajan and Dr. M. V. Satyanarayana for their constant encouragement and useful discussions. I would also like to thank the other members of my doctoral committee, Dr. S. G. Kamath and Dr. K. Mangala Sunder, for their efforts in reviewing and commenting on this work. My thanks also go to Dr. Neelima Gupte, Dr. Arul Lakshminarayan, Dr. M. S. Sriram and Dr. Radha Balakrishnan for their help and discussions.

It is a pleasure to thank Dr. A. Subrahmanyam, Head of the Department of Physics, and Dr. V. R. K. Murthy, former Head of the Department of Physics, for their kind help and advice whenever I needed these. I am thankful to Dr. V. G. Idichandy, Dean (Students), for taking necessary steps when I had health-related problems.

I would like to thank my parents and my uncles, Mr. P. Asokan and Mr. P. Gangadharan, for love, support and encouragement.

I am grateful to Aji, Shajahan and Vinu for providing useful reference material. I would like to extend my thanks to all my friends and colleagues for valuable discussions and timely help — in particular, Ranjith, Hari Varma, Subeesh, Raghu,

Sree Ranjani, Madhu, Zahera, Tanima, Meenakshi, Basheer, Pramod, Sandeep and Sanoop. Special thanks go to Sreejith, whom I am fortunate to have as a friend, and who has always been with me in my ups and downs since my college days.

I am grateful to IIT Madras for financial support in the form of a Research Assistantship during the course of my doctoral research.

The work presented here was supported in part by the Department of Science and Technology, India, under Project No. SP/S2/K-14/2000.

# ABSTRACT

**Keywords:** Wave packets; Kerr medium; revivals; fractional revivals; coherent states; photon-added coherent states; expectation values; higher moments; squeezing; Wigner function; entropy; entanglement; time series; Lyapunov exponent.

Starting with an initial wave packet that corresponds to an ideal coherent state, we show that, in the framework of a generic Hamiltonian that models the propagation of a single-mode electromagnetic field in a Kerr-like medium, distinctive signatures of wave packet revivals and fractional revivals are displayed by the time evolution of the expectation values and cumulants of appropriate observables. This enables selective identification of different fractional revivals. Using a class of photon-added coherent states as the initial states, we further show that the revival phenomena provide clear signatures of the extent of the departure from coherence, and of the deviation from Poissonian photon number statistics, of the initial state of the radiation field. A comparison is also made of the manner in which other non-classical effects are displayed as the wave packet evolves, in the cases of an initial photon-added coherent state and an initial ideal coherent state, respectively. These effects comprise squeezing, higher-order squeezing, and the non-positivity of the Wigner function.

Extending these studies to the case of two interacting modes, we consider another generic Hamiltonian that models the interaction of a single-mode electromagnetic field propagating in a nonlinear medium, an atom of which is modeled by an anharmonic oscillator. The dynamics of expectation values and higher moments of observables pertaining to the field sub-system as well as the total system are studied over a range of values of a relevant parameter, namely, the ratio of the strength of the anharmonicity to that of the inter-mode coupling. Analogs of revival phenomena are found, and their signatures identified in quantifiers such

as sub-system entropies that serve to characterize the degree of entanglement. A time series analysis of the mean photon number (or, equivalently, the mean energy of the field mode) is carried out, to deduce the embedding dimension of the reconstructed phase space and the maximal Lyapunov exponent. The corresponding dynamical behavior is found to range from mere ergodicity (as in quasi-periodicity) to exponential instability characterized by a positive maximal Lyapunov exponent, as the parameter ratio mentioned above is varied.

Our results shed light on the non-classical effects that occur during the propagation of a quantum mechanical wave packet in a nonlinear medium. Several avenues for further research are also revealed.

# TABLE OF CONTENTS

ACKNOWLEDGMENTS	i
ABSTRACT	iii
LIST OF FIGURES	ix
GLOSSARY OF SYMBOLS	x
<b>1 Introduction</b>	<b>1</b>
<b>2 Manifestations of wave packet revivals in the moments of observables - I</b>	<b>11</b>
2.1 Introduction . . . . .	11
2.2 Revivals and fractional revivals in wave packet dynamics . . . . .	11
2.3 Signatures of revivals and fractional revivals in quantum expectation values . . . . .	15
2.4 Moments of $x$ and $p$ : A classical interpretation . . . . .	18
2.5 Signatures of fractional revivals . . . . .	19
2.6 Concluding remarks . . . . .	25
<b>3 Manifestations of wave packet revivals in the moments of observables - II</b>	<b>27</b>
3.1 Introduction . . . . .	27
3.2 Dynamics of photon-added coherent states propagating in a non-linear medium . . . . .	29
3.3 Concluding remarks . . . . .	36
<b>4 Squeezing and higher-order squeezing in wave packet dynamics</b>	<b>39</b>
4.1 Introduction . . . . .	39
4.2 The case of an initial coherent state . . . . .	42
4.3 The case of an initial PACS . . . . .	44

4.4	The Wigner function and the non-classicality indicator . . . . .	48
4.5	Concluding remarks . . . . .	55
<b>5</b>	<b>Ergodicity properties of entangled two-mode states - I</b>	<b>57</b>
5.1	Introduction . . . . .	57
5.2	Single-mode field in a nonlinear medium: The model . . . . .	59
5.3	Entanglement properties . . . . .	62
5.4	Concluding remarks . . . . .	73
<b>6</b>	<b>Ergodicity properties of entangled two-mode states - II</b>	<b>74</b>
6.1	Properties of the coupled-system Hamiltonian . . . . .	74
6.2	Time-series analysis in brief . . . . .	78
6.3	Ergodicity properties of the mean photon number . . . . .	81
<b>7</b>	<b>Conclusion</b>	<b>90</b>
	<b>Appendices</b>	<b>92</b>
<b>A</b>	<b>Calculation of <math>\langle a^{\dagger r} a^{r+s} \rangle</math> for an initial PACS <math> \alpha, m\rangle</math> propagating in a Kerr-like medium</b>	<b>93</b>
<b>B</b>	<b>Analytic expressions for <math>\langle x(t) \rangle</math> and <math>\langle p(t) \rangle</math> for an initial PACS</b>	<b>96</b>
<b>C</b>	<b>Calculation of <math>D_q^{(m)}(t)</math> for an initial PACS <math> \alpha, m\rangle</math></b>	<b>99</b>
<b>D</b>	<b>Density matrix for a field mode interacting with a nonlinear medium</b>	<b>101</b>
	Bibliography . . . . .	106



## LIST OF FIGURES

2.1	$\langle x \rangle$ as a function of time . . . . .	20
2.2	“Phase plot” of $\langle p \rangle$ versus $\langle x \rangle$ . . . . .	21
2.3	Variation of the uncertainty product with time . . . . .	22
2.4	“Phase plot” of $\Delta p$ versus $\Delta x$ for $\nu = 1, 10$ and $100$ , respectively. . . . .	22
2.5	Square of the skewness in $x$ as a function of time . . . . .	23
2.6	The “phase plot” of $\beta_1^{(p)}$ versus $\beta_1^{(x)}$ . . . . .	23
2.7	The excess of kurtosis of $x$ as a function of time . . . . .	24
2.8	“Phase plot” of $(\beta_2^{(p)} - 3)$ versus $(\beta_2^{(x)} - 3)$ . . . . .	24
3.1	$(\langle N \rangle_m - \nu)$ versus $\nu$ for $m = 1, 3$ and $5$ . . . . .	28
3.2	Probability of single-photon content versus $\nu$ in a CS ( $m = 0$ ) and in a 1-photon-added CS ( $m = 1$ ). . . . .	29
3.3	$\langle x(t) \rangle$ as a function of $t/T_{\text{rev}}$ for a PACS (a) $ \alpha, 1\rangle$ and (b) $ \alpha, 10\rangle$ , with $\nu = 1$ . . . . .	32
3.4	“Phase plot” of $\langle p \rangle$ vs $\langle x \rangle$ for an initial PACS (a) $ \alpha, 1\rangle$ and (b) $ \alpha, 10\rangle$ , with $\nu = 1$ . . . . .	33
3.5	Phase distribution $P(\phi)$ versus $\phi$ in units of $\pi$ , for $\nu = 0.3$ and $m = 0, 1$ and $10$ . . . . .	33
3.6	Variation of the uncertainty product with $t/T_{\text{rev}}$ for an initial CS ( $m = 0$ ) and initial PACS $ \alpha, 1\rangle$ and $ \alpha, 10\rangle$ with $\nu = 1$ . . . . .	34
3.7	“Phase plots” of $\Delta p$ and $\Delta x$ for $\nu = 1$ , for an initial CS ( $m = 0$ ) and an initial PACS $ \alpha, 5\rangle$ . . . . .	35
3.8	“Phase plots” of $\langle (\delta p)^4 \rangle$ and $\langle (\delta x)^4 \rangle$ for $\nu = 1$ , for an initial CS and an initial PACS $ \alpha, 2\rangle$ . . . . .	37
4.1	$D_q(\frac{1}{2}T_{\text{rev}})$ versus $\nu$ for an initial CS (with $\theta = 0$ ), for (a) $q = 1$ and (b) $q = 3$ . (Note the different ordinate scales in the two cases.) . . . . .	43
4.2	$D_q(\frac{1}{2}T_{\text{rev}})$ versus $\theta$ for an initial CS (with $\nu = 0.1$ ), for (a) $q = 1$ and (b) $q = 3$ . . . . .	43
4.3	$D_q$ versus $t/T_{\text{rev}}$ for an initial CS with $\nu = 10$ , for $q = 1, 2, 3$ and $4$ . . . . .	44

4.4	$D_2^{(m)}(\frac{1}{2}T_{\text{rev}})$ versus $\nu$ (with $\theta = 0$ ), for an initial PACS with (a) $m = 1$ and (b) $m = 10$ . . . . .	46
4.5	$D_2^{(m)}(\frac{1}{2}T_{\text{rev}})$ versus $\theta$ (with $\nu = 2$ ), for an initial PACS with (a) $m = 1$ and (b) $m = 10$ . . . . .	46
4.6	$\Delta x$ versus time in units of $T_{\text{rev}}$ , in the case $x_0 = \sqrt{2}$ , $p_0 = 0$ . . .	47
4.7	$D_q^{(m)}$ versus $t/T_{\text{rev}}$ for an initial PACS (a) $ \alpha, 1\rangle$ and (b) $ \alpha, 5\rangle$ , with $\nu = 10$ , for $q = 1, 2, 3$ and $4$ . . . . .	48
4.8	$\langle(\delta x)^4\rangle$ versus time in units of $T_{\text{rev}}$ for initial states (a) $ \alpha\rangle$ and (b) $ \alpha, 5\rangle$ , with $\nu = 1$ . Note the very different ordinate scales in the two cases. Hong-Mandel squeezing in $x$ occurs below the dotted horizontal line. . . . .	49
4.9	Wigner function corresponding to an initial state $ \alpha\rangle$ with $\alpha = 1$ , at (a) $t = \frac{1}{2}T_{\text{rev}}$ and (b) $t = \frac{1}{3}T_{\text{rev}}$ . Here, and in the succeeding figures, $\beta_1 = \text{Re } \beta$ , $\beta_2 = \text{Im } \beta$ . . . . .	52
4.10	Wigner function corresponding to an initial state $ \alpha, 1\rangle$ with $\alpha = 1$ , at (a) $t = 0$ , (b) $t = \frac{1}{2}T_{\text{rev}}$ and (c) $t = \frac{1}{3}T_{\text{rev}}$ . . . . .	53
4.11	Wigner function corresponding to an initial state $ \alpha, 10\rangle$ with $\alpha = 1$ , at (a) $t = 0$ , (b) $t = \frac{1}{2}T_{\text{rev}}$ and (c) $t = \frac{1}{3}T_{\text{rev}}$ . . . . .	54
4.12	Non-classicality indicator $\delta$ versus time in units of $T_{\text{rev}}$ , for initial states $ \alpha, m\rangle$ with $\alpha = 1$ . . . . .	55
5.1	SVNE and SLE versus $gt$ for (a) an initial Fock state $ 10; 0\rangle$ , and (b) an initial coherent state $ \alpha; 0\rangle$ with $\nu = 1$ . The ratio $\gamma/g = 10^{-2}$ in Figs. 5.1 through 5.11. . . . .	64
5.2	SVNE and SLE versus $gt$ for an initial state $ (\alpha, 5); 0\rangle$ for (a) $\nu = 1$ and (b) $\nu = 5$ . . . . .	65
5.3	$\langle\xi\rangle$ versus $gt$ for an initial state $ \alpha; 0\rangle$ with (a) $\nu = 1$ and (b) $\nu = 5$ , respectively. . . . .	67
5.4	$\langle\xi\rangle$ versus $gt$ for an initial state $ (\alpha, 1); 0\rangle$ with $\nu = 1$ . . . . .	68
5.5	$\Delta\xi$ versus $gt$ for an initial state $ 10; 0\rangle$ . . . . .	69
5.6	$\Delta\xi$ versus $gt$ for an initial state $ (\alpha, m); 0\rangle$ with $\nu = 1$ and $m = 0, 1$ and $5$ , respectively. . . . .	69
5.7	$D_2^{(N)}$ versus $gt$ for an initial state $ N; 0\rangle$ with $N = 10$ . . . . .	71
5.8	$D_2^{(m)}$ versus $gt$ for an initial state $ \alpha; 0\rangle$ and $ (\alpha, 1); 0\rangle$ with $\nu = 1$ . . . . .	71
5.9	$\langle(\delta\xi)^3\rangle$ versus $gt$ for an initial state (a) $ \alpha; 0\rangle$ (b) $ (\alpha, 3); 0\rangle$ with $\nu = 1$ and $\gamma/g = 10^{-2}$ . . . . .	72
5.10	$\langle(\delta\xi)^3\rangle$ versus $gt$ for an initial state $ \alpha; 0\rangle$ with $\nu = 5$ . . . . .	72

5.11	$\Delta x_a$ versus $gt$ for an initial state $ \alpha; 0\rangle$ with $\nu = 5$ . . . . .	73
6.1	Power spectrum of the mean photon number for the initial states (a) $ \alpha; 0\rangle$ and (b) $ (\alpha, 5); 0\rangle$ with $\gamma/g = 10^{-2}$ and $\nu = 1$ . . . . .	82
6.2	Power spectrum of $\langle N \rangle$ for an initial state $ (\alpha, 5); 0\rangle$ with $\gamma/g = 10^{-2}$ and $\nu = 5$ . . . . .	83
6.3	$\langle \ln d_j(k) \rangle$ versus $t = k \delta t$ for an initial state $ (\alpha, 5); 0\rangle$ with $\gamma/g = 5$ and $\nu = 1$ . The solid line corresponds to $d_{\text{emb}} = 5$ . The dotted lines correspond to values of $d_{\text{emb}}$ from 6 to 10. . . . .	84
6.4	$\langle \ln d_j(k) \rangle$ versus $t$ for an initial state $ (\alpha, 1); 0\rangle$ with $\gamma/g = 5$ and $\nu = 5$ . The solid line corresponds to embedding dimension equal to 5. The dotted lines correspond to values of $d_{\text{emb}}$ from 6 to 10. . . . .	85
6.5	$\langle \ln d_j(k) \rangle$ versus $t$ for an initial state $ (\alpha, 5); 0\rangle$ with $\gamma/g = 5$ and $\nu = 5$ . The solid line corresponds to $d_{\text{emb}} = 6$ . The dotted lines correspond to values of $d_{\text{emb}}$ from 7 to 10. . . . .	85
6.6	$\langle \ln d_j(k) \rangle$ versus $t$ for an initial state $ \alpha; 0\rangle$ with $\gamma/g = 5$ and $\nu = 10$ . The solid line corresponds to embedding dimension equal to 5. The dotted lines correspond to values of $d_{\text{emb}}$ from 6 to 10. . . . .	86

## GLOSSARY OF SYMBOLS

$H$	Hamiltonian
$a, a^\dagger$	ladder operators for a single-mode electromagnetic field
$\mathbf{N}$	photon number operator $a^\dagger a$
$ n\rangle$	a Fock state
$x, p$	$(a + a^\dagger)/\sqrt{2}$ , $(a - a^\dagger)/i\sqrt{2}$
$\chi$	characteristic frequency parameter in the Hamiltonian
$T_{\text{rev}}$	revival time
$ \alpha\rangle$	coherent state (CS) of a single-mode electromagnetic field
$\alpha$	complex number labeling a CS
$\nu$	$ \alpha ^2$
$\theta$	argument of $\alpha$ ( $= \nu^{1/2} e^{i\theta}$ )
$\tau$	$\sin(2\chi t)$ (in Chapter 2)
$\delta x$	$x - \langle x \rangle$ (similarly, $\delta p$ )
$\Delta x$	variance of $x$ (similarly, $\Delta p$ )
$\beta_1^{(x)}$	square of the skewness in $x$ (similarly, $\beta_1^{(p)}$ )
$\beta_2^{(x)}$	kurtosis in $x$ (similarly, $\beta_2^{(p)}$ )
$ \alpha, m\rangle$	$m$ -photon-added coherent state (PACS)
$\langle \mathbf{N} \rangle$	mean photon number in a given state
$\langle \mathbf{N} \rangle_m$	mean photon number in the PACS $ \alpha, m\rangle$
$L_m$	Laguerre polynomial of order $m$
$L_m^s$	associated Laguerre polynomial
$ \phi\rangle$	$\sum_{n=0}^{\infty} e^{in\phi}  n\rangle$
$P(\phi)$	phase distribution function
$A_\varphi$	$(ae^{i\varphi} + a^\dagger e^{-i\varphi})/\sqrt{2}$
$B_\varphi$	$(ae^{i\varphi} - a^\dagger e^{-i\varphi})/(i\sqrt{2})$
$q$	a non-negative integer
$Z_1$	$(a^q + a^{\dagger q})/\sqrt{2}$ or $(a^q + a^{\dagger q} + b^q + b^{\dagger q})/(2\sqrt{2})$

$Z_2$	$(a^q - a^{\dagger q})/(i\sqrt{2})$ or $(a^q - a^{\dagger q} + b^q - b^{\dagger q})/(2i\sqrt{2})$
$F_q(\mathbf{N})$	$[a^q, a^{\dagger q}]$ , a polynomial of order $(q - 1)$ in $\mathbf{N}$
$D_q(t)$	a measure of $q^{\text{th}}$ -power amplitude squeezing
$D_q^{(m)}(t)$	$D_q(t)$ for an initial PACS $ \alpha, m\rangle$
$\beta$	a complex number
$W(\beta; t)$	Wigner function
$\delta$	non-classicality indicator $\int d^2\beta  W(\beta; t)  - 1$
$\rho(t)$	density matrix
$\rho_{nl}(t)$	density matrix element
$b, b^\dagger$	ladder operators for an atomic oscillator modeling the nonlinear medium
$\mathbf{N}_{\text{tot}}$	total number operator $a^\dagger a + b^\dagger b$
$\gamma$	anharmonicity parameter in the two-mode Hamiltonian
$g$	coupling constant in the two-mode Hamiltonian
$\lambda$	limiting value of $\gamma/\hbar$ in the classical limit
$H_{\text{cl}}$	Hamiltonian in the classical limit
$N_{\text{cl}}$	second constant of the motion in the classical system
$\rho_k(t)$	reduced density matrix for a sub-system
$\lambda_k^{(i)}(t)$	eigenvalue of the reduced density matrix $\rho_k(t)$
$S_k(t)$	sub-system von Neumann entropy (SVNE)
$\delta_k(t)$	sub-system linear entropy (SLE)
$\xi, \eta$	quadrature variables for the coupled two-mode system
$\delta t$	time step for time series analysis
$\tau$	delay time in time series analysis (in Chapter 6)
$d_{\text{emb}}$	embedding dimension (dimensionality of reconstructed phase space)
$S(f)$	power spectrum at frequency $f$
$d_j(k)$	distance between $j^{\text{th}}$ pair of nearest-neighbor points at time $k \delta t$
$\lambda_{\text{max}}$	maximal Lyapunov exponent

# CHAPTER 1

## Introduction

The long-time behavior of classical dynamical systems, and the degree of randomness they exhibit (ranging from mere ergodicity to fully-developed chaos), have been investigated extensively in the literature. They continue to be subjects of abiding interest and current research. Ergodicity theorems of wide applicability ensure that, generically, the dynamics is metrically transitive — either on the energy surface, in conservative (Hamiltonian) systems, or on some attractor, in dissipative systems. While the evolution equations for the dynamical variables describing the behavior of a classically chaotic system are necessarily nonlinear, the corresponding quantum dynamics is governed by the Schrödinger equation (or, in the more general case of mixed states, by the Liouville equation), which is inherently linear. It is not straightforward, therefore, to assess the extent of randomness in a quantum system, or the precise manner in which the information content of a quantum system changes with time.

At least two different approaches have been employed in identifying signatures of the nature of the ergodicity of the quantum mechanical counterpart of a generic classical system [1]. One approach relies on the observation that such signatures are generally manifested in the statistics of the energy levels of the corresponding quantum system. If the system is classically integrable, the quantum levels cluster together, and could even cross when a specific parameter in the Hamiltonian is varied [2]. A classically chaotic system, on the other hand, has its corresponding quantum energy levels so correlated as to resist such crossings [3, 4]. Another approach is based on investigating the dynamics of the overlap between two quantum states of the same physical system which originate from the same initial state, but with *slightly* different values of one of the control parameters [5]. The time-dependent overlap is close to unity at all times if the normalized initial state is located in a classically regular region of phase space. In contrast, if the initial state

is in a chaotic region of the classical phase space, the overlap falls off exponentially in time.

The foregoing lines of investigation concern quantum signatures of classical dynamics. The inverse problem, namely, the identification of signatures of non-classical effects in the temporal behavior of quantum mechanical expectation values (which, in turn, could be regarded as effective classical dynamical variables in an appropriate phase space), has also received attention. The dynamics of a quantum wave packet governed by a nonlinear Hamiltonian provides adequate scope for such an investigation to be carried out, as a wide variety of non-classical effects such as revivals and fractional revivals (for reviews see, e. g., [6, 7, 8]), as well as squeezing (for a review see, e. g., [9]), are displayed by the wave packet as it evolves in time.

While a generic initial wave packet (corresponding to the state  $|\psi(0)\rangle$ ) governed by a nonlinear Hamiltonian spreads rapidly during its evolution, it could return to its original state (apart from an overall phase) at integer multiples of a revival time  $T_{\text{rev}}$ , under certain conditions. This is signaled by the return of  $|\langle\psi(0)|\psi(t)\rangle|^2$  to its initial value of unity at  $t = nT_{\text{rev}}$ . The role played by the non-quadratic terms in the quantum Hamiltonian on the dynamics of a wave packet as it spreads and loses its original shape is best understood by examining the dynamics of appropriate expectation values and the consequences of Ehrenfest's theorem. Consider the simple one-dimensional example of a particle of mass  $m$  subject to a potential  $V(x)$ . The Hamiltonian is

$$H = \frac{p^2}{2m} + V(x), \quad (1.1)$$

where  $x$  is the position operator and  $p$  is the momentum operator. Ehrenfest's theorem states that

$$\frac{d\langle x \rangle}{dt} = \frac{\langle p \rangle}{m}, \quad (1.2)$$

$$\frac{d\langle p \rangle}{dt} = - \left\langle \frac{\partial V(x)}{\partial x} \right\rangle. \quad (1.3)$$

For quadratic Hamiltonians, the latter equation gets simplified to

$$\frac{d\langle p \rangle}{dt} = -\frac{\partial V(\langle x \rangle)}{\partial x}. \quad (1.4)$$

Correspondingly, these expectation values follow the classical motion. For non-quadratic Hamiltonians, (approximate) classical motion arises only if the potential can be approximated to the quadratic form. In fact, certain techniques for the semi-classical treatment of the propagation of wave packets [10, 11] are based on the replacement of the exact Hamiltonian with a tractable, usually quadratic, approximation governing the evolution of the wave packet. Further, the quadratic potential turns out to be the most general potential under which a Gaussian wave packet continues to remain a Gaussian. In fact, there is an interesting parallel [12] between the following two situations: The quadratic approximation given in Eq. (1.4), and the retention of the Gaussian shape under a quadratic potential, on the one hand; and the role of the second-order term in a series expansion for the classical Hamiltonian in the linearized behavior of classical orbits close to some reference orbit in phase space, on the other.

The eventual spreading of a generic wave packet (which could initially follow classical motion for a brief period of time) is inevitable if a quadratic approximation does not hold good. It has been argued [12] that such wave packet spreading in both position and momentum space should also be describable in a classical framework by considering an ensemble of nearby classical orbits. Despite the spreading phenomenon, interesting quantum interference phenomena [13] can lead not only to wave packet revivals, but also to fractional revivals between two successive revivals at specific instants. The latter is characterized by the splitting up of the initial wave packet into a number of spatially distributed sub-packets, each of which is similar to the original wave packet. Classical analogs of revival phenomena can also be envisaged. For instance, one can model the individual energy eigenstates comprising the wave packet as an ensemble of racing cars on a circular track with different speeds [14]. The quantum mechanical spreading of the wave packet arises due to the difference in speeds. However, certain distinct time scales appear in the problem: The initial classical periodicity may be retained for



a few laps, while for longer times no correlations between the various racers are observed — but obvious patterns can recur, including the original form (revivals), as well as small similar groups of racers clumped together at certain instants (fractional revivals). Another interesting analogy exists between wave packet revivals (in *time*) and the recurrence of images (in *space*) in the classical Talbot effect. This is the repeated self-imaging of a diffraction grating at multiples of a certain fundamental distance from the source due to coherent interference of waves, akin to quantum revivals of a wave packet at multiples of the fundamental time  $T_{\text{rev}}$ . Further, in between the appearance of two such self-images, Talbot images (which are superposed copies of the original) appear at definite spatial positions, akin to fractional revivals of the quantum wave packet at certain instants between two successive revivals (see, for instance, [15, 16]).

In this thesis, we focus on the quantum revival phenomena and other non-classical effects that arise close to instants of revivals and fractional revivals, and the information that can be obtained about these effects by examining the expectation values and higher moments (or cumulants) of operators corresponding to appropriately chosen observables. It is evident that, at full revivals of any initial state, the expectation values of all observables return to their initial values. Thus, in a “phase space” where these expectation values play the role of classical dynamical variables, the trajectories are closed orbits, indicative of the regular temporal evolution of the corresponding dynamical system. In principle, such a classical phase space would be infinite-dimensional, because the full information contained in a specific quantum state can only be obtained if the expectation values and all the higher moments of all operators pertaining to the system are included in the set of dynamical variables. A more practicable approach, however, is to use the time series of an available set of expectation values pertaining to the system, in order to estimate the embedding dimension of the relevant phase space, as is done when carrying out a time-series analysis to determine the extent of randomness of a given set of signals.

Interesting signatures of different fractional revivals also manifest themselves in the dynamics of the expectation values of various operators. For one-dimensional

systems with Hamiltonians that can be written in the form given in Eq.(1.1), the Ehrenfest equations can be generalized to include the temporal evolution of the second moments of  $x$  and  $p$ . These are given by

$$\frac{d\langle x^2 \rangle}{dt} = \frac{1}{m} \langle xp + px \rangle, \quad (1.5)$$

$$\frac{d\langle xp \rangle}{dt} = \frac{d\langle px \rangle}{dt} = \frac{\langle p^2 \rangle}{m} + \langle xF(x) \rangle, \quad (1.6)$$

and

$$\frac{d\langle p^2 \rangle}{dt} = \langle pF(x) + F(x)p \rangle, \quad (1.7)$$

where  $F(x) = -dV/dx$ . These equations have been used to examine the role of quantal uncertainties in wave packet dynamics in the case of the free particle and the harmonic oscillator [17]. We have examined the role of expectation values in a more general setting by considering a nonlinear Hamiltonian which is not of the form given in Eq. (1.1). We have established that, by tracking the time evolution of various moments of certain operators, selective identification of different fractional revivals can be achieved [18].

While revival phenomena have been investigated extensively in the context of Rydberg atoms, both theoretically and experimentally (see, e. g., [19, 20, 21, 22]), for our purposes we have studied the dynamics of an initial wave packet (a single mode of an electromagnetic field) propagating in a Kerr-like medium. This is motivated by the fact that non-classical effects displayed by optical fields have also been investigated intensively for well over a decade now. The model that we consider (in the first part of this thesis) neatly captures the important role played by expectation values of higher moments of operators in wave packet dynamics: we examine the dynamics of the field mode under an effective Hamiltonian

$$H = \hbar\chi a^{\dagger 2} a^2, \quad (1.8)$$

where  $a$  and  $a^\dagger$  are photon destruction and creation operators. The starting point in obtaining this effective Hamiltonian [23], which is written in terms of the field

operators alone (without explicitly invoking the field-medium interaction terms), is the set of classical field equations pertaining to the optical Kerr effect, namely, the dependence of the refractive index of the medium on the intensity of the light propagating through it. While this effect, displayed by certain nonlinear optical materials (Kerr media), can be explained within a classical framework, the field amplitudes are replaced in the standard manner by photon destruction and creation operators, in order to take into account the quantum nature of the radiation field. The effective quantum Hamiltonian is constructed subject to the requirement that the Heisenberg equations for the field operators yield the correct dynamical equations in the classical limit. A ‘Kerr-like’ medium is one for which the above effective Hamiltonian is a good approximate Hamiltonian. In this thesis, we shall use the words ‘Kerr medium’ and ‘Kerr-like medium’ interchangeably.

We note, in passing, that fractional revivals of an initial Gaussian wave packet propagating under the Kerr Hamiltonian have been considered to be potentially useful in quantum computation. They play a significant role in the context of quantum cloning with continuous variables [24]. Fractional revivals corresponding to the appearance of two and four superposed sub-packets are particularly useful in implementing one- and two-bit logic gates [25]. Further, by combining these superposed states with the vacuum using a 50% beam splitter, the output state can be shown to be an entangled state (a Bell state) under certain conditions [26].

Another aspect which we have investigated in some detail in this thesis, in the context of wave packet evolution in the Kerr-like medium, is the precise role played by the initial state in determining the non-classical features exhibited by the time-evolved state. Taking the standard oscillator coherent state (abbreviated as CS throughout this thesis) as the reference initial state for the purposes of comparison, we have examined the extent to which the departure from coherence of different initial states affects the dynamics of the wave packet. In particular, we have identified, both qualitatively and (wherever possible) quantitatively, the manner in which effects such as revivals, fractional revivals and squeezing of the state at certain instants depend on the degree of coherence of the initial state. The initial states considered for this purpose are the photon-added coherent states (ab-

breviated as PACS throughout this thesis). By repeated application of the photon creation operator on a CS, photons can be added to it systematically, and a quantifiable departure of the state from perfect coherence obtained as a consequence. The recent experimental production and complete characterization of the single-photon added coherent state by quantum state tomography [27] adds impetus to our investigation. The single-photon added coherent state is particularly interesting, as it exhibits marginal departure from coherence, and is intermediate between a one-photon Fock state (that is purely quantum mechanical) and a CS (a minimum uncertainty, “classical” state). Hence, in principle, this state offers a convenient tool to follow the smooth transition from the particle to the wave nature of light. We have shown that expectation values computed in the case of an initial PACS at various instants during its temporal evolution in a Kerr-like medium offer a means to assess the effect of imperfect coherence of the initial state upon its subsequent dynamics [28].

A detailed analysis of the squeezing and higher-order squeezing properties of the wave packet in the neighborhood of a two-sub-packet fractional revival provides another method to ascertain whether the initial state is coherent or not [29]. A quantifier to assess the extent of non-classicality of a state can be identified [30] in terms of the Wigner function corresponding to that state. We have used this quantifier to also identify the manner in which non-classical effects in the dynamics of the wave packet are affected, when the initial state is itself a non-classical state such as a PACS. The Wigner function is a quasi-probability distribution function of (a pair of) phase space variables, and could become negative in some regions of the phase plane. It is well known that the Wigner function corresponding to a CS (which is considered to be a classical state) is positive in all regions of the phase plane. This remains true for the Wigner function of the squeezed vacuum state as well. It is therefore not unreasonable to regard the negativity of this function in some region of the phase plane as an indicator of the non-classical nature of the state concerned. Further, the Wigner function can be reconstructed from experimentally measured quantities: for instance, that of a one-photon Fock state has been reconstructed using a phase-randomized pulsed optical homodyne method [31]. The indicator [30] based on the Wigner function that we have used

is merely one way of quantifying the extent of the non-classicality of a state, but it suffices for our purposes. The Sudarshan-Glauber  $P$ -function [32], for instance, would provide another measure of the non-classicality of a state.

The dynamics of a single mode of the radiation field enables us to understand, to a considerable extent, the connections between the behavior of quantum expectation values and revival phenomena. When two-mode interactions are considered, another significant aspect of quantum physics appears — namely, entanglement. We have examined the conditions under which analogs of revivals and fractional revivals of the initial state occur in this case. Revivals of two initially non-entangled modes governed by a nonlinear Hamiltonian have been examined in the literature [33]. However, in order to study the full spectrum of randomness exhibited by the expectation values of relevant observables as they evolve in time, we need a system in which revival phenomena can either occur or be suppressed, depending on the values of the parameters in the Hamiltonian considered. A good candidate Hamiltonian for this purpose is obtained by a straightforward extrapolation of the single-mode example considered earlier, to explicitly take into account the atomic modes in the Kerr-like medium through which a single-mode electromagnetic field propagates, and the interaction between the atoms and the field. The Hamiltonian for the total system is given by [34]

$$H = \hbar\omega a^\dagger a + \hbar\omega_0 b^\dagger b + \hbar\gamma b^{\dagger 2} b^2 + \hbar g (a^\dagger b + b^\dagger a). \quad (1.9)$$

As before, the ladder operators  $a$  and  $a^\dagger$  pertain to the field, while  $b$  and  $b^\dagger$  are the ladder operators for the nonlinear oscillator modeling an atom of the medium.  $\gamma$  is the anharmonicity parameter, and  $g$  is the strength of the interaction between the field and the medium. It is easily verified that the operator  $(a^\dagger a + b^\dagger b)$  commutes with  $H$ . We have analyzed this model for initial states that are direct product states, in which the atom is in its ground state, while the field is, respectively, in a Fock state, a coherent state, and a photon-added coherent state. Detailed results have been obtained on the precise manner in which the moments of appropriate quadrature variables display the counterparts of the revival and fractional revival phenomena in this case. These phenomena arise for weak nonlinearity, i.e., for

sufficiently small ( $\ll 1$ ) values of the ratio  $\gamma/g$ .

We have shown that these revival phenomena also manifest themselves in the entropy of entanglement of the system. The latter may be taken to be either the sub-system von Neumann entropy or the sub-system linear entropy, where by “sub-system” we mean either the field or the medium. These entropies are defined in terms of the corresponding reduced density operators. Striking differences arise in the behaviour of the entropies for different initial states of the field. These have been described in detail in the thesis.

The situation that prevails for sufficiently large values of  $\gamma/g$  is especially interesting. We have carried out a time-series and power spectrum analysis [35, 36, 37] of the time series generated by the values of the mean photon number  $\langle a^\dagger a \rangle$  computed over long intervals of time, and assessed the effect of the departure from coherence of the initial field mode on the ergodicity properties of the mean photon number [38]. The time series analysis shows that a wide range of behavior can manifest itself in the dynamics of the sub-system represented by the field mode: a progression occurs, from mere ergodicity for a coherent initial state and weak nonlinearity, all the way to “chaotic” behavior (as characterized by a positive Lyapunov exponent) for a sufficiently large departure from coherence of the initial state (i. e., a PACS with a relatively large number of added photons) and a sufficiently large nonlinearity (as given by the ratio  $\gamma/g$ ). This is corroborated by the fact that similar behavior is exhibited by  $\langle b^\dagger b \rangle$ , in such a manner that  $\langle b^\dagger b \rangle + \langle a^\dagger a \rangle$  remains constant, as required. The implications of “chaotic” dynamics, and what it really means in this context, are of special interest. A discussion of these aspects is given in the relevant chapter of the thesis.

A summary of the contents of the contents of the rest of this thesis is as follows:

**Chapter 2** is devoted to a discussion of the manner in which distinctive signatures of revivals and fractional revivals are displayed in the time evolution of appropriate observables, which help in selectively identifying different fractional revivals [18]. The model Hamiltonian used is that of a single mode propagating in a Kerr-like medium, Eq. (1.8), while the wave packet considered corresponds

to a coherent initial state.

**Chapter 3** describes how revivals and fractional revivals of a wave packet propagating in the nonlinear medium provide signatures of the degree of coherence of the initial wave packet. The investigation focuses on revival phenomena in the case of an initial photon-added coherent state. A comparison vis-à-vis the corresponding results obtained for an initial coherent state enables the elucidation of the role played by the coherence of the initial state in determining the revival properties of the state [28].

**Chapter 4** is concerned with the squeezing and higher-order squeezing properties of a PACS as it propagates in the nonlinear medium. Once again, the precise manner in which departure from coherence of the initial state affects its squeezing properties at the instants of revivals and fractional revivals is brought out [29].

**Chapter 5** is based on the Hamiltonian in Eq. (1.9), that describes the entanglement dynamics of a single-mode electromagnetic field interacting with a nonlinear medium, an atom of the latter being modelled as an anharmonic oscillator. Revival phenomena are now examined in terms of the expectation values of certain observables, as well as the sub-system von Neumann entropy and the sub-system linear entropy. The initial states considered are direct product states, in which the atom is in its ground state, while the field is taken to be in either a number state, or a CS, or a PACS. Once again, this leads to an understanding of the role played by the initial state.

**Chapter 6** deals with the case in which revivals of the initial state are suppressed. The dynamical behaviour of the mean photon number is investigated [38] by means of a time-series analysis, in order to identify the effects of different initial states on the entanglement and ergodicity properties of the system. This behavior is seen to range from quasi-periodicity to exponential instability, depending on the specific initial state and the values of certain parameters occurring in the Hamiltonian.

**Chapter 7** concludes the thesis with some brief remarks placing this work in a broader perspective, and a list of open problems and avenues for further research.

# CHAPTER 2

## Manifestations of wave packet revivals in the moments of observables - I

### 2.1 Introduction

Revivals and fractional revivals of a wave packet propagating in a nonlinear medium have been extensively investigated in the literature [8]. Since revival phenomena arise from quantum interference, it is of interest to examine precisely how their occurrence is captured in the expectation values of appropriate physical observables. Such investigations have led to a better understanding of different aspects of revival phenomena in a wide variety of physical situations, ranging from wave packet propagation in the infinite square well [39] to the long-time behavior of a quantum bouncer [40]. In this Chapter, we discuss the manner in which distinctive signatures of revivals and fractional revivals are displayed in the time evolution of certain observables, thereby facilitating the selective identification of different fractional revivals [18]. It is necessary to bear in mind the salient features of the specific quantum interference between the basis states comprising the wave packet when we analyze the dynamics of expectation values. For this purpose, we outline in the next Section the conditions under which revivals and fractional revivals of a wave packet occur.

### 2.2 Revivals and fractional revivals in wave packet dynamics

The broad features of wave packet dynamics are quite generic, regardless of the details of the physical system concerned, the initial wave packet considered, and



the specific nonlinear Hamiltonian governing the time evolution. We recall from Chapter 1 that, given an initial state  $|\psi(0)\rangle$ , a revival is the return of the overlap function

$$C(t) = |\langle\psi(0)|\psi(t)\rangle|^2 \quad (2.1)$$

to its initial value of unity at specific instants of time. Revivals and fractional revivals are essentially controlled by the parameters occurring, respectively, in the first and second-order terms in the Taylor expansion of the energy spectrum  $E_n$  about the energy  $E_{n_0}$  corresponding to the peak of the wave packet. Hence, it suffices to consider wave packet evolution governed by an effective Hamiltonian whose energy eigenvalues are at most quadratic functions of  $n$ . Further, one of our objectives is to examine the role played by the initial state in the subsequent dynamics. Therefore, for purposes of comparison, an appropriate reference state must be selected. A good starting point is the investigation of the revival phenomena displayed by an initial coherent state (CS) propagating in a Kerr-like medium, so as to facilitate subsequent comparison with the dynamics of initial states which depart in a quantifiable manner from coherence. We explicitly demonstrate below the role played by quantum interference in this context [13].

The effective Hamiltonian for the propagation of a single-mode electromagnetic field in a Kerr medium is given by [41, 42]

$$H = \chi a^{\dagger 2} a^2 = \chi \mathbf{N}(\mathbf{N} - 1) \quad (2.2)$$

in the usual notation, where  $a$  (respectively,  $a^\dagger$ ) is the photon annihilation (respectively, creation) operator,  $\mathbf{N} = a^\dagger a$  is the photon number operator, and  $\chi (> 0)$  is essentially the third-order nonlinear susceptibility of the medium. Here, and in the rest of this thesis,  $\hbar$  has been set equal to unity. We shall restore this factor when it becomes essential to do so (e. g, in Sec. 6.1 of Chapter 6). This Hamiltonian is also relevant in a very different physical context, namely, in describing the dynamics of a Bose-Einstein condensate in a potential well. In that case,  $a$  and  $a^\dagger$  are boson annihilation and creation operators, and  $\chi$  characterizes the energy needed to overcome the inter-atomic repulsion in adding an atom to the population of the

potential well [43]. Many of the results that we derive may therefore be expected to be applicable in the context of atom optics and Bose-Einstein condensate, as well.

The initial state of the field  $|\psi(0)\rangle$  is taken to be the CS  $|\alpha\rangle$ , where  $\alpha$  is any complex number. It satisfies

$$a|\alpha\rangle = \alpha|\alpha\rangle. \quad (2.3)$$

The Fock state representation of the CS, which we will use extensively, is given by

$$|\alpha\rangle = e^{-|\alpha|^2/2} \sum_{n=0}^{\infty} \frac{\alpha^n}{\sqrt{n!}} |n\rangle. \quad (2.4)$$

The unitary time evolution operator  $U(t)$  corresponding to the Hamiltonian of Eq. (2.2) is

$$U(t) = \exp[-i\chi t \mathbf{N}(\mathbf{N} - 1)]. \quad (2.5)$$

Hence the state of the field at time  $t$  is given by

$$|\psi(t)\rangle = \exp[-i\chi t \mathbf{N}(\mathbf{N} - 1)] |\alpha\rangle. \quad (2.6)$$

The time evolution operator at instants  $t = \pi/(k\chi)$  (where  $k$  is an integer), namely,

$$U(\pi/k\chi) = \exp\left[-\frac{i\pi}{k} \mathbf{N}(\mathbf{N} - 1)\right], \quad (2.7)$$

displays interesting periodicity properties. These follow from the fact that the eigenvalues of  $\mathbf{N}$  are integers. We will use  $N$  to denote these eigenvalues. For odd integer values of  $k$ ,

$$\exp\left[-\frac{i\pi}{k}(N+k)(N+k-1)\right] = \exp\left[\frac{-i\pi}{k}N(N-1)\right]. \quad (2.8)$$

Similarly, for even integer values of  $k$ ,

$$\exp\left[-\frac{i\pi}{k}(N+k)^2\right] = \exp\left[-\frac{i\pi}{k}N^2\right]. \quad (2.9)$$

As a consequence,  $U(\pi/k\chi)$  can be expanded in a Fourier series with  $\exp(-2\pi ij/k)$

as the basis functions, in the form

$$\exp\left[-\frac{i\pi}{k}N(N-1)\right] = \sum_{j=0}^{k-1} f_j \exp\left[-\frac{2\pi ij}{k}N\right] \quad (2.10)$$

for odd values of  $k$ , and

$$\exp\left[-\frac{i\pi}{k}N^2\right] = \sum_{j=0}^{k-1} g_j \exp\left[-\frac{2\pi ij}{k}N\right] \quad (2.11)$$

for even values of  $k$ , respectively, where the coefficients  $f_j$  and  $g_j$  are known. Using the above equations and the property

$$e^{i\chi a^\dagger a} |\alpha\rangle = |\alpha e^{i\chi}\rangle, \quad (2.12)$$

we find

$$|\psi(\pi/k\chi)\rangle = \begin{cases} \sum_{j=0}^{k-1} f_j |\alpha e^{-2\pi ij/k}\rangle, & k \text{ odd;} \\ \sum_{j=0}^{k-1} g_j |\alpha e^{i\pi/k} e^{-2\pi ij/k}\rangle, & k \text{ even.} \end{cases} \quad (2.13)$$

It is evident that at time  $T_{\text{rev}} = \pi/\chi$ , corresponding to  $k = 1$ , the initial state revives for the first time. Periodic revivals occur at integer multiples of  $T_{\text{rev}}$ . Further, between  $t = 0$  and  $t = T_{\text{rev}}$  and between two successive revivals, fractional revivals occur at instants  $nT_{\text{rev}} + T_{\text{rev}}/k$ . At these instants, the initial wave packet evolves to a state that can be described as a finite superposition of ‘rotated’ coherent states with definite amplitudes. For instance, the state at time  $\pi/(2\chi)$  (corresponding to  $k = 2$ ) is a superposition of the two coherent states  $|i\alpha\rangle$  and  $|-i\alpha\rangle$ . In general,  $|\psi(\pi/k\chi)\rangle$  is a superposition of  $k$  coherent states. The corresponding wave packet in position space is a superposition of  $k$  spatially distributed Gaussian wave packets. The periodicity property of  $U$  further implies that the wave function at times  $t = \pi j/(k\chi)$ ,  $1 \leq j \leq k - 1$  for a given  $k$ , is also a superposition of  $k$  wave packets [19].

## 2.3 Signatures of revivals and fractional revivals in quantum expectation values

We now proceed to examine the manner in which fractional revivals are manifested in distinctive ways in the expectation values of the physical observables pertaining to the system at hand. As the system enjoys revivals with a period  $T_{\text{rev}}$ , all such expectation values are periodic functions of  $t$  with this fundamental period. A family of relevant observables is provided (in the context of nonlinear media) by the field quadrature ( $a e^{i\varphi} + a^\dagger e^{-i\varphi}$ ) for various values of the phase  $\varphi$ . In the context of Bose-Einstein condensation, the expectation value  $\langle a(t) \rangle$  of the atom annihilation operator represents the condensate wave function. Its real and imaginary parts (which correspond to the cases  $\varphi = 0$  and  $\varphi = -\frac{1}{2}\pi$ , respectively) are analogous to classical phase space variables. Let us define the operators

$$x = \frac{(a + a^\dagger)}{\sqrt{2}} \quad \text{and} \quad p = \frac{(a - a^\dagger)}{i\sqrt{2}}. \quad (2.14)$$

Clearly, their expectation values alone do not suffice to reproduce the full information contained in the wave function itself. In principle, an infinite set of moments, comprising the expectation values of *all* powers of  $x$  and  $p$  and their combinations, is required for this purpose. In this sense, the quantum system is equivalent to an infinite-dimensional classical system in which the role of the dynamical variables is played by the set of expectation values. However, we emphasize that even the first few moments can be shown to yield considerable information on the behavior of the system.

Recalling that  $a|\alpha\rangle = \alpha|\alpha\rangle$ , we define the  $c$ -number function

$$\alpha(t) = \langle \psi(t) | a | \psi(t) \rangle = \langle \alpha | e^{iHt/\hbar} a e^{-iHt/\hbar} | \alpha \rangle, \quad (2.15)$$

so that  $\alpha(0) \equiv \alpha$ . For the case at hand, this simplifies after some algebra to

$$\alpha(t) = \alpha e^{-|\alpha|^2(1-\cos 2\chi t)} [\cos (|\alpha|^2 \sin (2\chi t)) - i \sin (|\alpha|^2 \sin (2\chi t))]. \quad (2.16)$$

Thus  $\alpha(t)$  is a periodic function of time with period  $\pi/\chi$ , as expected. It is convenient to introduce the notation

$$\alpha = \alpha_1 + i\alpha_2 = \frac{(x_0 + ip_0)}{\sqrt{2}} \quad (2.17)$$

and

$$\nu = |\alpha|^2 = \frac{1}{2}(x_0^2 + p_0^2). \quad (2.18)$$

$x_0$  and  $p_0$  represent the locations of the centers of the initial Gaussian wave packets corresponding to the CS  $|\alpha\rangle$  in position space and momentum space, respectively. The expectation values of  $x$  and  $p$  at any time can then be obtained as explicit functions of  $t$  (as stated in Appendix B) in the form

$$\langle x(t) \rangle = e^{-\nu(1-\cos 2\chi t)} [x_0 \cos(\nu \sin 2\chi t) + p_0 \sin(\nu \sin 2\chi t)], \quad (2.19)$$

$$\langle p(t) \rangle = e^{-\nu(1-\cos 2\chi t)} [-x_0 \sin(\nu \sin 2\chi t) + p_0 \cos(\nu \sin 2\chi t)]. \quad (2.20)$$

Expressions for the higher moments can be deduced readily from the general result

$$\langle a^{\dagger r} a^{r+s} \rangle = \alpha^s \nu^r e^{-\nu(1-\cos 2s\chi t)} \exp[-i\chi(s(s-1) + 2rs)t - i\nu \sin 2s\chi t], \quad (2.21)$$

where  $r$  and  $s$  are non-negative integers. This result is derived in Appendix A (see Eq. (A.15)). It is a special case of a more general relation derived there (Eq. (A.14)). Using this result, the second moments of  $x$  and  $p$  are found to be given by

$$\begin{aligned} 2\langle x^2(t) \rangle &= 1 + x_0^2 + p_0^2 + e^{-\nu(1-\cos 4\chi t)} [(x_0^2 - p_0^2) \cos(2\chi t + \nu \sin 4\chi t) \\ &\quad + 2x_0 p_0 \sin(2\chi t + \nu \sin 4\chi t)], \end{aligned} \quad (2.22)$$

$$\begin{aligned} 2\langle p^2(t) \rangle &= 1 + x_0^2 + p_0^2 - e^{-\nu(1-\cos 4\chi t)} [(x_0^2 - p_0^2) \cos(2\chi t + \nu \sin 4\chi t) \\ &\quad + 2x_0 p_0 \sin(2\chi t + \nu \sin 4\chi t)]. \end{aligned} \quad (2.23)$$

For reasons already mentioned, the higher moments also carry much information of direct interest. We give below the expressions for the third and fourth moments as well, since we need them to obtain the skewness and kurtosis in all the cases of interest. The third moments can be written compactly in the form

$$\begin{aligned}
4 \langle x^3(t) \rangle &= e^{-\nu(1-\cos 6\chi t)} [(x_0^3 - 3x_0 p_0^2) \cos(6\chi t + \nu \sin 6\chi t) \\
&+ (3x_0^2 p_0 - p_0^3) \sin(6\chi t + \nu \sin 6\chi t)] \\
&+ 6\nu [\langle x(t) \rangle (1 + \cos 2\chi t) + \langle p(t) \rangle \sin 2\chi t], \tag{2.24}
\end{aligned}$$

$$\begin{aligned}
4 \langle p^3(t) \rangle &= e^{-\nu(1-\cos 6\chi t)} [(x_0^3 - 3x_0 p_0^2) \sin(6\chi t + \nu \sin 6\chi t) \\
&- (3x_0^2 p_0 - p_0^3) \cos(6\chi t + \nu \sin 6\chi t)] \\
&+ 6\nu [\langle p(t) \rangle (1 + \cos 2\chi t) - \langle x(t) \rangle \sin 2\chi t]. \tag{2.25}
\end{aligned}$$

The fourth moments are given by

$$\begin{aligned}
8 \langle x^4(t) \rangle &= e^{-\nu(1-\cos 8\chi t)} [(x_0^4 + p_0^4 - 6x_0^2 p_0^2) \cos(12\chi t + \nu \sin 8\chi t) \\
&+ 4(x_0^3 p_0 - x_0 p_0^3) \sin(12\chi t + \nu \sin 8\chi t)] \\
&+ 8\nu e^{-\nu(1-\cos 4\chi t)} [(x_0^2 - p_0^2) \cos(6\chi t + \nu \sin 4\chi t) \\
&+ 2x_0 p_0 \sin(6\chi t + \nu \sin 4\chi t)] \\
&+ 24 \langle x^2(t) \rangle + 3(x_0^2 + p_0^2)^2 - 6, \tag{2.26}
\end{aligned}$$

$$\begin{aligned}
8 \langle p^4(t) \rangle &= e^{-\nu(1-\cos 8\chi t)} [(x_0^4 + p_0^4 - 6x_0^2 p_0^2) \cos(12\chi t + \nu \sin 8\chi t) \\
&+ 4(x_0^3 p_0 - x_0 p_0^3) \sin(12\chi t + \nu \sin 8\chi t)] \\
&- 8\nu e^{-\nu(1-\cos 4\chi t)} [(x_0^2 - p_0^2) \cos(6\chi t + \nu \sin 4\chi t) \\
&+ 2x_0 p_0 \sin(6\chi t + \nu \sin 4\chi t)] \\
&- 24 \langle x^2(t) \rangle + 3(x_0^2 + p_0^2)^2 + 24(x_0^2 + p_0^2) + 18. \tag{2.27}
\end{aligned}$$

With these expressions, the variances of  $x$  and  $p$  as functions of  $t$ , as also the skewness and kurtosis in each case, can be obtained. The uncertainty product (i. e., the product of the respective standard deviations)  $\Delta x \Delta p$ , which initially

has the minimum value  $\frac{1}{2}$ , is of special interest. We do not write down the lengthy expressions for these quantities here, but we shall comment upon their time variation in the sequel, when discussing the numerical results for specific values of the parameters.

## 2.4 Moments of $x$ and $p$ : A classical interpretation

Before discussing our results in detail, we digress briefly to compare the explicit solutions found for the expectation values of  $x$  and  $p$  in Eqs. (2.19) and (2.20) with the solutions that would have been obtained for  $x(t)$  and  $p(t)$  had the system been a *classical* one, governed by the classical counterpart of the normal-ordered Hamiltonian (restoring the factor  $\hbar$ )  $H = \hbar\chi a^{\dagger 2} a^2$ , namely,

$$H_{\text{cl}} = \frac{1}{4}(x^2 + p^2)^2. \quad (2.28)$$

Although the equations of motion corresponding to  $H_{\text{cl}}$  are nonlinear, it is evident that  $x^2 + p^2$  is a constant of the motion, so that the phase trajectories are circles. However, the frequency of motion is dependent on the initial conditions (i.e., the amplitude of the motion), being equal to  $\nu = \frac{1}{2}(x_0^2 + p_0^2)$ . This is, of course, a well-known feature of nonlinear oscillators. But we note that the actual solutions for  $\langle x(t) \rangle$  and  $\langle p(t) \rangle$  in Eqs. (2.19) and (2.20) are more complicated than the classical ones for  $x(t)$  and  $p(t)$  under  $H_{\text{cl}}$ . This is a consequence of the quantum mechanical nature of the system, over and above the nonlinearity of  $H$ . However, the expressions for  $\langle x(t) \rangle$  and  $\langle p(t) \rangle$  can be given the following interesting interpretation in classical terms. Define the (non-canonical) pair of classical dynamical variables

$$X = \langle x \rangle e^{\nu(1-\cos 2\chi t)}, \quad P = \langle p \rangle e^{\nu(1-\cos 2\chi t)}, \quad (2.29)$$

and the *re-parametrized time*  $\tau = \sin(2\chi t)$ . The initial values of these variables are again  $x_0$  and  $p_0$ , respectively. Equations (2.19) and (2.20) can then be re-written

in the suggestive form

$$X = x_0 \cos \nu\tau + p_0 \sin \nu\tau, \quad P = -x_0 \sin \nu\tau + p_0 \cos \nu\tau. \quad (2.30)$$

But these are the solutions to the system of equations

$$dX/d\tau = \nu P, \quad dP/d\tau = -\nu X, \quad (2.31)$$

describing a nonlinear oscillator of frequency

$$\nu = \frac{1}{2}(x_0^2 + p_0^2), \quad (2.32)$$

in terms of the transformed variables  $(X, P)$  and the re-parametrized time  $\tau$ . At the level of the *first* moments, therefore, the system is effectively a nonlinear oscillator after a suitable transformation of the relevant variables, together with a re-parametrization of the time.

## 2.5 Signatures of fractional revivals

We now discuss our results, using representative numerical values for the various parameters in the problem. Turning to the time dependence of the various moments of  $x$  and  $p$ , there are two striking features that underlie the essential point we wish to make. First, the higher the order of the moment (or cumulant), the more rapid is its variation, since the leading (highest) frequency in the  $k^{\text{th}}$  moment is  $2k\chi$ . Second, the time dependence is strongly controlled by the factor  $\exp[-\nu(1 - \cos 2k\chi t)]$ ,  $k = 1, 2, \dots$ , that modulates the oscillatory terms. While this permits substantial time variation for sufficiently small values of  $\nu$ , it acts as a strong damping factor for large values of  $\nu$ , *except when*  $\cos(2m\chi t)$  *is near unity*. As one might expect, this happens precisely at revivals (when  $t = n\pi/\chi$ , an integer multiple of  $T_{\text{rev}}$ ). But it also happens — in the  $k^{\text{th}}$  moment and *not* in the lower moments — at the fractional revival times  $t = (n + j/k)T_{\text{rev}}$ . Thus, by setting  $\nu$  at a suitably large value, we can ensure that the moments are essentially



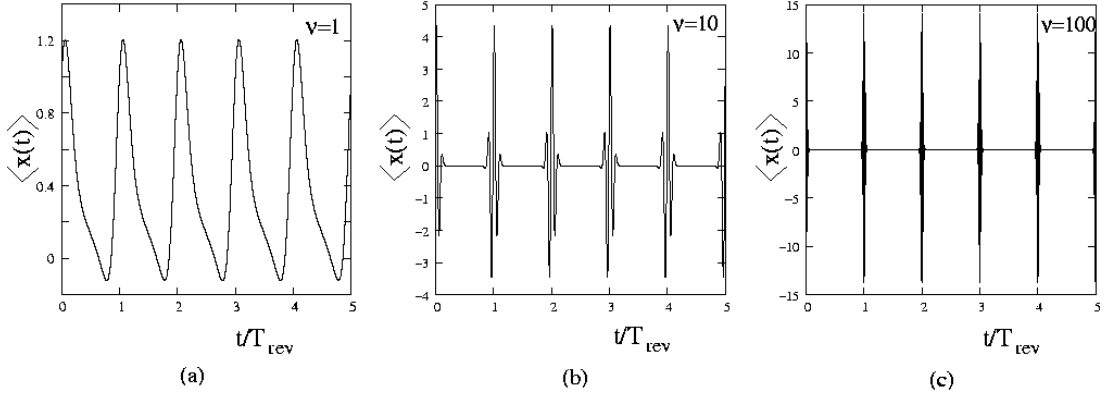


Figure 2.1:  $\langle x \rangle$  as a function of time

static, bursting into rapid variation at specific instants of time before reverting to quiescence.

These points are illustrated in the figures. Owing to an obvious symmetry of  $H$ , the moments of  $x$  and  $p$  behave in an essentially similar manner, especially if we start with the symmetric initial condition  $x_0 = p_0$ . Without significant loss of generality, we restrict ourselves to this case in what follows. We have set  $\chi = 5$  in the numerical results to be presented, but this is irrelevant, as all the plots correspond to  $t$  measured in units of  $T_{\text{rev}} = \pi/\chi$ . We find that for very small values ( $\ll 1$ ) of  $x_0$  and  $p_0$  (i. e., of  $\nu$ ), the nonlinearity of  $H$  does not play a significant role, and the behavior of the system is much like that of a simple oscillator. Interesting behavior occurs for larger values of  $\nu$ . We therefore present results for three typical values of the parameters representing the initial conditions, namely:

$$(a) \quad x_0 = p_0 = 1 \Rightarrow \nu = 1;$$

$$(b) \quad x_0 = p_0 = \sqrt{10} \Rightarrow \nu = 10;$$

$$(c) \quad x_0 = p_0 = 10 \Rightarrow \nu = 100.$$

These correspond, respectively, to small, intermediate, and large values of  $\nu$ . In all the “phase plots”, the point representing the state at  $t = 0$  is labeled A.

Figures 2.1(a)-(c) show the variation of  $\langle x(t) \rangle$  as a function of  $t$  for small, medium and large values of  $\nu$ . (As already mentioned,  $\langle p(t) \rangle$  displays similar

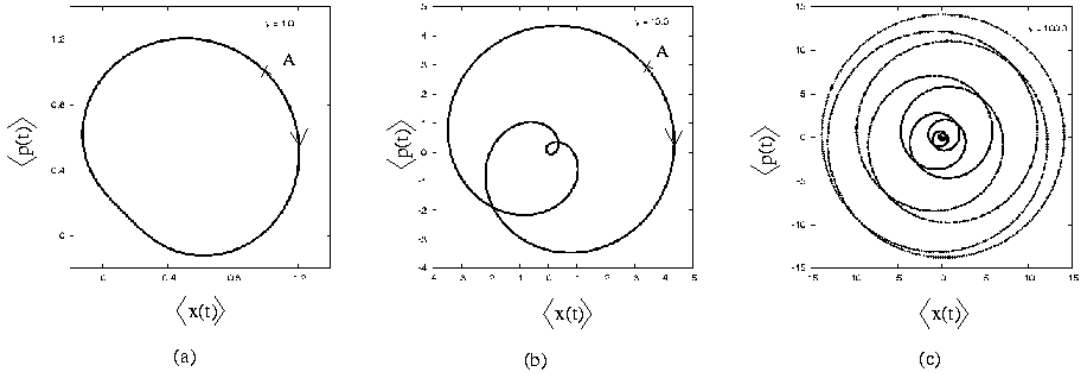


Figure 2.2: “Phase plot” of  $\langle p \rangle$  versus  $\langle x \rangle$

behavior.) For sufficiently large values of  $\nu$ , it is evident that, except for times close to integer multiples of  $T_{\text{rev}}$ ,  $\langle x(t) \rangle$  and  $\langle p(t) \rangle$  essentially remain static at the value zero. Figures 2.2(a)-(c) depict the corresponding “phase plots” in the  $(\langle x \rangle, \langle p \rangle)$  plane. In Fig. 2.2(c), the representative point remains at the origin most of the time, except at times close to successive revivals, when it rapidly traverses the rest of the curve before returning to the origin.

While sudden changes from nearly static values of  $\langle x(t) \rangle$  and  $\langle p(t) \rangle$  are thus signatures of revivals, the occurrence of fractional revivals is not captured in these mean values. The fractional revival occurring mid-way between successive revivals (e. g., at  $t = \pi/2\chi$  in the interval between  $t = 0$  and  $t = T_{\text{rev}}$ ), when the initial wave packet reconstitutes itself into two separate wave packets of a similar kind, leaves its signature upon the second moments. Figures 2.3(a)-(c) show the variation with time of the uncertainty product  $\Delta x \Delta p$ . In each case, this product returns at every revival to its initial, minimum, value ( $= \frac{1}{2}$ ), rising to higher values in between revivals. Once again, for sufficiently large values of  $\nu$ , the product remains essentially static at the approximate value  $(\frac{1}{2} + \nu)$  for most of the time, but undergoes extremely rapid variation near revivals, and *also* near the fractional revivals occurring mid-way between revivals. During the latter, the uncertainty product drops to smaller values, but does not reach the minimum value  $\frac{1}{2}$ .

There is a very striking difference in the behavior of the standard deviations near revivals as opposed to their behavior near the foregoing fractional revivals. This is brought out in Figs. 2.4(a)-(c), which is a “phase plot” of  $\Delta p$  versus

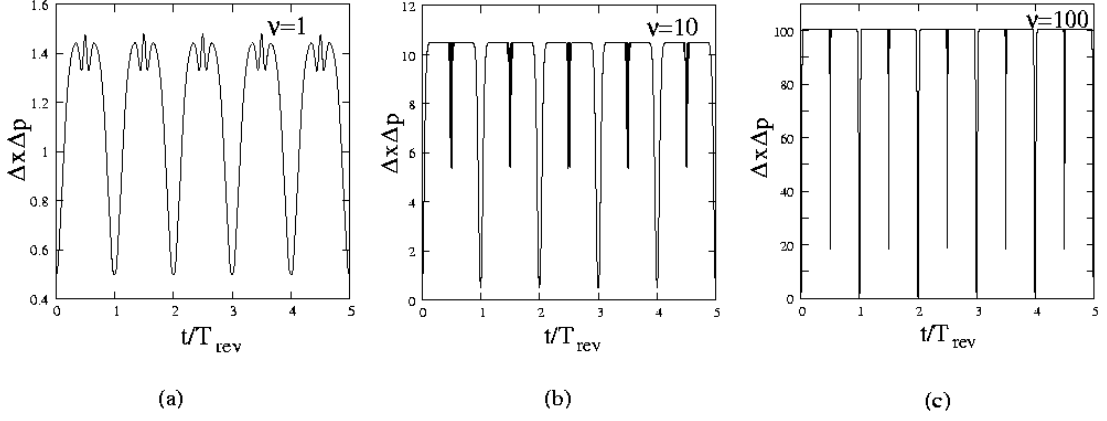


Figure 2.3: Variation of the uncertainty product with time

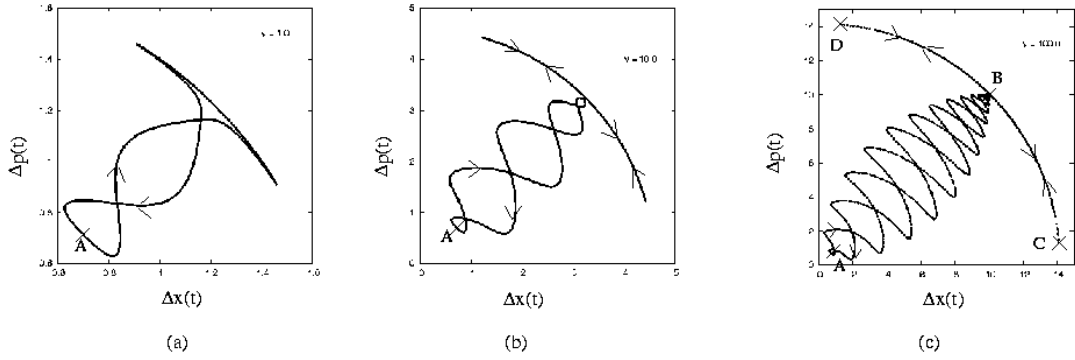


Figure 2.4: “Phase plot” of  $\Delta p$  versus  $\Delta x$  for  $\nu = 1, 10$  and  $100$ , respectively.

$\Delta x$ . For very small  $\nu$ , as in Fig. 2.4(a),  $\Delta x$  and  $\Delta p$  vary quite gently around a simple closed curve. When  $\nu$  is somewhat larger, as in 2.4(b) which corresponds to  $\nu = 10$ , the plot begins to show interesting structure. For much larger values of  $\nu$  as in 2.4(c), the initial point A quickly moves out on the zig-zag path about the radial  $\Delta p = \Delta x$  line to the steady value represented by the point B, and returns to A at every revival along the complementary zig-zag path. Close to the fractional revival at  $t = (n + \frac{1}{2})T_{\text{rev}}$ , however, the representative point moves back and forth along the azimuthal path BCDB rather than the zig-zag path: clearly, a kind of “squeezing” occurs, as one of the variances reaches a small value while the other becomes large, and vice versa. (Of course the state of the system is far from a minimum uncertainty state throughout, except at the instants  $nT_{\text{rev}}$ .)

The fractional revivals occurring at  $t = (n + \frac{1}{3})T_{\text{rev}}$  and  $t = (n + \frac{2}{3})T_{\text{rev}}$ , at which the initial wave packet is reconstituted into a superposition of *three* separate wave packets, are detectable in the third moments of  $x$  and  $p$ . To make this

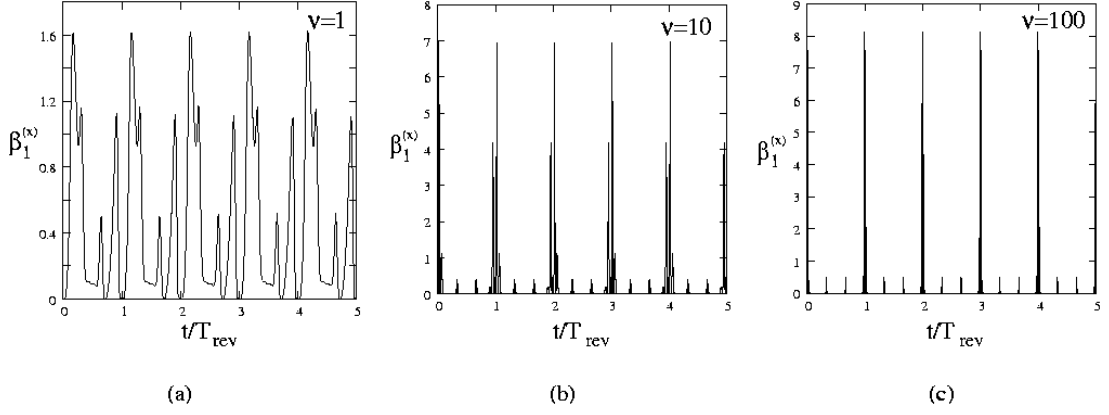


Figure 2.5: Square of the skewness in  $x$  as a function of time

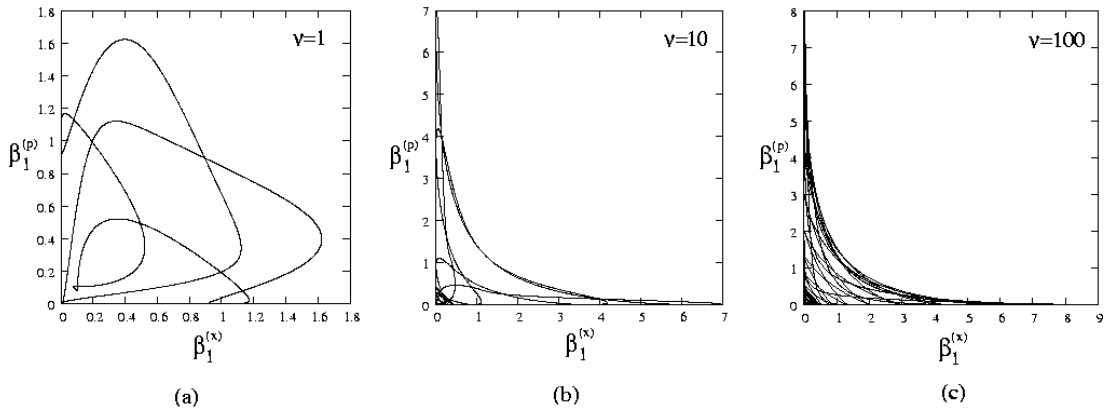


Figure 2.6: The “phase plot” of  $\beta_1^{(p)}$  versus  $\beta_1^{(x)}$

unambiguous, we may consider the third moments about the mean values — or, in standard statistical notation, the square of the skewness, defined as

$$\beta_1^{(x)} = \frac{\langle (x - \langle x \rangle)^3 \rangle^2}{(\langle x^2 \rangle - \langle x \rangle^2)^3} \equiv \frac{\langle (\delta x)^3 \rangle^2}{(\Delta x)^6}, \quad (2.33)$$

and similarly for  $\beta_1^{(p)}$ . Figures 2.5(a)-(c) show the variation of  $\beta_1^{(x)}$  with  $t$ . It is evident that, for sufficiently large values of  $\nu$ ,  $\beta_1^{(x)}$  remains nearly zero most of the time, except for bursts of rapid variation close to revivals and fractional revivals. Both  $\beta_1^{(x)}$  and  $\beta_1^{(p)}$  actually vanish at  $t = nT_{\text{rev}}$  (since the Gaussian wave packet corresponding to the CS  $|\alpha\rangle$  has no skewness in either  $x$  or  $p$ ), but they remain non-zero at  $t = (n + \frac{1}{3}j) T_{\text{rev}}$ ,  $j = 1, 2$ . More detailed information is obtained from a “phase plot” of  $\beta_1^{(p)}$  versus  $\beta_1^{(x)}$ , depicted in Figs. 2.6 (a)-(c).

Finally, we consider fractional revivals corresponding to  $m = 4$ , when *four*

superposed wave packets appear. These are detectable in the behavior of the fourth moments of  $x$  and  $p$ . Equivalently, we may use the excess of kurtosis ( $\beta_2 - 3$ ), where the kurtosis of  $x$  is defined as

$$\beta_2^{(x)} = \frac{\langle (x - \langle x \rangle)^4 \rangle}{(\langle x^2 \rangle - \langle x \rangle^2)^2} \equiv \frac{\langle (\delta x)^4 \rangle}{(\Delta x)^4}, \quad (2.34)$$

with a similar definition for  $\beta_2^{(p)}$ . The excess of kurtosis is the measure of the departure of a distribution from a Gaussian. Figures 2.7(a)-(c) depict how  $(\beta_2^{(x)} - 3)$  varies with time. For sufficiently large  $\nu$ , both  $(\beta_2^{(x)} - 3)$  and  $(\beta_2^{(p)} - 3)$  re-

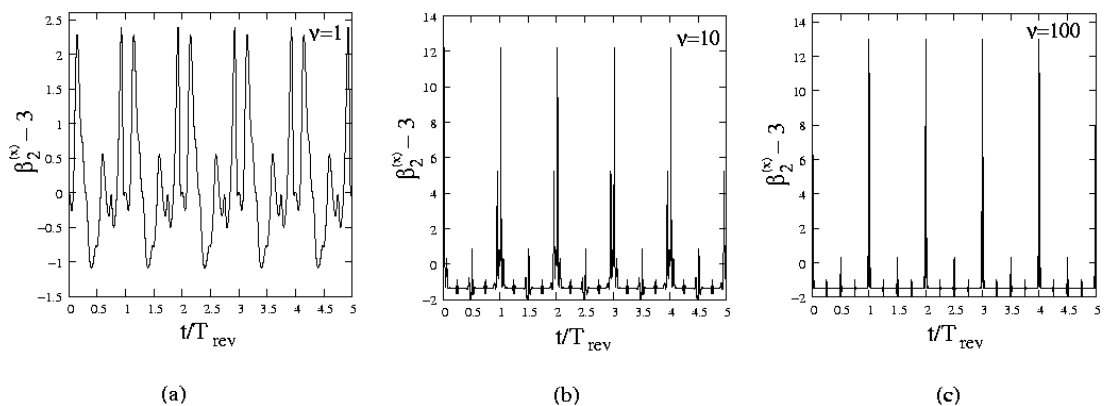


Figure 2.7: The excess of kurtosis of  $x$  as a function of time

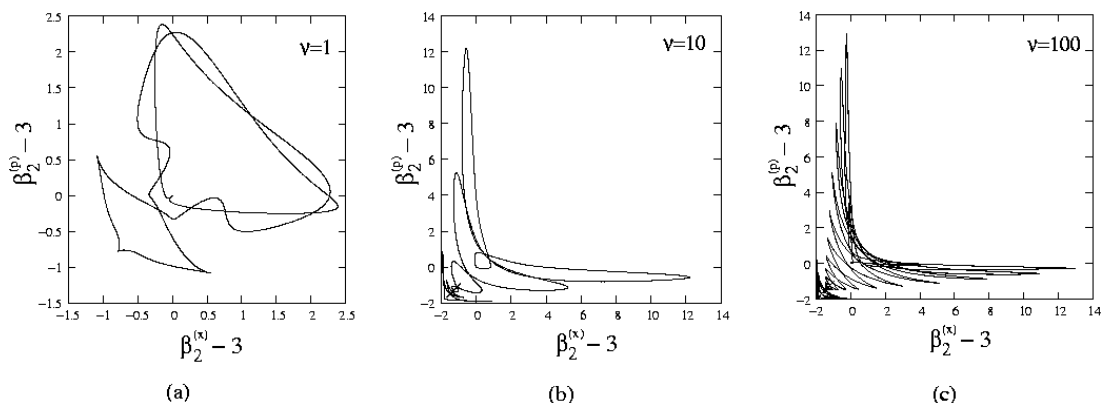


Figure 2.8: “Phase plot” of  $(\beta_2^{(p)} - 3)$  versus  $(\beta_2^{(x)} - 3)$

main essentially static near the value  $-\frac{3}{2}$  most of the time. They vary rapidly near revivals, vanishing at  $t = nT_{\text{rev}}$  because the wave packet is a Gaussian both in position space and in momentum space at these instants of time. As is clear from Fig. 2.7(c), they also vary rapidly near the fractional revivals at

$t = (n + j/4)T_{\text{rev}}$  (where  $j = 1, 2, 3$ ), oscillating about the “steady value”  $-\frac{3}{2}$ . Once again, a “phase plot” of  $(\beta_2^{(p)} - 3)$  versus  $(\beta_2^{(x)} - 3)$  helps identify features that distinguish between the three fractional revivals concerned. These are shown in Figs. 2.8 (a)-(c).

## 2.6 Concluding remarks

We have shown that distinctive signatures of the different fractional revivals of a suitably prepared initial wave packet are displayed in the mean values and higher moments of appropriate observables. The complicated quantum interference effects that lead to fractional revivals can thus be captured in the dynamics of these expectation values, which may be regarded as effective dynamical variables in a classical phase space. While direct experimental measurement of the expectation values considered, particularly the higher moments of the quadrature variables, is certainly not easy, it is not, *à priori*, impossible. Moreover, the essential point of our analysis is to bring out explicitly an interesting aspect of quantum interference: the link between the occurrence of a  $k$ -sub-packet fractional revival and the behavior of the  $k$ th moment of appropriate observables, emphasizing (as in the rest of this thesis) the role of quantum expectation values in the investigation of non-classical effects. Again, it is evident that the specific observables signaling the occurrence of revivals and fractional revivals will vary from system to system, and it may not be easy, in practice, to identify the correct observables in all cases. However, the special nature of the interference between basis states at certain definite instants leads to revival phenomena, and this feature is closely linked to sudden changes in these expectation values at those instants. This feature is not necessarily traceable in all cases to the occurrence of an overall *exponential* factor in the expressions for the expectation values, although our analysis seems to indicate that a factor involving an exponential of periodic functions certainly plays a crucial role. Wave packet propagation in a Kerr-like medium provides us with a clean framework for illustrating these aspects, as it involves just a single pair of ladder operators, and the spectrum is not degenerate, in general. In the next

Chapter we therefore extend our investigations to initial photon-added coherent states propagating in a Kerr-like medium, and draw attention to the differences that arise due to the departure from perfect coherence of the initial state.

# CHAPTER 3

## Manifestations of wave packet revivals in the moments of observables - II

### 3.1 Introduction

In this chapter, we study the manner in which signatures of the revival phenomena which are manifested in the expectation values of observables depend on the extent of coherence enjoyed by the initial wave packet. For this purpose, we need to compare the details of the revival phenomena exhibited by an appropriate non-Gaussian initial state with that of an initial CS propagating in the nonlinear medium. As mentioned in Chapter 1, a suitable candidate for the initial state is the photon-added coherent state (PACS): it possesses the useful property of a precisely quantifiable, as well as tunable, degree of departure from perfect coherence. This property follows from the fact that a PACS can be obtained in principle by repeated addition of photons to a CS. The normalized  $m$ -photon-added coherent state  $|\alpha, m\rangle$  is defined as [41]

$$|\alpha, m\rangle = \frac{(a^\dagger)^m |\alpha\rangle}{\sqrt{\langle\alpha| a^m a^{\dagger m} |\alpha\rangle}} = \frac{(a^\dagger)^m |\alpha\rangle}{\sqrt{m! L_m(-\nu)}}. \quad (3.1)$$

where  $m$  is a positive integer,  $\nu = |\alpha|^2$  as before, and  $L_m(-\nu)$  is the Laguerre polynomial of order  $m$ . Setting  $m = 0$ , we retrieve the CS  $|\alpha\rangle$ . The mean photon number in the PACS  $|\alpha, m\rangle$  is given by [41]

$$\langle\mathbf{N}\rangle_m = \frac{(m+1) L_{m+1}(-\nu)}{L_m(-\nu)} - 1, \quad (3.2)$$

When  $\nu = 0$ ,  $\langle\mathbf{N}\rangle_m$  reduces to  $m$ , as required. When  $\nu \gg m$ , we can show that  $\langle\mathbf{N}\rangle_m = \nu + 2m + \mathcal{O}(\nu^{-1})$ . The plot of  $(\langle\mathbf{N}\rangle_m - \nu)$  versus  $\nu$  in Fig. 3.1 shows how the ordinate saturates to the value  $2m$  as  $\nu$  increases. The extent of departure of



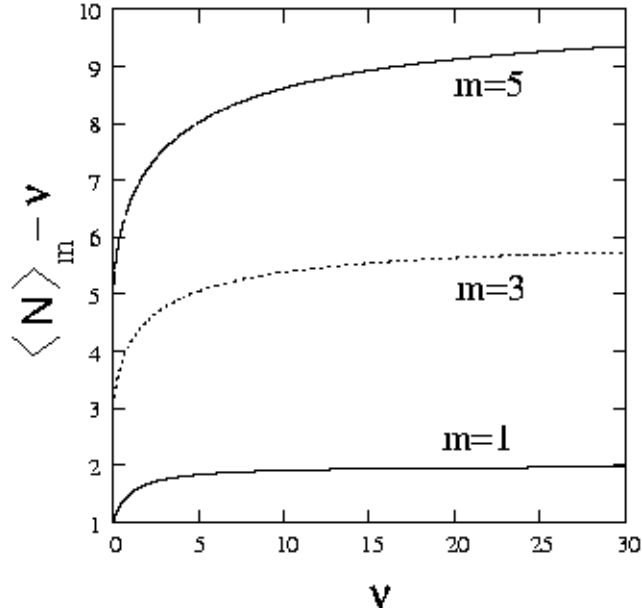


Figure 3.1:  $(\langle \mathbf{N} \rangle_m - \nu)$  versus  $\nu$  for  $m = 1, 3$  and  $5$ .

a PACS from perfect coherence clearly becomes more pronounced with increasing  $m$ . A PACS also possesses other interesting properties which may be kept in mind when we investigate its dynamics. For instance, in contrast to a CS, it exhibits phase-squeezing and sub-Poissonian statistics [13]. The latter implies that the standard deviation of the photon number operator  $\mathbf{N}$  behaves like  $\langle \mathbf{N} \rangle^{\frac{1}{2}-\beta}$  rather than  $\langle \mathbf{N} \rangle^{\frac{1}{2}}$ , the exponent  $\beta$  being a calculable decreasing function of  $m$ .

The PACS is also a *nonlinear* coherent state in the sense that it is an eigenstate of a nonlinear annihilation operator [44], namely,

$$\left(1 - \frac{m}{1 + a^\dagger a}\right) a |\alpha, m\rangle = \alpha |\alpha, m\rangle. \quad (3.3)$$

The state  $|\alpha, m\rangle$  can also be viewed in yet another way. Instead of the Fock basis  $\{|n\rangle\}$ , we may consider the unitarily transformed basis  $\{|n, \alpha\rangle\}$  formed by the *generalized coherent states*

$$|n, \alpha\rangle = e^{\alpha a^\dagger - \alpha^* a} |n\rangle. \quad (3.4)$$

Equivalently, for a given  $n$ , the generalized coherent state  $|n, \alpha\rangle$  is simply the state  $(a^\dagger - \alpha^*)^n |\alpha\rangle$ , normalized to unity. It can now be shown that, for a given  $m$ , the

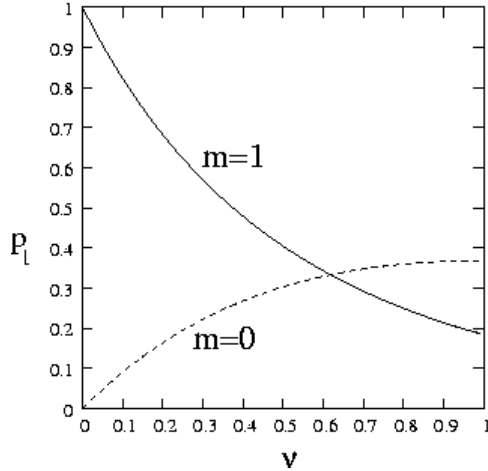


Figure 3.2: Probability of single-photon content versus  $\nu$  in a CS ( $m = 0$ ) and in a 1-photon-added CS ( $m = 1$ ).

state  $|\alpha, m\rangle$  is a *finite* superposition of the form  $\sum_{n=0}^m c_n |n, \alpha\rangle$ .

We further note that the single-photon-added coherent state recently generated in experiments [27] has a higher probability  $p_1$  of single-photon content than an ideal CS for sufficiently small values of  $\nu$ , as may be seen from Fig. 3.2. (It is straightforward to show that this happens for  $\nu < (\sqrt{5} - 1)/2 \simeq 0.618$ .) In this sense, a PACS would seem to be preferable to a CS for single-photon experiments.

With this brief introduction to the properties of a PACS, we proceed to examine the details of its dynamics as it propagates in a nonlinear medium. The latter is once again modeled by the Hamiltonian of Eq. (2.2).

## 3.2 Dynamics of photon-added coherent states propagating in a nonlinear medium

As in the case of an initial CS, we examine the moments and variances of the hermitian operators  $x$  and  $p$ , defined in Eq. (2.14), as the single-mode field evolves from the initial PACS of Eq. (3.1) under the Kerr-like Hamiltonian. We shall use

the convenient notation

$$\langle x(t) \rangle_m = \langle \alpha, m | e^{iHt/\hbar} x e^{-iHt/\hbar} | \alpha, m \rangle, \quad (3.5)$$

with an analogous definition for  $\langle p(t) \rangle_m$ . As  $H$  is diagonal in the number operator  $\mathbf{N}$ , it follows that the mean photon number  $\langle \mathbf{N} \rangle_m$ , as well as its higher moments, and hence the sub-Poissonian statistics of the photon number, remain unaltered in time.

We recall from Chapter 2 that, at the level of the first moments, the dynamical equations in the case of an initial CS are those of a classical nonlinear oscillator, with a certain re-parametrization of time. In contrast, the time dependences of  $\langle x(t) \rangle_m$  and  $\langle p(t) \rangle_m$  (i. e., averages obtained in the time-evolved  $m$ -photon-added coherent state with  $m \neq 0$ ) differ in striking ways from the foregoing, even for small values of  $m$ . The revival time  $T_{\text{rev}}$  remains equal to  $\pi/\chi$ , of course, but in the intervals between revivals the time evolution is considerably more involved than the expressions in Eqs. (2.19) and (2.20) for the case  $m = 0$ . This implies that even a small departure from coherence in the initial state and from Poissonian number statistics leads to a very different time evolution of the system and the phase squeezing it exhibits. We have calculated analytically the exact expressions for  $\langle x(t) \rangle_m$  and  $\langle p(t) \rangle_m$  in Appendix B, and these are given in Eqs. (B.3) and (B.4). The initial values of these expectation values in the PACS  $|\alpha, m\rangle$  are

$$\langle x(0) \rangle_m = \frac{L_m^1(-\nu)}{L_m(-\nu)} x_0, \quad \langle p(0) \rangle_m = \frac{L_m^1(-\nu)}{L_m(-\nu)} p_0, \quad (3.6)$$

where  $L_m^1(-\nu) = dL_{m+1}(-\nu)/d\nu$  is an associated Laguerre polynomial,  $x_0 = \sqrt{2} \text{Re } \alpha$ , and  $p_0 = \sqrt{2} \text{Im } \alpha$ . Analogous to the variables  $X$  and  $P$  in the case of the CS given by Eq. (2.29) of Chapter 2, let us define

$$\left. \begin{aligned} X_m(t) &= \langle x(t) \rangle_m \exp[\nu(1 - \cos 2\chi t)], \\ P_m(t) &= \langle p(t) \rangle_m \exp[\nu(1 - \cos 2\chi t)]. \end{aligned} \right\} \quad (3.7)$$

(Thus  $X_0$  and  $P_0$  are just the quantities  $X$  and  $P$  of the preceding chapter.) The solutions for these quantities may then be written in the following compact and

suggestive form (derived in Appendix B, Eqs. (B.11) and Eqs. (B.12)):

$$\left. \begin{aligned} X_m(t) &= x_0 \operatorname{Re} z_m(t) + p_0 \operatorname{Im} z_m(t), \\ P_m(t) &= p_0 \operatorname{Re} z_m(t) - x_0 \operatorname{Im} z_m(t), \end{aligned} \right\} \quad (3.8)$$

where

$$z_m(t) = \frac{L_m^1(-\nu e^{2i\chi t})}{L_m(-\nu)} \exp[i(2m\chi t + \nu \sin 2\chi t)]. \quad (3.9)$$

A number of differences between these results and those for the case  $m = 0$  are noteworthy. First,  $|z_m|$  varies with  $t$ , in contrast to  $|z_0(t)| \equiv 1$ . (Note also that  $z_m(0) = L_m^1(-\nu)/L_m(-\nu) \neq 1$ .) The time dependence of  $X_m$  and  $P_m$  involves the sines and cosines of the set of arguments  $(2\chi lt + \nu \sin 2\chi t)$ , where  $l = m, \dots, 2m$ . Thus, not only are higher harmonics present, but the arguments also involve *secular* (linear) terms in  $t$  added to the original  $(\nu \sin 2\chi t)$ . This important difference precludes the possibility of subsuming the time dependence into that of an effective nonlinear oscillator by means of a re-parametrization of the time, in contrast to the case  $m = 0$ .

We present the rest of our results with the help of figures based on numerical computation. As in Chapter 2, we have set  $\chi = 5$  for definiteness. (Our results on wave packet dynamics will hold good for any other value of  $\chi$  as well. The numerical value of  $\chi$  merely sets a time scale.) Again, as before, we restrict ourselves to the case  $x_0 = p_0$  (there is no significant loss of generality as a result of this symmetric choice of parameters). As before, the presence of the overall factor  $\exp[-\nu(1 - \cos 2\chi t)]$  in the expressions for  $\langle x(t) \rangle_m$  and  $\langle p(t) \rangle_m$  implies that, for sufficiently large values of the parameter  $\nu$ , the expectation values remain essentially static around the value zero, and burst into rapid variation only in the neighborhood of revivals. Smaller values of  $\nu$  enable us to resolve the details of the time variation more clearly.

Figures 3.3 (a) and (b) are, respectively, plots of the expectation values  $\langle x(t) \rangle_1$  and  $\langle x(t) \rangle_{10}$  versus  $t/T_{\text{rev}}$  for parameter values  $x_0 = p_0 = 1$  (i.e., for  $\nu = 1$ ). The revivals at integer values of  $t/T_{\text{rev}}$  are manifest. With increasing  $m$  (or a decreasing degree of coherence in the initial state), the relatively smooth behavior of  $\langle x(t) \rangle_0$

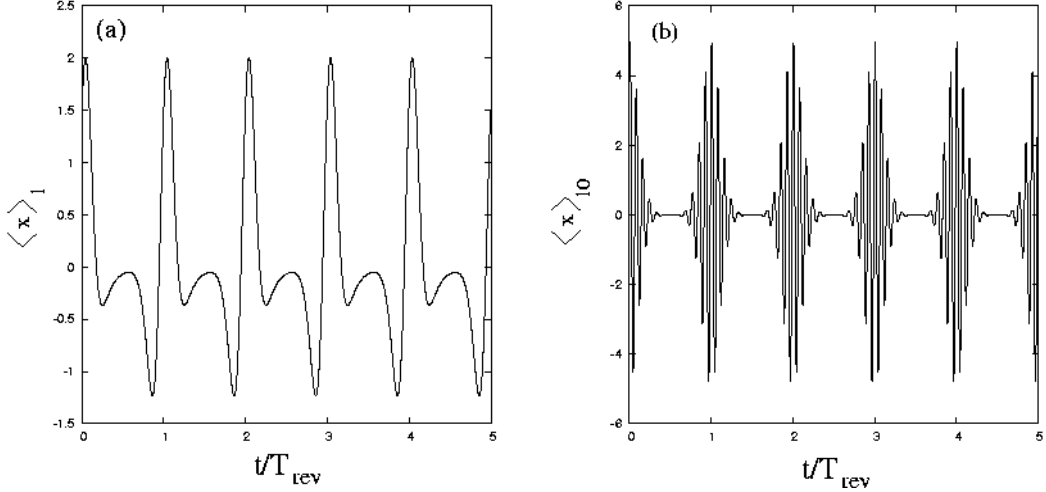


Figure 3.3:  $\langle x(t) \rangle$  as a function of  $t/T_{\text{rev}}$  for a PACS (a)  $|\alpha, 1\rangle$  and (b)  $|\alpha, 10\rangle$ , with  $\nu = 1$ .

gives way to increasingly rapid oscillatory behavior in the vicinity of revivals. This is to be compared with Fig. 2.1 (a), the corresponding plot for an initial CS. The range over which the expectation value varies also increases for larger values of  $m$ .

Essentially the same sort of behavior is shown by  $\langle p(t) \rangle_m$ . However, a “phase plot” of  $\langle p(t) \rangle_m$  versus  $\langle x(t) \rangle_m$  in Figs. 3.4 (a) and (b) reveals complementary aspects of such oscillatory behavior with increasing  $m$ , showing how the oscillations in the two quantities go in and out of phase with each other. The entire closed curve in each case is traversed in a time period  $T_{\text{rev}}$ .

As in the case of an initial CS, here too the initial state undergoes fractional revivals in the interval between any two successive revivals at the instants  $T_{\text{rev}}/k$  where  $k = 2, 3, \dots$ , and also, for any given  $k$ , at the instants  $jT_{\text{rev}}/k$  where  $j = 1, 2, \dots, (k-1)$ . These fractional revivals at the instants  $jT_{\text{rev}}/k$  also show up in the rapid pulsed variation of the  $k^{\text{th}}$  moments of  $x$  and  $p$ , and not in the lower moments. However, there is a crucial difference if we use  $|\alpha, m\rangle$  as the initial state: then, even for relatively small values of  $m$ , the signatures of fractional revivals appear for values of  $\nu$  that are not large, in contrast to what happens when the initial state is the coherent state  $|\alpha\rangle$ . (Recall that  $\langle \mathbf{N} \rangle_m$  is determined by  $\nu$  according to Eq. (3.2).)

For illustrative purposes we investigate the specific case of the fractional revival

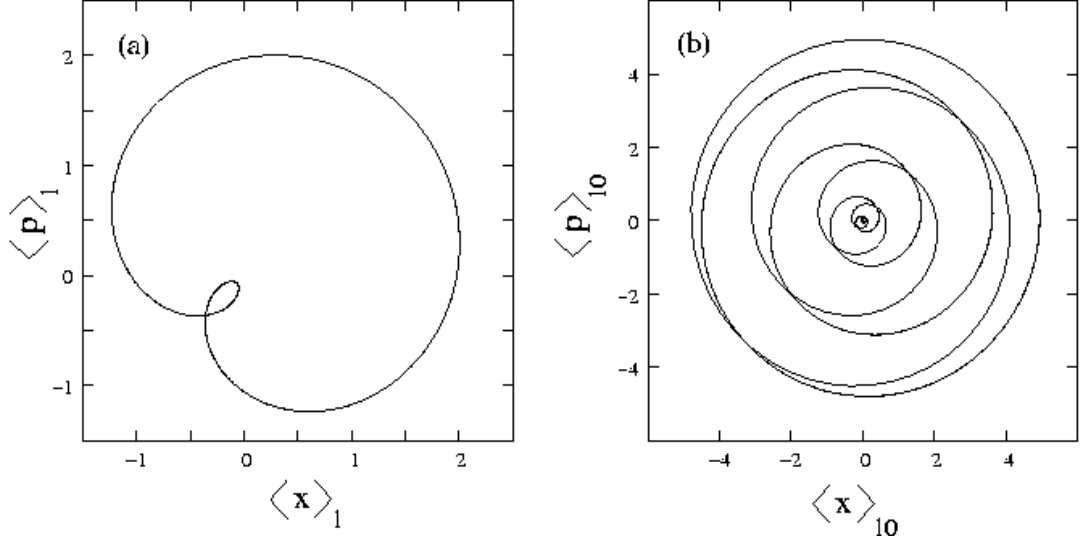


Figure 3.4: “Phase plot” of  $\langle p \rangle$  vs  $\langle x \rangle$  for an initial PACS (a)  $|\alpha, 1\rangle$  and (b)  $|\alpha, 10\rangle$ , with  $\nu = 1$ .

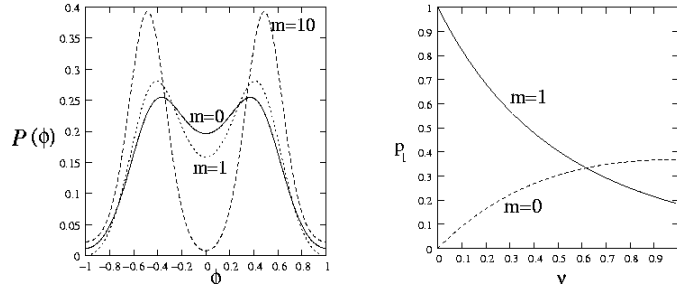


Figure 3.5: Phase distribution  $P(\phi)$  versus  $\phi$  in units of  $\pi$ , for  $\nu = 0.3$  and  $m = 0, 1$  and  $10$ .

at  $t = \frac{1}{2}T_{\text{rev}}$ . This corresponds to the appearance of two spatially separated similar wave packets, i. e., a single qubit in the language of logic gate operations.

At this instant the overlap between the two sub-packets in the wave function corresponding to the state  $|\psi(T_{\text{rev}}/2)\rangle$  decreases significantly with an increase in  $m$ . This feature emerges clearly in a plot of the phase distribution  $P(\phi)$  versus the angular variable  $\phi$  (shown in Fig. 3.5 for  $\nu = 0.3$  and  $m = 0, 1$  and  $10$ ). This phase distribution is defined as [45]

$$P(\phi) = \frac{1}{2\pi} |\langle \phi | \psi(T_{\text{rev}}/2) \rangle|^2, \quad |\phi\rangle = \sum_{n=0}^{\infty} e^{in\phi} |n\rangle. \quad (3.10)$$

In this sense, a PACS is better suited than a CS for performing single qubit oper-

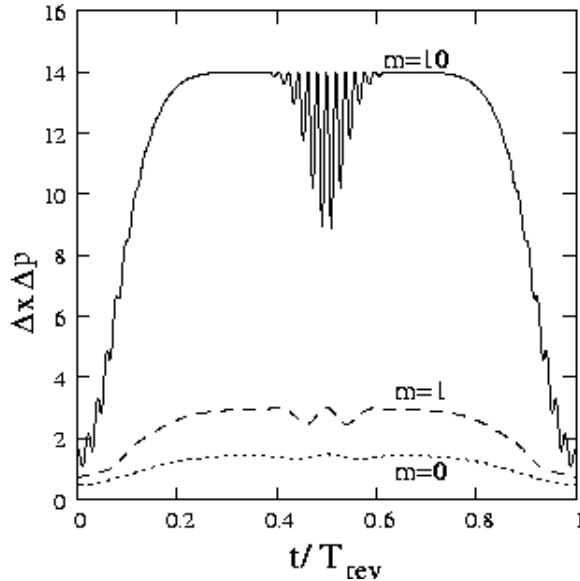


Figure 3.6: Variation of the uncertainty product with  $t/T_{\text{rev}}$  for an initial CS ( $m = 0$ ) and initial PACS  $|\alpha, 1\rangle$  and  $|\alpha, 10\rangle$  with  $\nu = 1$ .

ations treating the two sub-packets as qubits  $|0\rangle$  and  $|1\rangle$ , respectively. Similarly, at  $t = \frac{1}{4}T_{\text{rev}}$ , the overlap between the four sub-packets is significantly smaller in the case of an initial PACS than in the case of an initial CS, and this feature becomes more pronounced with increasing  $m$ . The sub-packets therefore behave as genuine orthogonal basis states in the former case even for relatively small values of  $\nu$ . Hence the quantum logic approach to wave packet control for the purpose of implementing two-qubit operations, outlined in Ref. [25], is more feasible with an initial state that is a PACS rather than a CS.

Plots of the product  $\Delta x \Delta p$  of the standard deviations of  $x$  and  $p$  versus  $t/T_{\text{rev}}$  over a full cycle are shown in Fig. 3.6 for initial states given, respectively, by the coherent state  $|\alpha\rangle$  (dotted curve), the photon-added state  $|\alpha, 1\rangle$  (dashed curve), and the 10-photon-added state  $|\alpha, 10\rangle$  (bold curve), for  $\chi = 5$ ,  $x_0 = p_0 = 1$ , so that  $\nu = 1$ . It is seen that hardly any trace of the fractional revival is evident in the case of an initially coherent state, in marked contrast to the case of the photon-added states, in which the fractional revival is signaled by oscillations whose frequency and amplitude increase quite rapidly with increasing  $m$ . This effect gets masked for larger values of the parameter  $\nu$ , when these oscillations are relatively insensitive to the value of  $m$ . Another striking feature that provides a

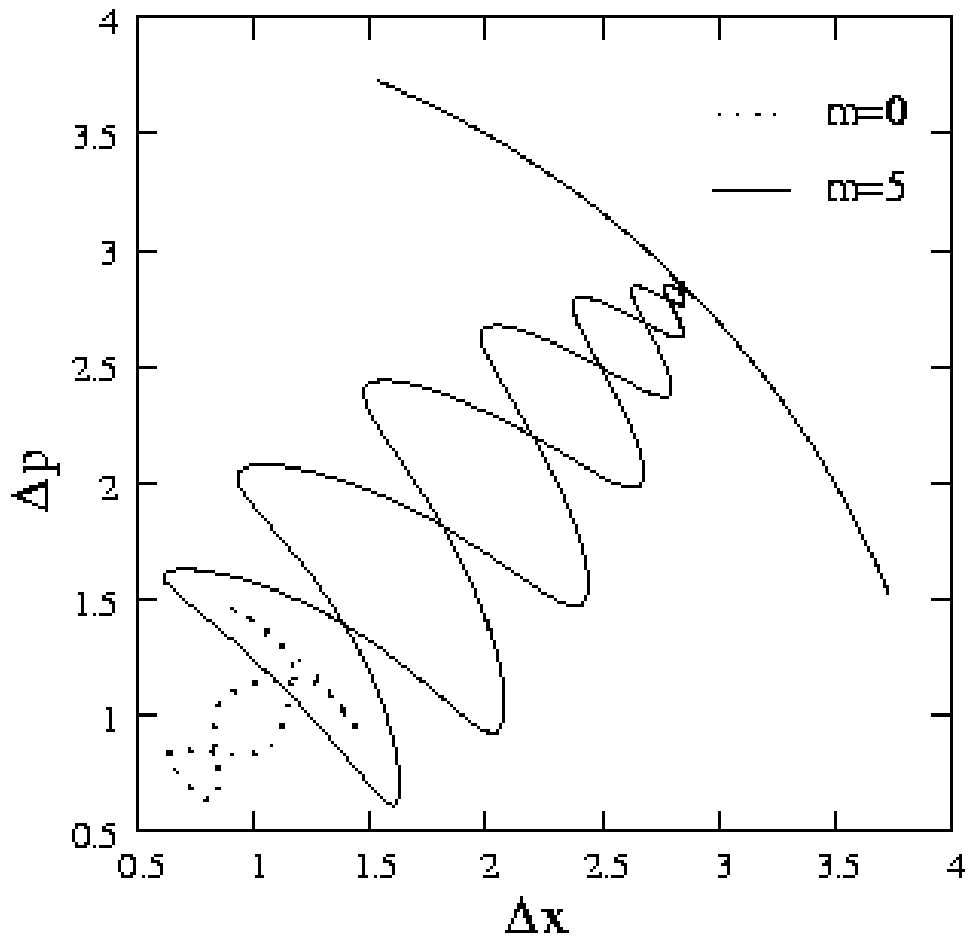


Figure 3.7: “Phase plots” of  $\Delta p$  and  $\Delta x$  for  $\nu = 1$ , for an initial CS ( $m = 0$ ) and an initial PACS  $|\alpha, 5\rangle$ .



clear distinction between the revivals at  $t = n T_{\text{rev}}$  and the fractional revivals at  $t = (n + \frac{1}{2}) T_{\text{rev}}$  (where  $n$  is a positive integer) is illustrated in Fig. 3.7, which is a plot of  $\Delta p$  versus  $\Delta x$ . The dotted and full lines in the same plot correspond to  $m = 0$  and  $m = 5$ , respectively, making ready comparison possible. We recall from Chapter 2, Figs. 2.4 (a)-(c) that for an initial CS these standard deviations start from an initial value  $\frac{1}{2}$ . As  $t$  increases, they rapidly build up, oscillating about the radial  $\Delta p = \Delta x$  line with an initially increasing, and then decreasing, amplitude. A maximum value of  $\Delta x$  and  $\Delta p$  is attained, at which these quantities then remain nearly static, till the onset of the fractional revival at  $T_{\text{rev}}$ . They then begin to oscillate rapidly once again, but this time in a *tangential* direction, swinging back and forth along an arc with an amplitude that initially increases and then decreases to zero: in other words, the individual standard deviations fluctuate rapidly in the vicinity of the fractional revival (while  $[(\Delta x)^2 + (\Delta p)^2]^{1/2}$  remains essentially unchanged in magnitude), in marked contrast to what happens at a revival. It is evident from Fig. 3.7 that all these features are very significantly enhanced and magnified for non-zero values of  $m$ , relative to what happens for the case  $m = 0$ .

Similar signatures of fractional revivals for higher values of  $k$  can be picked out by using initial states  $|\alpha, m\rangle$ , even with relatively small values of  $\nu$ . The oscillations in the moments of observables become more pronounced with increasing  $m$ . For instance, signatures of the fractional revivals at  $t = \frac{1}{4}j T_{\text{rev}}$ ,  $j = 1, 2, 3$  are clearly discernible in the behavior of the fourth moments of  $x$ . Figure 3.8 is a plot of  $\langle(\delta p)^4\rangle$  versus  $\langle(\delta x)^4\rangle$  where  $\delta x = x - \langle x \rangle$ ,  $\delta p = p - \langle p \rangle$ , for  $\nu = 1$ . The dotted and full lines correspond to the initial states  $|\alpha\rangle$  and  $|\alpha, 2\rangle$ , respectively.

### 3.3 Concluding remarks

We have shown that distinctive signatures of wave packet revivals and fractional revivals are displayed in the temporal evolution of appropriate variables, enabling identification of departure from coherence of the initial state. These distinctions between an initial CS and an initial PACS are, however, clearly seen only for small

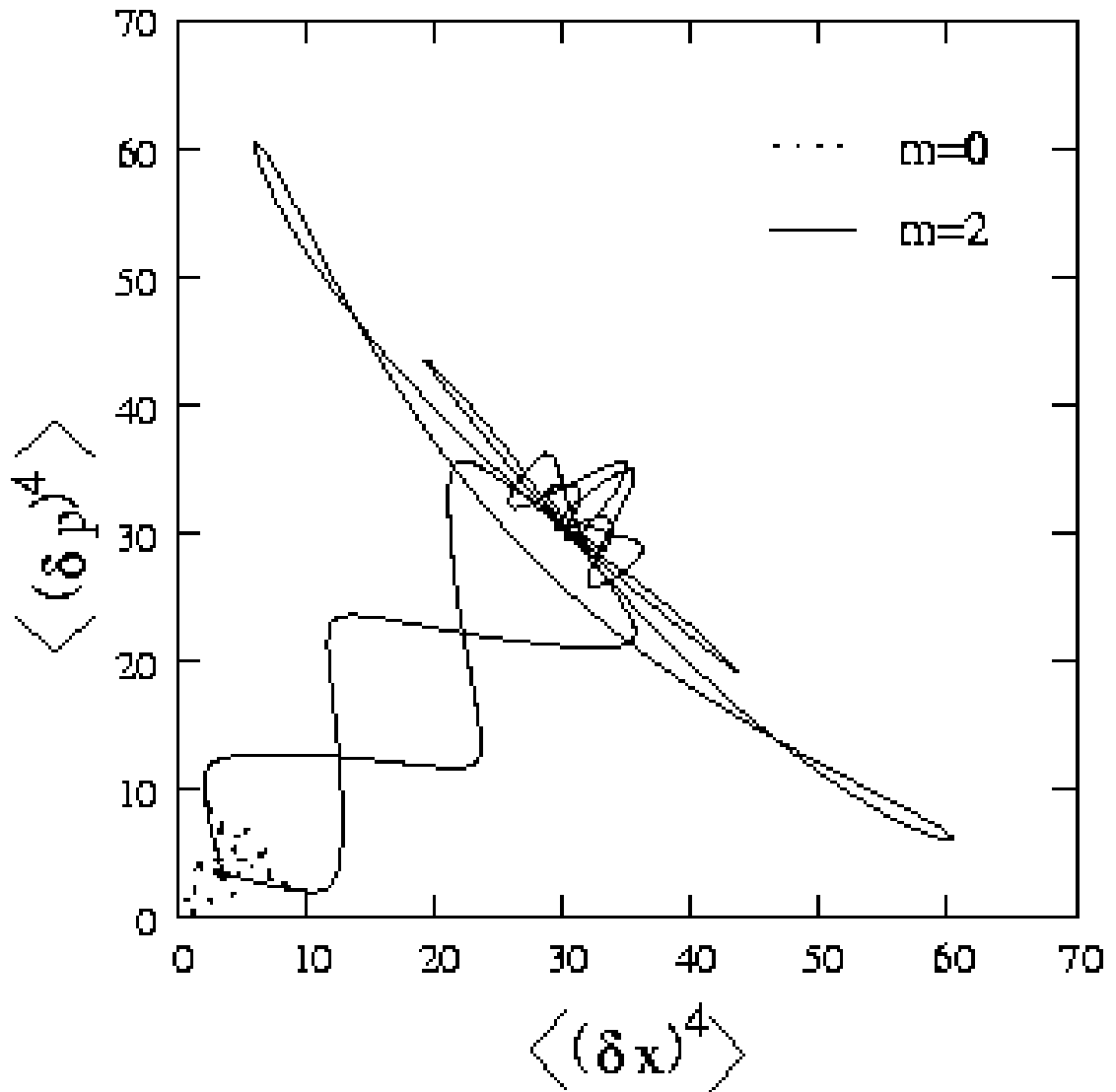


Figure 3.8: “Phase plots” of  $\langle (\delta p)^4 \rangle$  and  $\langle (\delta x)^4 \rangle$  for  $\nu = 1$ , for an initial CS and an initial PACS  $|\alpha, 2\rangle$ .

values of  $\nu$ . This is related to the fact that, for small values of  $\nu$ , the probability of the  $m$ -photon content of an  $m$ -photon-added coherent state is substantially larger than that of the CS. Another difference between these states emerges during their temporal evolution: the addition of even a single photon washes out the squeezing property displayed by an initial CS at specific instants. In the next Chapter, we examine the squeezing and higher-order squeezing properties of these states as they propagate in a Kerr-like medium.

# CHAPTER 4

## Squeezing and higher-order squeezing in wave packet dynamics

### 4.1 Introduction

In this chapter, we investigate the squeezing and higher-order squeezing properties of an initial PACS as it propagates in a Kerr-like medium. In particular, we examine the precise manner in which departure from coherence of the initial state affects its squeezing properties in the neighborhood of revivals and fractional revivals.

For ready reference, we first summarize the conditions under which a generic state is said to display squeezing or higher-order squeezing [46]. Consider two arbitrary Hermitian operators  $A$  and  $B$  with a commutator

$$[A, B] = iC. \quad (4.1)$$

The generalized uncertainty relation satisfied by these operators in any state is

$$\Delta A \Delta B \geq \frac{1}{2} |\langle C \rangle|. \quad (4.2)$$

The state is said to be squeezed in the observable  $A$  if

$$(\Delta A)^2 < \frac{1}{2} |\langle C \rangle|. \quad (4.3)$$

A similar definition holds for  $B$ .

In particular, for the quadrature variables  $x$  and  $p$  defined in Eq. (2.14), this implies that  $x$  (or  $p$ ) is squeezed if  $\Delta x$  (or  $\Delta p$ )  $< 1/\sqrt{2}$  in the state concerned.

Several states satisfying this squeezing property have been investigated in the literature [9]. Some examples are the squeezed vacuum state, squeezed number states, and photon-added coherent states. Proposals for the generation, and detection of squeezed states, as well as their potential applications, have been outlined in the literature [47, 48].

Of direct relevance to us is the squeezing property displayed by the  $m$ - photon-added coherent state  $|\alpha, m\rangle$ . A general result for this state is as follows. Consider the hermitian operators

$$A_\varphi = \frac{ae^{i\varphi} + a^\dagger e^{-i\varphi}}{\sqrt{2}} \quad \text{and} \quad B_\varphi = \frac{ae^{i\varphi} - a^\dagger e^{-i\varphi}}{i\sqrt{2}}, \quad (4.4)$$

satisfying the commutation relation  $[A_\varphi, B_\varphi] = i$  for any value of  $\varphi$ . For  $\varphi = 0$ ,  $A_\varphi$  and  $B_\varphi$  reduce to quadrature variables  $x$  and  $p$ . It can be shown that the variance of  $A_\varphi$  in the state  $|\alpha, m\rangle$  is given by [41]

$$\begin{aligned} (\Delta A_\varphi)^2 = & \left\{ 2\nu \left( L_m^2(-\nu)L_m(-\nu) - [L_m^1(-\nu)]^2 \right) \cos(2(\theta + \varphi)) - 2\nu [L_m^1(-\nu)]^2 \right. \\ & \left. - [L_m(-\nu)]^2 + 2(m+1)L_{m+1}(-\nu)L_m(-\nu) \right\} / \left\{ 2[L_m(-\nu)]^2 \right\}, \quad (4.5) \end{aligned}$$

where  $\alpha = \nu^{1/2}e^{i\theta}$  as before. Setting  $m = 0$  in the above equation and simplifying, we retrieve the corresponding expression for a CS  $|\alpha\rangle$ , namely,  $(\Delta A_\varphi)^2 = \frac{1}{2}$ . As is well known, the CS is not a squeezed state. It is in fact a minimum uncertainty state in the observables  $x$  and  $p$  with  $\Delta x = \Delta p = 1/\sqrt{2}$ . Choosing the phases such that  $\theta + \varphi = \pi$ , a plot of  $(\Delta A_\varphi)^2$  versus  $|\alpha|$  shows that almost 50% squeezing can be obtained over a wide range of values of  $|\alpha|$ , for non-zero values of  $m$ .

The concept of higher-order squeezing was first introduced by Hong and Mandel [49]. A state is said to be squeezed to order  $2q$  ( $q = 1, 2, 3, \dots$ ) in the operator  $A$  if  $\langle (\delta A)^{2q} \rangle$  in that state is less than the corresponding value obtained for a CS, where  $\delta A = A - \langle A \rangle$ . For the quadrature variable  $x$ , this reduces to the requirement

$$\langle (\delta x)^{2q} \rangle < \frac{1}{2^q} (2q - 1)!! \quad (4.6)$$

Another type of higher-order squeezing, called amplitude-squared squeezing, was

defined first by Hillery [50], and generalized subsequently by Zhang *et al.* to  $q^{\text{th}}$ -power amplitude-squeezing [51]. (Amplitude-squared squeezing corresponds to the case  $q = 2$ .) One considers the two quadrature variables

$$Z_1 = \frac{(a^q + a^{\dagger q})}{\sqrt{2}} \quad \text{and} \quad Z_2 = \frac{(a^q - a^{\dagger q})}{i\sqrt{2}} \quad (q = 1, 2, 3, \dots). \quad (4.7)$$

The generalized uncertainty principle now reads

$$(\Delta Z_1)^2 (\Delta Z_2)^2 \geq \frac{1}{4} |\langle [Z_1, Z_2] \rangle|^2. \quad (4.8)$$

The state is said to be  $q^{\text{th}}$ -power amplitude-squeezed in the variable  $Z_1$  if

$$(\Delta Z_1)^2 < \frac{1}{2} |\langle [Z_1, Z_2] \rangle|. \quad (4.9)$$

Amplitude squeezing in  $Z_2$  is similarly defined. Let us write  $[a^q, a^{\dagger q}] = F_q(\mathbf{N})$ . This is a polynomial of order  $(q - 1)$  in the number operator  $\mathbf{N}$  (see Appendix C, Eq. (C.4)), given by

$$F_q(\mathbf{N}) = q! \left[ 1 + \sum_{n=1}^{q-1} \binom{q}{n} \frac{1}{n!} \left\{ \mathbf{N}(\mathbf{N} - 1) \cdots (\mathbf{N} - (n - 1)) \right\} \right]. \quad (4.10)$$

Let

$$D_q(t) = \frac{(\Delta Z_1)^2 - \frac{1}{2} \langle F_q(\mathbf{N}) \rangle}{\frac{1}{2} \langle F_q(\mathbf{N}) \rangle}. \quad (4.11)$$

(The time-dependence has been indicated explicitly in  $D_q(t)$  to remind us that the expectation values involved are those in the instantaneous state of the system.) It is easily seen that the state is  $q^{\text{th}}$ -power amplitude-squeezed in  $Z_1$  if  $-1 \leq D_q < 0$ . We can rewrite Eq. (4.11) in terms of  $a^q$  and  $a^{\dagger q}$  as

$$D_q(t) = \frac{2 \left[ \text{Re} \langle a^{2q} \rangle - 2 (\text{Re} \langle a^q \rangle)^2 + \langle a^{\dagger q} a^q \rangle \right]}{\langle F_q(\mathbf{N}) \rangle}. \quad (4.12)$$

We now examine the manner in which the extent of coherence of the initial state affects its subsequent squeezing properties. There is a considerable literature on this subject. For instance, dynamical squeezing of a PACS arising as a result

of the time-dependence of the frequency of the electromagnetic field oscillator in a cavity has been investigated [52]. The non-classical effects exhibited by an initial CS propagating in a Kerr-like medium [53], its Hong-Mandel squeezing properties [54], and its  $q^{\text{th}}$ -power amplitude-squeezing properties [55] have been discussed in the literature. We are interested specifically in the squeezing properties of wave packets propagating in a Kerr-like medium. In the next Section, we therefore summarize the results of [55] in this context, obtained for an initial CS. This will facilitate subsequent comparison between our work on the squeezing properties of an initial PACS [29] with those of an initial CS.

## 4.2 The case of an initial coherent state

When the initial CS evolves under the Hamiltonian of Eq. (2.2), the (time-dependent) expectation values on the RHS of Eq. (4.12) can be evaluated [55] using Eq. (2.21). The result is the expression for  $D_q(t)$  given in Eq. (C.6), Appendix C.

We are interested, in particular, in examining whether fractional revivals are accompanied by any significant degree of squeezing and higher-order squeezing. For this purpose, we focus on  $D_q(t)$  at a 2-sub-packet fractional revival. Setting  $t = \pi/(2\chi)$  in Eq. (C.6) (Appendix C) and simplifying, we get

$$D_q(T_{\text{rev}}/2) = \frac{2\nu^q}{\langle F_q(\mathbf{N}) \rangle} \left\{ 1 + (-1)^{q-1} \cos 2q\theta - 2e^{-4\nu \sin^2 q\pi/2} \cos^2 q\theta \right\}. \quad (4.13)$$

As before,  $\theta$  is the argument of  $\alpha (= \nu^{1/2} e^{i\theta})$ . It is evident that  $D_q$  vanishes at this instant for all even values of  $q$ , implying that no even-order squeezing of the state accompanies this fractional revival. For odd values of  $q$ , however, we find

$$D_q(T_{\text{rev}}/2) = \frac{4\nu^q}{\langle F_q(\mathbf{N}) \rangle} (\sin^2 q\theta - e^{-4\nu} \cos^2 q\theta). \quad (4.14)$$

Thus squeezing (or higher-order squeezing) occurs at this instant, provided  $D_q < 0$ , i.e.,  $|\tan q\theta| < e^{-2\nu}$ . We illustrate this in Figs. 4.1(a) and (b), where  $D_1$  and  $D_3$  are plotted as functions of  $\nu$  for an initial CS with  $\theta = 0$ . (Once again, we have

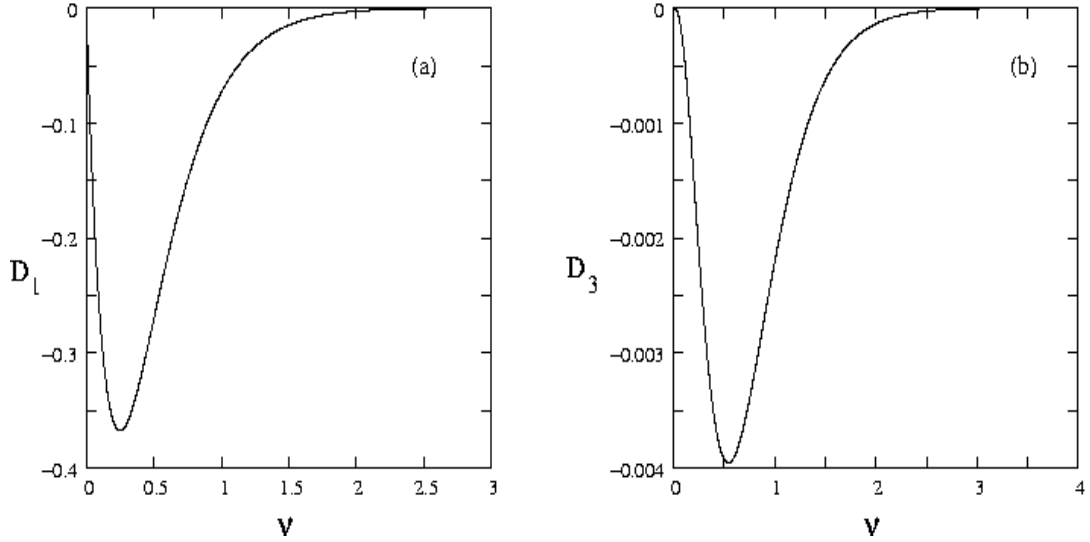


Figure 4.1:  $D_q(\frac{1}{2}T_{\text{rev}})$  versus  $\nu$  for an initial CS (with  $\theta = 0$ ), for (a)  $q = 1$  and (b)  $q = 3$ . (Note the different ordinate scales in the two cases.)

set  $\chi = 5$  in all the numerical results presented in this Chapter.) We have also

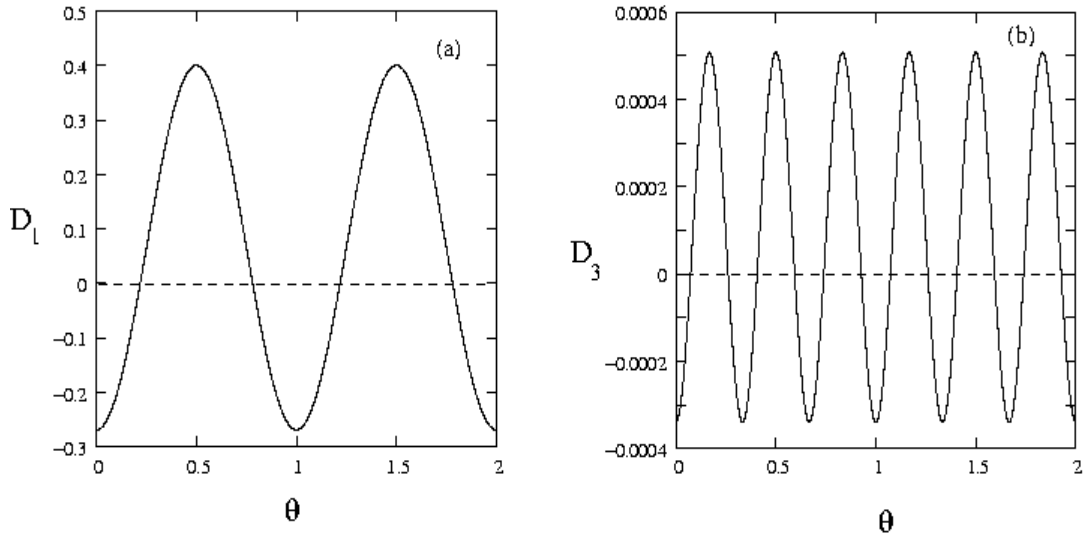


Figure 4.2:  $D_q(\frac{1}{2}T_{\text{rev}})$  versus  $\theta$  for an initial CS (with  $\nu = 0.1$ ), for (a)  $q = 1$  and (b)  $q = 3$ .

plotted  $D_1$  and  $D_3$  as functions of  $\theta$  for a fixed value of  $\nu (= 0.1)$  in Figs. 4.2(a) and (b), showing how squeezing occurs for certain ranges of the argument of  $\alpha$ , when  $D_q$  becomes negative.

An interesting feature is that the CS spreads and loses its coherence almost immediately after it starts propagating in the medium. This is borne out by the fact that it becomes squeezed even within a very short time of propagation [55] as



seen in Fig. 4.3, which is a plot of  $D_q$  versus  $t/T_{rev}$  for an initial CS with  $\nu = 10$ . Further, we see that close to  $t = 0$  the state not only displays squeezing, but also higher-order squeezing, for both odd and even integer values of  $q$ .

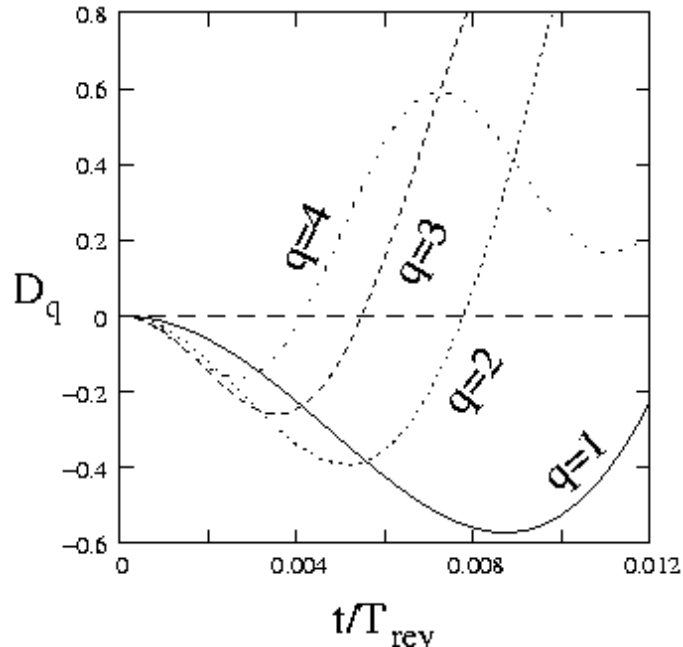


Figure 4.3:  $D_q$  versus  $t/T_{rev}$  for an initial CS with  $\nu = 10$ , for  $q = 1, 2, 3$  and  $4$ .

In the light of these results, we are in a position to investigate the dynamics of an initial PACS and compare it with that of an initial CS.

### 4.3 The case of an initial PACS

We show that if the initial state departs even marginally from coherence, as in a PACS with a small value of  $m$ , the results of the preceding Section change significantly. Writing  $D_q$  as  $D_q^{(m)}$  (for ready identification) when the expectation values in Eq. (4.12) are evaluated for an initial state  $|\alpha, m\rangle$ , we find the following

general result:

$$\begin{aligned}
\frac{1}{2}L_m(-\nu) \langle F_q(\mathbf{N}) \rangle_m D_q^{(m)}(t) &= e^{-\nu(1-\cos 4\chi qt)} \sum_{n=0}^m \binom{m+2q}{n+2q} \frac{\nu^{n+q}}{n!} \\
&\times \cos \left[ 2(2m+2n+2q-1)\chi qt + \nu \sin 4\chi qt - 2q\theta \right] \\
&- \frac{2e^{-2\nu(1-\cos 2\chi qt)}}{L_m(-\nu)} \left\{ \sum_{n=0}^m \binom{m+q}{n+q} \frac{\nu^{n+q/2}}{n!} \right. \\
&\times \left. \cos \left[ (q-1+2m+2n)\chi qt + \nu \sin 2\chi qt - q\theta \right] \right\}^2 \\
&+ \sum_{n=n_{\min}}^q \binom{q}{n} \frac{m!}{(m-q+n)!} \nu^n L_m^n(-\nu), \quad (4.15)
\end{aligned}$$

where  $n_{\min} = \max(0, q-m)$ . The derivation of the expression above is given in Appendix C. It is the generalization of the expression for  $D_q \equiv D_q^{(0)}$  obtained for a coherent state. As before, we examine  $D_q^{(m)}$  at  $t = \frac{1}{2}T_{\text{rev}}$  for possible squeezing and higher-order squeezing of the state at that instant. The foregoing expression reduces at this instant of time to

$$\begin{aligned}
\frac{1}{2}L_m(-\nu) \langle F_q(\mathbf{N}) \rangle_m D_q^{(m)}(T_{\text{rev}}/2) &= (-\nu)^q L_m^{2q}(-\nu) \cos 2q\theta \\
&- \frac{2e^{-2\nu(1-\cos q\pi)}}{L_m(-\nu)} \nu^q \left\{ L_m^q((-1)^q \nu) \right\}^2 \cos^2 q\theta \\
&+ \sum_{n=n_{\min}}^q \binom{q}{n} \frac{m!}{(m-q+n)!} \nu^n L_m^n(-\nu). \quad (4.16)
\end{aligned}$$

We use this to analyze various cases numerically. In contrast to what happens for an initial CS, it turns out that there is no *odd*-power amplitude-squeezing for an initial PACS. Even-power amplitude-squeezing does occur, though, for sufficiently large values of  $\nu$ . This is illustrated in Figs. 4.4(a) and (b), which show the ranges of  $\nu$  for which  $D_2^{(m)}$  falls below zero. Figures 4.5(a) and (b) depict the variation of  $D_2^{(m)}$  with the phase angle  $\theta$  for a fixed value of  $\nu$ .

Turning to the extent of squeezing as a function of time, in Fig. 4.6 we compare the temporal variation of the standard deviation  $\Delta x$  for an initial CS ( $m=0$ ) and an initial PACS ( $m=1$ ), with  $\alpha=1$  (hence  $\theta=0$ ). The horizontal dashed

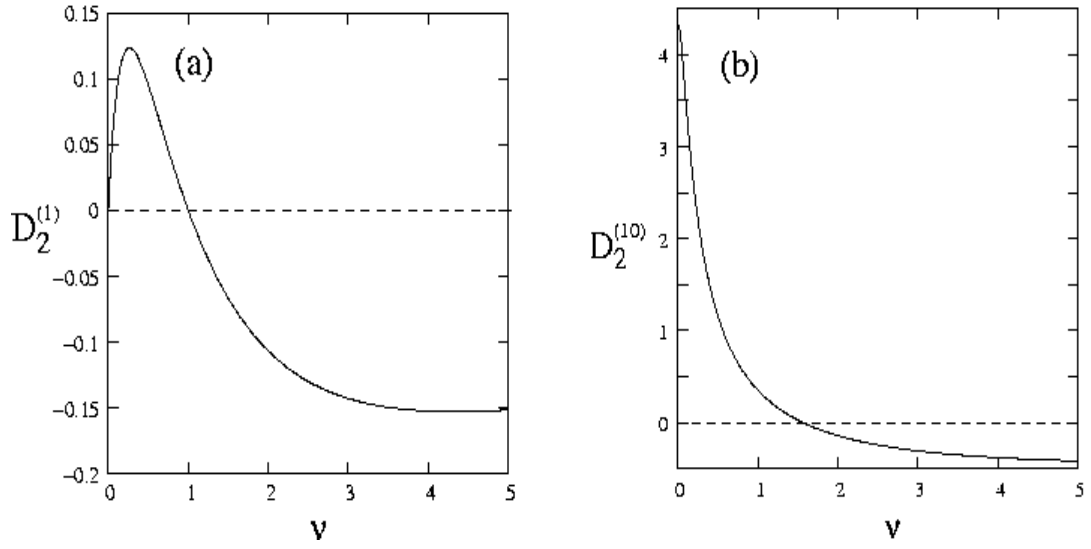


Figure 4.4:  $D_2^{(m)}(\frac{1}{2}T_{\text{rev}})$  versus  $\nu$  (with  $\theta = 0$ ), for an initial PACS with (a)  $m = 1$  and (b)  $m = 10$ .

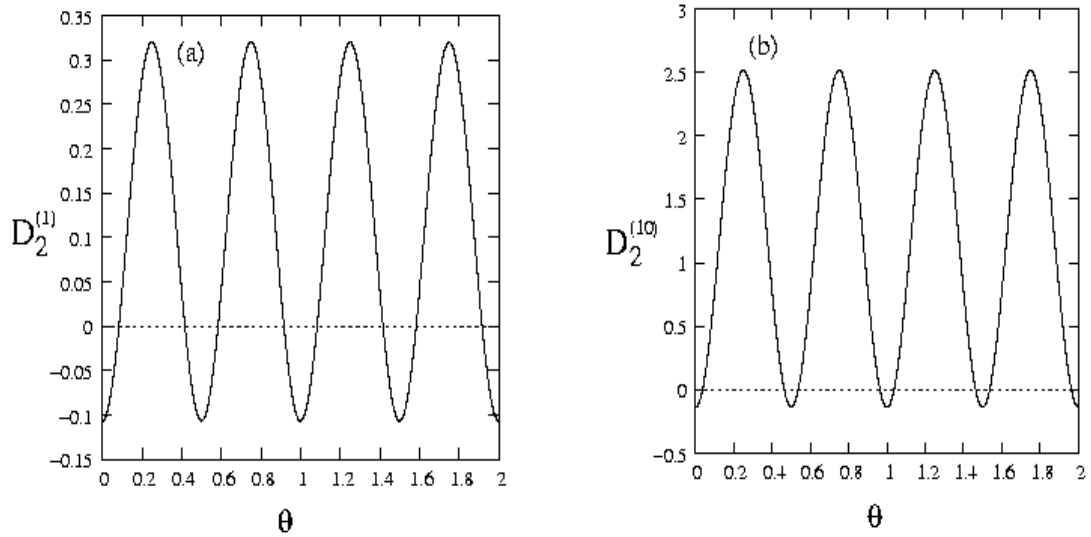


Figure 4.5:  $D_2^{(m)}(\frac{1}{2}T_{\text{rev}})$  versus  $\theta$  (with  $\nu = 2$ ), for an initial PACS with (a)  $m = 1$  and (b)  $m = 10$ .

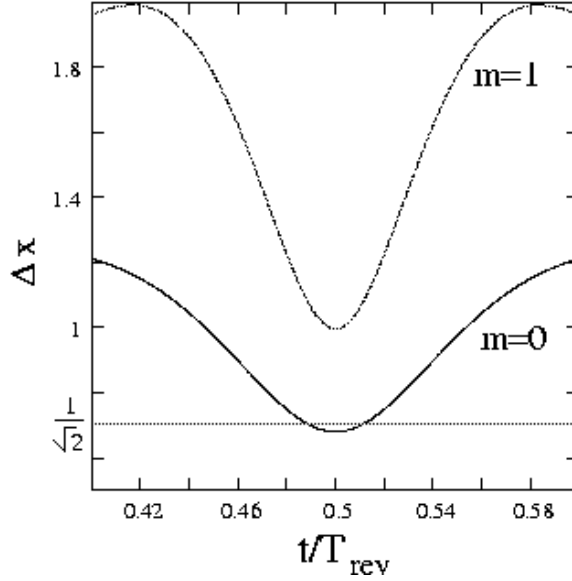


Figure 4.6:  $\Delta x$  versus time in units of  $T_{\text{rev}}$ , in the case  $x_0 = \sqrt{2}$ ,  $p_0 = 0$ .

line demarcates the level below which the state is squeezed. It is evident that squeezing in the rigorous sense accompanies the fractional revival at  $t = \frac{1}{2}T_{\text{rev}}$  when the initial state is a CS. This feature is suppressed when it is a PACS, although  $\Delta x$  does dip down considerably around this fractional revival.

To complete the picture, we have also plotted, in Figs. 4.7 (a) and (b),  $D_q^{(m)}$  versus  $t/T_{\text{rev}}$  for the initial states  $|\alpha, 1\rangle$  and  $|\alpha, 5\rangle$  respectively, for  $\nu = 10$  and  $q = 1, 2, 3$  and 4.

We have focused on  $q^{\text{th}}$ -power amplitude-squeezing at fractional revivals, as this turns out to provide rather more discriminatory signatures of higher-order squeezing effects than the other alternative, namely, Hong-Mandel squeezing. However, a few remarks on the latter are in order here. The relevant variables in the case of Hong-Mandel squeezing are

$$\left[\frac{a + a^\dagger}{\sqrt{2}}\right]^q = x^q \quad \text{and} \quad \left[\frac{a - a^\dagger}{i\sqrt{2}}\right]^q = p^q. \quad (4.17)$$

For  $q = 1$ , of course, Hong-Mandel squeezing is the same as amplitude-squeezing, but the two kinds of squeezing differ for  $q \geq 2$ . Figures 4.8(a) and (b) show how  $\langle(x - \langle x \rangle)^4\rangle \equiv \langle(\delta x)^4\rangle$ , the fourth moment of  $x$  about its mean value, varies over a revival period for an initial CS and PACS, respectively. The horizontal dotted lines

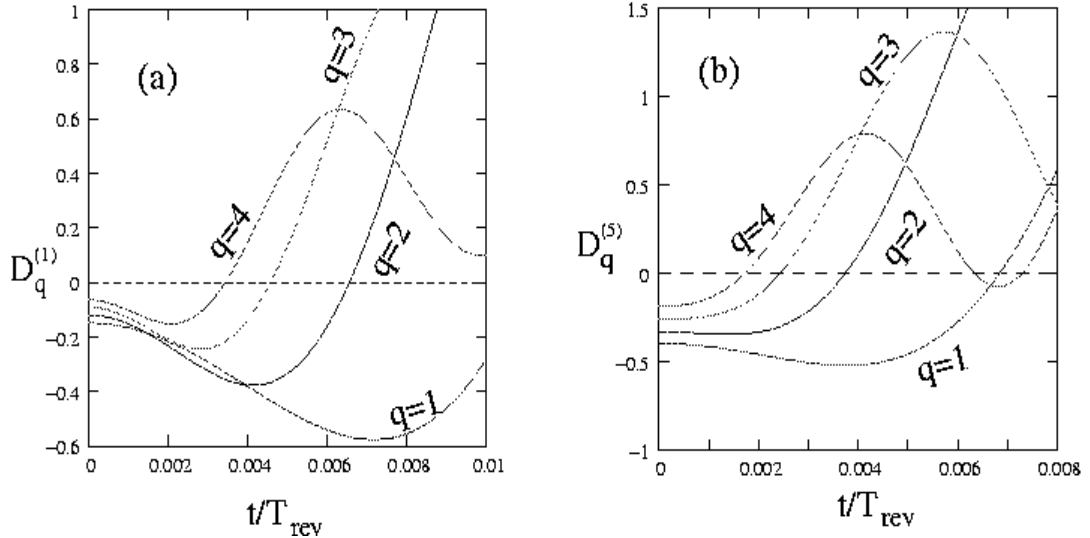


Figure 4.7:  $D_q^{(m)}$  versus  $t/T_{\text{rev}}$  for an initial PACS (a)  $|\alpha, 1\rangle$  and (b)  $|\alpha, 5\rangle$ , with  $\nu = 10$ , for  $q = 1, 2, 3$  and  $4$ .

indicate the bound on  $\langle(\delta x)^4\rangle$ , below which fourth-order Hong-Mandel squeezing occurs in this quadrature. An initial CS exhibits such squeezing near revivals, and comes close to doing so near the fractional revival at  $\frac{1}{2}T_{\text{rev}}$ , but does not actually do so. An initial PACS does not display such higher-order squeezing at any time, although  $\langle(\delta x)^4\rangle$  attains its lowest value at revival times. However, fractional revivals are marked by rapid oscillations of  $\langle(\delta x)^4\rangle$ , these being most pronounced around the 2-sub-packet fractional revival. These features are enhanced further in the case of initial states with larger values of  $m$ .

#### 4.4 The Wigner function and the non-classicality indicator

Finally, we examine the Wigner functions corresponding to the wave packets at instants of fractional revivals, to quantify non-classical behavior during their time evolution. It has been suggested [30] that the “extent” to which the Wigner function becomes negative (as a function of its complex argument) may serve as a measure of the non-classicality of the state concerned. The normalized Wigner function  $W(\beta; t)$  (where  $\beta \in \mathbb{C}$ ) is defined in the case at hand as follows [56]. One

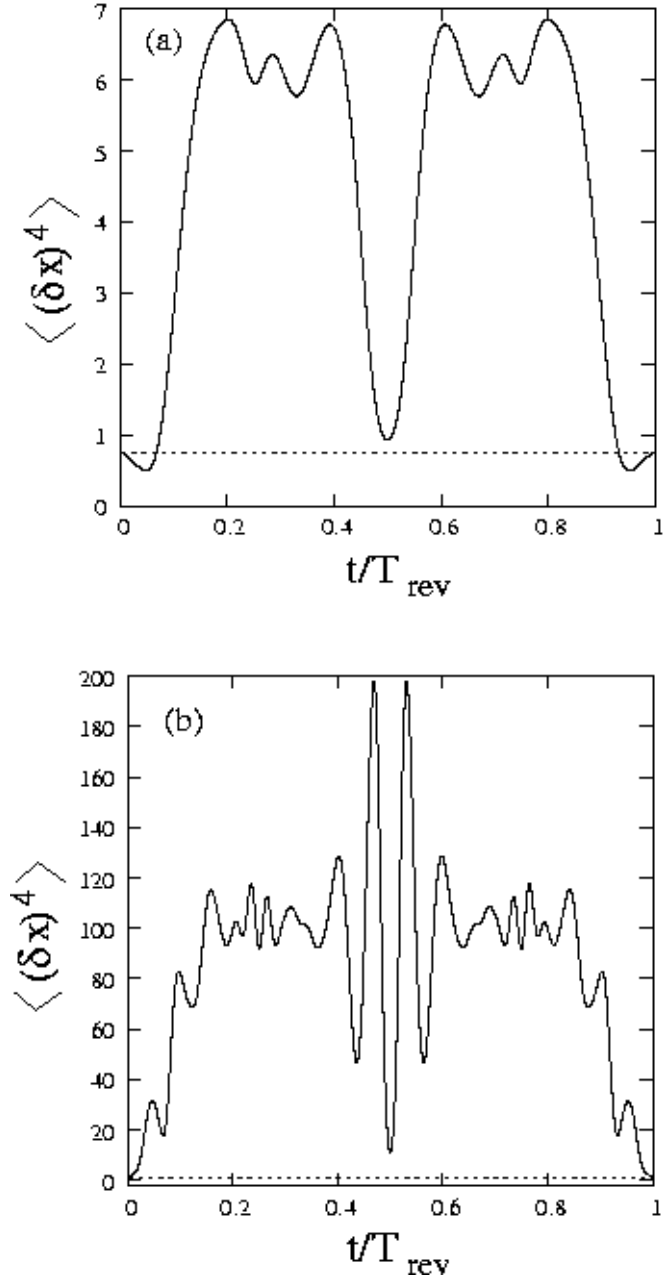


Figure 4.8:  $\langle (\delta x)^4 \rangle$  versus time in units of  $T_{\text{rev}}$  for initial states (a)  $|\alpha\rangle$  and (b)  $|\alpha, 5\rangle$ , with  $\nu = 1$ . Note the very different ordinate scales in the two cases. Hong-Mandel squeezing in  $x$  occurs below the dotted horizontal line.

first defines the symmetric characteristic function

$$K(z, t) = \text{Tr} [\rho(t) e^{z a^\dagger - z^* a}], \quad (4.18)$$

where  $z \in \mathbb{C}$ , and  $\rho(t)$  is the density matrix. Then  $W(\beta; t)$  is the two-dimensional Fourier transform given by

$$W(\beta; t) = \frac{1}{\pi^2} \int d^2 z K(z, t) e^{z a^\dagger - z^* a}. \quad (4.19)$$

Using the representation for the density matrix in the Fock basis, i. e.,

$$\rho(t) = \sum_{l, n=0}^{\infty} \rho_{ln}(t) |l\rangle \langle n|, \quad (4.20)$$

one arrives at the following representation for the Wigner function in terms of the density matrix elements  $\rho_{ln}(t)$  [57]:

$$\begin{aligned} W(\beta; t) = & \frac{2}{\pi} e^{-2|\beta|^2} \text{Re} \left\{ \sum_{l=0}^{\infty} \sum_{n=l}^{\infty} (-1)^l (2 - \delta_{ln}) (l!/n!)^{1/2} \right. \\ & \left. \times (2\beta)^{n-l} \rho_{ln}(t) L_l^{n-l}(4|\beta|^2) \right\}. \end{aligned} \quad (4.21)$$

For an initial coherent state  $|\alpha\rangle$ , we have the standard result

$$\rho_{ln}(0) = \frac{\alpha^{*n} \alpha^l}{\sqrt{l! n!}} e^{-|\alpha|^2}. \quad (4.22)$$

The corresponding Wigner distribution is given by the well-known expression [58]

$$W(\beta; 0) = \frac{2}{\pi} e^{-2|\alpha - \beta|^2}. \quad (4.23)$$

This is positive definite everywhere in the complex  $\beta$ -plane, justifying the appellation “classical” for an oscillator coherent state  $|\alpha\rangle$ . The time-dependent density matrix element in this case is given by

$$\rho_{ln}(t) = \frac{\alpha^{*n} \alpha^l}{\sqrt{l! n!}} e^{-|\alpha|^2} e^{-ix[l(l-1) - n(n-1)]t}. \quad (4.24)$$

Using this in Eq. (4.21), we compute  $W(\beta, t)$  numerically. Figures 4.9(a) and (b) show how the Wigner function for an initial CS behaves at the instants of the 2-sub-packet and 3-sub-packet fractional revivals, respectively.

For the initial photon-added coherent state  $|\alpha, m\rangle$ , one finds

$$\rho_{ln}(0) = \frac{e^{-\nu}}{m! L_m(-\nu)} \frac{\alpha^{l-m} \alpha^{*n-m} \sqrt{l! n!}}{(l-m)! (n-m)!}. \quad (4.25)$$

Correspondingly, the Wigner function at  $t = 0$  can be expressed in the closed form [41, 52]

$$W(\beta; 0) = \frac{2(-1)^m}{\pi L_m(-\nu)} L_m(|2\beta - \alpha|^2) e^{-2|\alpha - \beta|^2}. \quad (4.26)$$

It is to be noted that this is no longer positive definite for all complex  $\beta$ , reflecting the fact that this initial state is no longer “totally” classical, as it departs from perfect coherence due to the photons that have been “added” to  $|\alpha\rangle$  to produce the PACS. The time-dependent density matrix element in this case is given by

$$\rho_{ln}(t) = \frac{e^{-\nu}}{m! L_m(-\nu)} \frac{\alpha^{l-m} \alpha^{*n-m} \sqrt{l! n!}}{(l-m)! (n-m)!} e^{-i\chi [l(l-1) - n(n-1)]t}, \quad (4.27)$$

where  $l, n \geq m$ . (The matrix element  $\rho_{ln}(t)$  vanishes identically for  $l, n < m$ .) Once again, using this in Eq. (4.21), we compute the Wigner function numerically. Figures 4.10(a), (b) and (c) are plots of  $W(\beta; t)$  for the case  $m = 1$  at  $t = 0, \frac{1}{2}T_{\text{rev}}$  and  $\frac{1}{3}T_{\text{rev}}$ , respectively. The corresponding plots for the case  $m = 10$  are shown in Figs. 4.11(a), (b) and (c). With increasing  $m$ , the oscillations of the Wigner function in the  $\beta$ -plane between positive and negative values become more pronounced, and the region of non-classicality becomes more extensive.

To get an idea of the degree of non-classicality as a continuously varying function of time for each of the different initial states we have considered, it is instructive to consider the non-negative quantity  $\delta$  defined as [30]

$$\begin{aligned} \delta(t) &= \int d^2\beta \left( |W(\beta; t)| - W(\beta; t) \right) \\ &= \int d^2\beta |W(\beta_1; t)| - 1. \end{aligned} \quad (4.28)$$



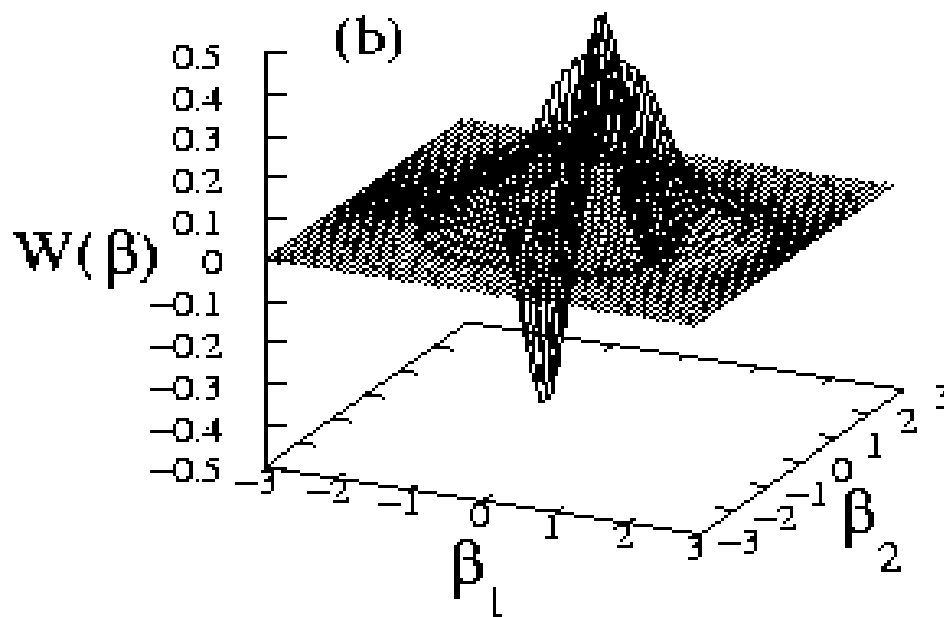
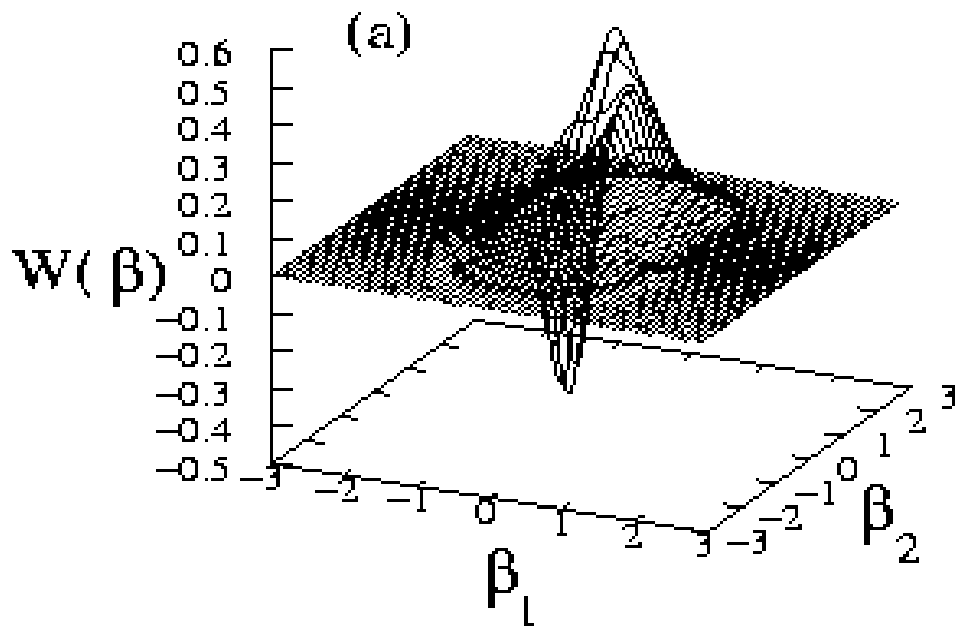


Figure 4.9: Wigner function corresponding to an initial state  $|\alpha\rangle$  with  $\alpha = 1$ , at (a)  $t = \frac{1}{2}T_{\text{rev}}$  and (b)  $t = \frac{1}{3}T_{\text{rev}}$ . Here, and in the succeeding figures,  $\beta_1 = \text{Re } \beta$ ,  $\beta_2 = \text{Im } \beta$ .

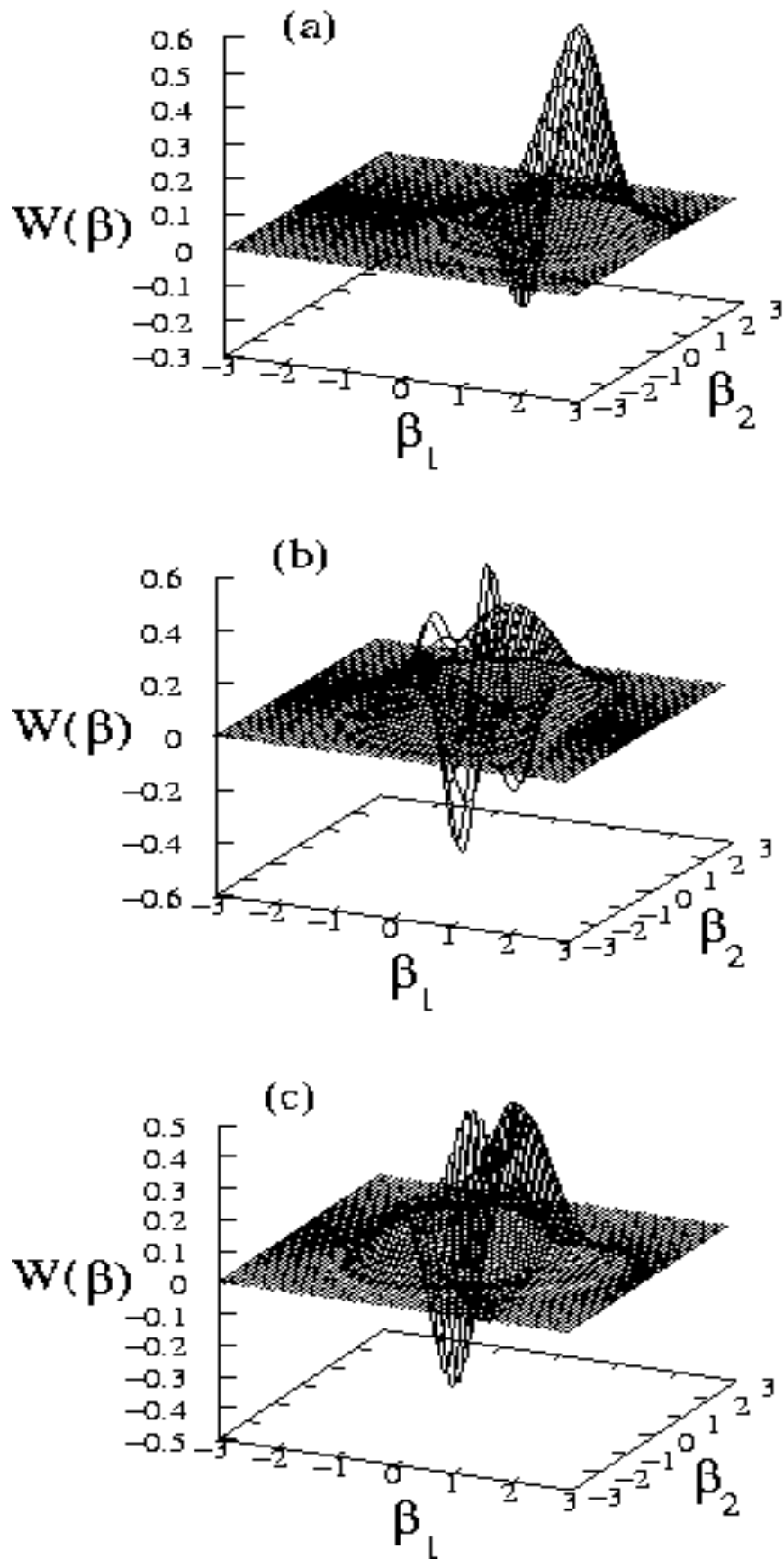


Figure 4.10: Wigner function corresponding to an initial state  $|\alpha, 1\rangle$  with  $\alpha = 1$ , at (a)  $t = 0$ , (b)  $t = \frac{1}{2}T_{\text{rev}}$  and (c)  $t = \frac{1}{3}T_{\text{rev}}$ .

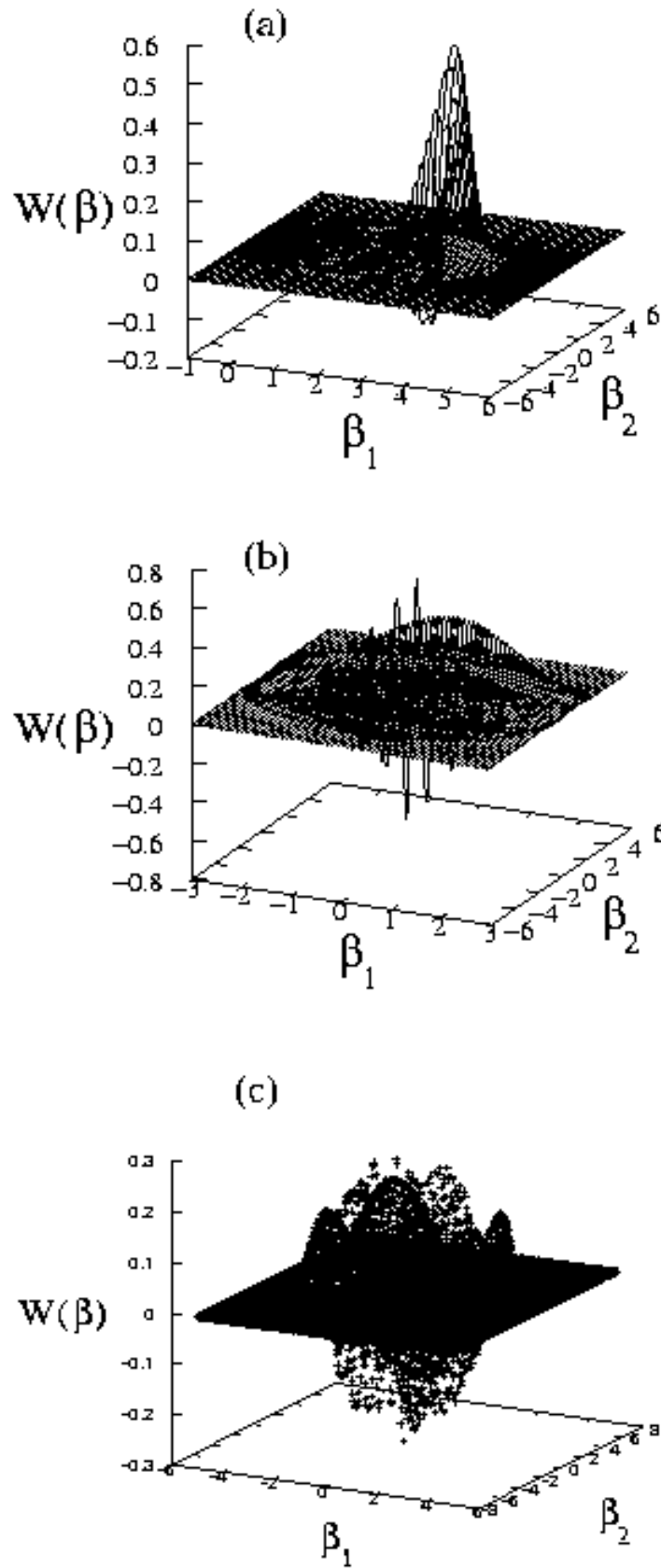


Figure 4.11: Wigner function corresponding to an initial state  $|\alpha, 10\rangle$  with  $\alpha = 1$ , at (a)  $t = 0$ , (b)  $t = \frac{1}{2}T_{\text{rev}}$  and (c)  $t = \frac{1}{3}T_{\text{rev}}$ .

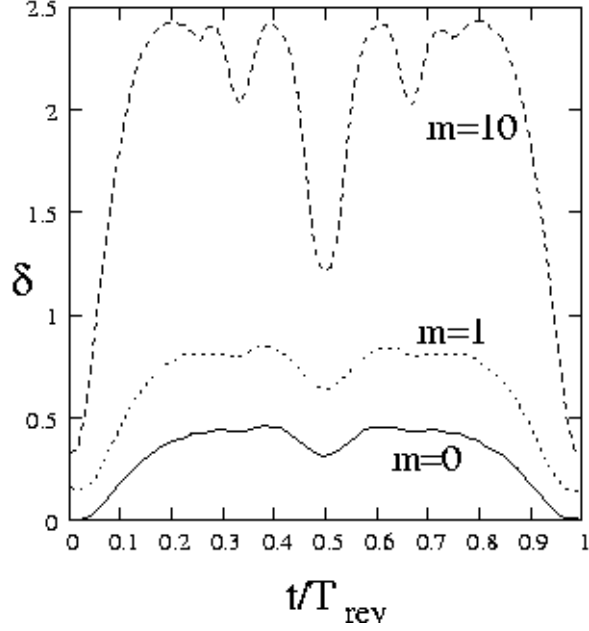


Figure 4.12: Non-classicality indicator  $\delta$  versus time in units of  $T_{\text{rev}}$ , for initial states  $|\alpha, m\rangle$  with  $\alpha = 1$ .

The larger the value of  $\delta$ , the greater is the extent of non-classicality of the state concerned, although of course  $\delta$  alone does not give a complete picture of the oscillations of the Wigner function. In Fig. 4.12 we have plotted  $\delta$  versus  $t$  for initial states  $|\alpha\rangle$ ,  $|\alpha, 1\rangle$ , and  $|\alpha, 10\rangle$  with  $\alpha = 1$ . It is clear that in the interval between  $t = 0$  and  $t = T_{\text{rev}}$ ,  $\delta$  has the most pronounced local minimum at the 2-sub-packet fractional revival, followed by the local minima at the 3-sub-packet and 4-sub-packet fractional revivals. This feature becomes increasingly prominent for larger values of  $m$ , showing that the extent of non-classicality also increases with  $m$ , as expected.

## 4.5 Concluding remarks

We have shown that the crucial difference between an initial CS and an initial PACS propagating through a Kerr-like medium arises at the instant  $\frac{1}{2}T_{\text{rev}}$ , when the former displays squeezing and the latter does not. A possible experimental set-up to examine the squeezing properties of the state at  $\frac{1}{2}T_{\text{rev}}$  involves passing it through a Kerr medium with a known value of  $\chi$  (the third-order nonlinear sus-

ceptibility), and therefore  $T_{\text{rev}}$ , and using the time evolved state at  $\frac{1}{2}T_{\text{rev}}$  as the input field. Superimposing this on the field from a local oscillator, and performing balanced homodyne detection to measure the variance in  $x$ , would determine the extent of squeezing. Thus, the successful experimental generation of non-classical states of light together with the observation of higher-order moments [59] of appropriate quadrature variables would enable the probing of the rich structure of wave packet dynamics in a nonlinear medium.

# CHAPTER 5

## Ergodicity properties of entangled two-mode states - I

### 5.1 Introduction

In the preceding chapters, we have examined the manner in which signatures of revivals and different fractional revivals of a wave packet manifest themselves in the dynamics of the expectation values of appropriate operators. We have shown that, by tracking the time evolution of various moments of certain operators, selective identification of different fractional revivals can be achieved [18]. Again, since the precise nature of the initial state concerned plays a crucial role in determining its subsequent dynamics and the non-classical features it exhibits, these signatures help assess the extent of coherence of the initial state [28]. Further, it has been shown that the squeezing and higher-order squeezing properties of certain quadrature variables in the neighborhood of a two sub-packet fractional revival of the wave packet provide quantifiable measures of the degree of departure from coherence of the initial state [29].

In this chapter, we extend these investigations to the dynamics of entangled states. To be specific, we consider a physically relevant generalization of the example considered earlier, and now study the dynamics of a single-mode electromagnetic field interacting with the atoms of a nonlinear medium [34], taking into account the interaction between the field mode and the medium. Although we consider initial states that are direct product states of the field and atom modes, entanglement of these two modes sets in during temporal evolution. However, we have shown that for certain ranges of values of the parameters and coupling constants in the governing Hamiltonian, the modes disentangle at specific instants during the evolution, and the state of the system returns to its initial form, apart

from an overall phase. This feature is clearly the analog of wave packet revivals in the dynamics of a single mode. The entropy of entanglement of the system provides a measure of the extent of revival of the original state. At the instants of revivals (these being integer multiples of a revival time which we refer to as  $T_{\text{rev}}$  in this two-mode example as well), this entropy vanishes.

It is evident that, as in the single-mode case, the dynamics of the quantum state between  $t = 0$  and  $t = T_{\text{rev}}$  would lead to closed orbits in a classical phase space in which quantum mechanical expectation values are regarded as the dynamical variables. The entropy of entanglement is also seen to reduce significantly in certain cases at fractions  $\frac{1}{2}$ ,  $\frac{1}{3}$ ,  $\frac{2}{3}$  and  $\frac{1}{4}$  of  $T_{\text{rev}}$ , signaling the appearance of the counterparts of fractional revivals at these instants. We identify suitable operators whose expectation values carry clear signatures of this phenomenon.

We have also investigated the role of the (non-entangled) initial state, and the extent of departure of the initial field mode from coherence, on the subsequent revival properties of the state. In particular, the link between entanglement of states and their squeezing properties [60] has been examined. The entropy of entanglement at any instant increases with increasing departure from coherence of the initial field mode, and revivals do not occur. This aspect is studied by means of a time-series analysis of the expectation value of a certain observable. The details of this analysis and the results obtained are presented in the next chapter.

In the next section, we describe the model [34] we use to study the dynamics of two-mode entanglement. Earlier results on the collapse and revival phenomena in this case, and their dependence on the initial state and parameter values, are summarized. In Section 5.3, we show how the extent to which a state revives at any instant is related to the instantaneous sub-system von Neumann entropy (SVNE) and the sub-system linear entropy (SLE). Certain operators whose expectation values carry signatures of the different fractional revivals are also identified. We have examined the dynamics of several initial states, taking the oscillator representing an atom of the medium to be in the ground state while the field is, respectively, in a Fock state, a CS, and a PACS. This enables us to analyze systematically the

effects of different initial field modes on the dynamics. The relationship between the squeezing exhibited by the state of the system and the initial field mode is also brought out. We conclude the chapter with some brief comments.

## 5.2 Single-mode field in a nonlinear medium:

### The model

Sanz *et al.* [33] have examined the non-classical effects that arise in the dynamics of two entangled modes governed by a nonlinear Hamiltonian, in the framework of an exactly solvable case: two modes of an electromagnetic field interacting in a Kerr-like medium. Taking the initial state to be a direct product, either of two Fock states or of two coherent states, the periodic exact revival of these states has been established, and the manner in which these properties show up in the collapse and revival phenomena displayed by the expectation values of observables has been investigated. The collapses are marked by expectation values remaining constant over a certain interval, while the revivals are signaled by rapid pulsed variations of these quantities. This is clearly analogous to the signatures of revivals displayed in the single-mode case that we have discussed in the preceding chapters.

As stated in Chapter 1, our objective is to investigate the full range of regular and irregular dynamical behavior exhibited by quantum mechanical expectation values. For this purpose, we require a system where revivals, near revivals, as well as no revivals of the initial state can all occur, for different parameter values. As already mentioned, a good candidate Hamiltonian for our purposes is the one that describes the interaction of a single-mode field of frequency  $\omega$  with the atoms of the nonlinear medium through which it propagates. The medium is modeled [34] by an anharmonic oscillator with frequency  $\omega_0$  and anharmonicity parameter  $\gamma$ . The Hamiltonian of the total system is given by

$$H = \omega a^\dagger a + \omega_0 b^\dagger b + \gamma b^{\dagger 2} b^2 + g(a^\dagger b + b^\dagger a). \quad (5.1)$$

$a$  and  $a^\dagger$  are the annihilation and creation operators pertaining to the field, while



$b$  and  $b^\dagger$  are the corresponding atomic oscillator operators. The coupling constant  $g$  is a measure of the strength of the coupling between the field modes and the atom modes. The Fock basis is given by  $\{|n\rangle_a \otimes |n'\rangle_b\}$ , where  $n$  and  $n'$  are the eigenvalues of  $a^\dagger a$  and  $b^\dagger b$ , respectively. The photon number operator  $\mathbf{N} = a^\dagger a$  no longer commutes with  $H$ . However, the *total* number operator  $\mathbf{N}_{\text{tot}} = a^\dagger a + b^\dagger b$  *does* commute with  $H$ . Hence we may write the basis states as  $|N - n\rangle_a \otimes |n\rangle_b$ , using  $N$  to label the eigenvalue of  $\mathbf{N}_{\text{tot}}$ . (We remark that, in the discussion of the one-mode case in the preceding chapters, we have used  $N$  in places to denote the eigenvalue of the photon number operator  $\mathbf{N}$ . No confusion should arise as a result, as we specify the notation explicitly wherever required.) For notational simplicity, let us write

$$|N - n\rangle_a \otimes |n\rangle_b \equiv |N - n; n\rangle. \quad (5.2)$$

It is evident that  $\langle N - n; n | H | N' - n'; n' \rangle = 0$ , if  $N \neq N'$ . Hence, for each given value of  $N$ , the Hamiltonian  $H$  can be diagonalized in the space of the states  $|N - n; n\rangle$ , where  $n = 0, 1, \dots, N$ . Let the eigenvalues and eigenstates of  $H$  be  $\lambda_{N_s}$  and  $|\psi_{N_s}\rangle$ , respectively, where  $s = 0, 1, \dots, N$  for a given  $N$ , and  $N = 0, 1, \dots$  *ad inf*. It is convenient to expand  $|\psi_{N_s}\rangle$  in the basis  $\{|N - n; n\rangle\}$  as

$$|\psi_{N_s}\rangle = \sum_{n=0}^N d_n^{N_s} |N - n; n\rangle, \quad (5.3)$$

so that  $d_n^{N_s} = \langle N - n; n | \psi_{N_s} \rangle$ .

The time-dependent density operator  $\rho(t)$  corresponding to different choices of the initial state  $|\psi(0)\rangle$  can now be obtained. For instance, in the simple case in which  $|\psi(0)\rangle = |N\rangle_a \otimes |0\rangle_b \equiv |N; 0\rangle$ , we have

$$\begin{aligned} \rho(t) &= \sum_{s=0}^N \sum_{s'=0}^N \exp[-i(\lambda_{N_s} - \lambda_{N_{s'}})t] \langle \psi_{N_s} | N; 0 \rangle \\ &\times \langle N; 0 | \psi_{N_{s'}} \rangle |\psi_{N_s}\rangle \langle \psi_{N_{s'}}|. \end{aligned} \quad (5.4)$$

Such expressions for the time-dependent density matrix and the corresponding reduced density matrices for the two sub-systems (i. e., the field and the medium,

respectively) are required in order to evaluate the expectation values and entropies to be considered in the next section. Further details are given in Appendix D.

We now summarize some of the key results of Ref. [34] pertaining to the collapse and revival phenomena exhibited by the field, as these are of relevance to our study. When  $g = 0$ , the Hamiltonian in Eq. (5.1) is in diagonal form as it stands. If  $\gamma = 0$ ,  $H$  is exactly diagonalizable, and there is periodic exchange of energy between the field and the atomic oscillator. For non-zero values of the ratio  $\gamma/g$  of the respective strengths of the nonlinearity and the field-atom interaction, collapses and revivals could occur over certain intervals of time, in between these periodic exchanges of energy. This phenomenon translates into the behavior of expectation values of certain observables as well. For instance, during a collapse of the energy exchange over an interval of time, the mean photon number  $\langle a^\dagger a \rangle$  essentially remains constant. A revival of the energy exchange is signaled by rapid oscillations of the mean photon number about this steady value, over the relevant time interval.

Further, when the atomic oscillator is initially in its ground state, while the field starts either in a Fock state or in a coherent state, one finds the the following results: (a) For weak nonlinearity ( $\gamma/g \ll 1$ ), collapses and revivals of the mean photon number occur almost periodically in time, for both kinds of initial field states. The revival time can be shown to be *approximately* equal to  $2\pi/\gamma$  in the former case, and  $4\pi/\gamma$  in the latter. (b) For  $\gamma/g \sim 1$ , such collapses and revivals occur more irregularly if the field is initially in a coherent state, compared to the case when it is initially in a Fock state. (c) For large nonlinearity ( $\gamma/g \gg 1$ ), these collapses and revivals do not occur. Bearing these results in mind, in the next section we examine the manner in which the foregoing collapse and revival phenomena are mirrored in the entropy of entanglement of the system. We identify observables which carry signatures of these collapses and revivals, and discuss the influence of the departure from coherence of the initial state of the field on the extent to which it revives subsequently.

### 5.3 Entanglement properties

Let us now examine the detailed dynamics of three different classes of initial states which are direct products of the field and atom states, evolving under the Hamiltonian in Eq. (5.1). As stated earlier, the initial state of the atom is taken to be the oscillator ground state  $|0\rangle_b$ , while that of the field is, respectively, (a) a Fock state  $|n\rangle_a$ ,  $n = 0, 1, \dots$ ; (b) a CS  $|\alpha\rangle_a$ ; and (c) an  $m$ -photon-added CS  $|\alpha, m\rangle_a$ ,  $m = 1, 2, \dots$ . (Recall that the suffixes  $a$  and  $b$  correspond to the electromagnetic field and the atoms of the medium, respectively.) Extending the notation in Eq. (5.2), we shall write

$$|\alpha, m\rangle_a \otimes |n\rangle_b \equiv |(\alpha, m); n\rangle \quad (5.5)$$

for the direct product state concerned.

As we are dealing with a pure bipartite system, it is natural to consider the time-dependences of  $S_k$ , the sub-system von Neumann entropy (SVNE), and  $\delta_k$ , the sub-system linear entropy (SLE), where the suffix  $k$  stands for either  $a$  or  $b$ , depending on the sub-system considered. These quantities are defined as

$$S_k(t) = -\text{Tr}_k(\rho_k(t) \ln \rho_k(t)) \quad (5.6)$$

and

$$\delta_k(t) = 1 - \text{Tr}_k(\rho_k^2(t)), \quad (5.7)$$

where  $\rho_k(t)$  is the time-dependent reduced density operator for the sub-system concerned. In terms of the set of eigenvalues of  $\rho_k(t)$ , we have

$$S_k(t) = -\sum_i \lambda_k^{(i)}(t) \ln \lambda_k^{(i)}(t), \quad \delta_k(t) = 1 - \sum_i [\lambda_k^{(i)}(t)]^2, \quad (5.8)$$

where the summation runs over all the eigenvalues  $\lambda_k^{(i)}(t)$ . Once again, as we have a pure bipartite system, the SVNEs for the two sub-systems are in fact equal to each other at all times, as are the SLEs. (This used as one of the checks on the numerical routines employed.) In Appendix D, we have outlined the steps leading

to the derivation of the matrix elements of the reduced density matrices  $\rho_a(t)$  and  $\rho_b(t)$ , required for the numerical computation of  $S_k(t)$  and  $\delta_k(t)$ .

We are interested, in this chapter, in examining revival phenomena. We therefore restrict ourselves to the case of weak nonlinearity, i. e.,  $\gamma/g \ll 1$ , as this is the situation in which these phenomena occur. For illustrative purposes, we set the values of the parameters at  $\omega = \omega_0 = 1$ , and  $\gamma = 1$ ,  $g = 100$ , so that  $\gamma/g = 10^{-2}$ , in all the numerical results reported in the rest this section. Note that the revival time then corresponds to  $gt \approx 200\pi$  for an initial Fock state of the field, and  $gt \approx 400\pi$  for an initial coherent state of the field.

Figures 5.1 (a) and (b) depict plots of the SVNE and the SLE versus  $gt$  for respective initial states  $|10; 0\rangle$  and  $|\alpha\rangle_a \otimes |0\rangle_b \equiv |\alpha; 0\rangle$  with the parameter value  $\nu = 1$ . The band-like appearance of the plots in Fig. 5.1 (a) arises from the extremely rapid oscillations of the ordinates. The corresponding plots for an initial state  $|\alpha, 5\rangle_a \otimes |0\rangle_b \equiv |(\alpha, 5); 0\rangle$  in the cases  $\nu = 1$  and  $\nu = 5$  are shown in Figs. 5.2 (a) and (b) respectively. In all the cases above, the SVNE (the upper plot in each figure) is larger than the SLE (the lower plot in each figure) at any instant of time. It is evident that both SVNE and SLE display roughly similar oscillatory behavior in time. However, certain striking differences arise in the time evolution of the SVNE and SLE, depending on the actual initial state considered. If the field is initially in a Fock state or a CS, the entropies return to zero at regular intervals of time (see Fig. 5.1), signaling a revival of the initial state. (Note that the revival times are indeed approximately equal to  $2\pi$  and  $4\pi$ , respectively, recalling that we have set  $\gamma = 1$  and  $g = 100$ .) In contrast, if the initial state of the field is a PACS, the entropies do not exhibit such exact revivals, although they do show substantial oscillatory behavior near  $T_{\text{rev}}$ . Further, with an increase in the value of  $\nu$ , the oscillations in the SVNE and SLE die down. This effect is enhanced for larger values of  $m$ , as seen in the rapid increase and saturation of both the SVNE and SLE for an initial state  $|(\alpha, 5); 0\rangle$  for  $\nu = 5$ , in contrast to the corresponding plots for  $\nu = 1$ : see Figs. 5.2 (a) and (b).

It is also clear that the SVNE and SLE display marked oscillatory behavior near  $\frac{1}{2}T_{\text{rev}}$ ,  $\frac{1}{3}T_{\text{rev}}$  and  $\frac{1}{4}T_{\text{rev}}$ . This behavior may be regarded as the counterpart,

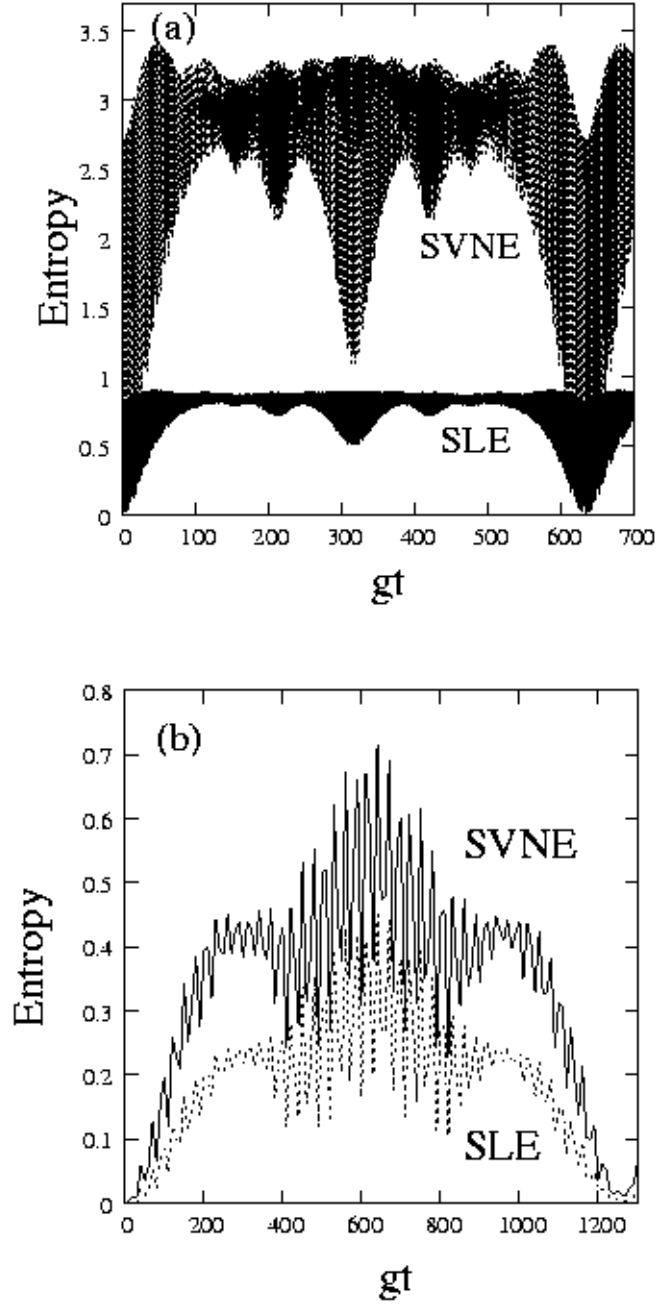


Figure 5.1: SVNE and SLE versus  $gt$  for (a) an initial Fock state  $|10; 0\rangle$ , and (b) an initial coherent state  $|\alpha; 0\rangle$  with  $\nu = 1$ . The ratio  $\gamma/g = 10^{-2}$  in Figs. 5.1 through 5.11.

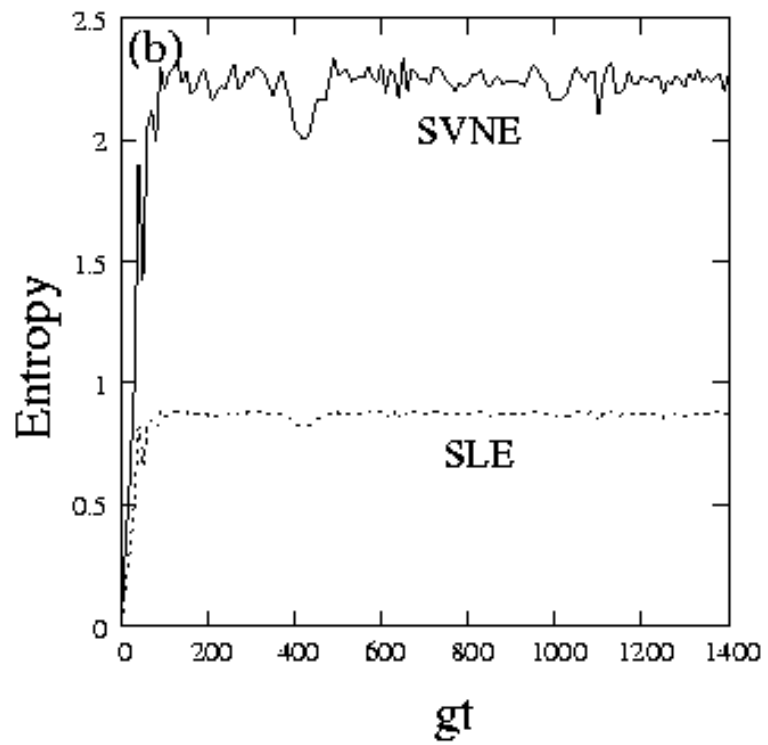
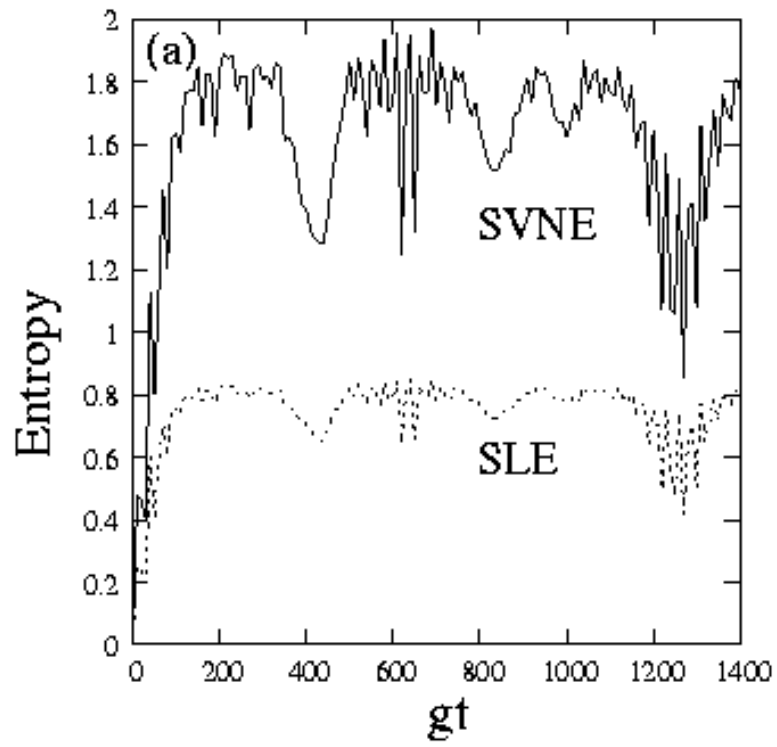


Figure 5.2: SVNE and SLE versus  $gt$  for an initial state  $|(\alpha, 5); 0\rangle$  for (a)  $\nu = 1$  and (b)  $\nu = 5$ .

in the coupled system, of the fractional revivals seen in the single-mode case (as described in Chapters 2 and 3). Again, these oscillations die down in amplitude with increasing  $m$  when the initial state of the field is a PACS, and are most pronounced if the field is initially in a Fock state.

We now examine whether signatures of the features seen above appear in the time evolution of expectation values of observables. For this purpose, we define the quadratures

$$\xi = (x_a + x_b)/2, \quad \eta = (p_a + p_b)/2, \quad (5.9)$$

where

$$x_a = (a + a^\dagger)/\sqrt{2}, \quad x_b = (b + b^\dagger)/\sqrt{2} \quad (5.10)$$

and

$$p_a = (a - a^\dagger)/(i\sqrt{2}), \quad p_b = (b - b^\dagger)/(i\sqrt{2}). \quad (5.11)$$

If the field is initially in a Fock state, both  $\langle \xi \rangle$  and  $\langle \eta \rangle$  vanish identically at all times. Setting  $\omega = \omega_0 = 1$ ,  $\gamma = 1$  and  $g = 100$  as before (for ready comparison with the behavior of the SVNE and SLE discussed above), we have plotted  $\langle \xi \rangle$  versus  $gt$  for an initial state  $|\alpha; 0\rangle$  with  $\nu = 1$  and 5, respectively, in Figs. 5.3 (a) and (b). Figure 5.3 (a) shows that  $\langle \xi \rangle$  displays rapid pulsed oscillations near  $t = 4\pi$ , similar to its behavior near  $t = 0$ . This mark of a revival is consistent with the behavior of the SVNE and SLE in this case, *cf.* Fig. 5.1 (b). The collapses are not sharp, in the sense that  $\langle \xi \rangle$  is not constant over the time interval between successive revivals — oscillatory bursts occur in between, with a slight enhancement of these oscillations around the fractional revival at  $\frac{1}{2}T_{\text{rev}}$ . In contrast, the collapses in between revivals are much more complete for larger values of  $\nu$ , as seen in Fig. 5.3 (b), consistent with the corresponding behavior of the SVNE and SLE in this case.

An interesting feature is that these collapses become much sharper for even a marginal departure from coherence of the initial state of the field.  $\langle \xi \rangle$  remains virtually constant over the duration of the collapse, and then bursts into rapid oscillations close to revivals, as seen in Fig. 5.4 which corresponds to  $m = 1$  and  $\nu = 1$ . As in the case of single-mode dynamics, the amplitude of the oscil-

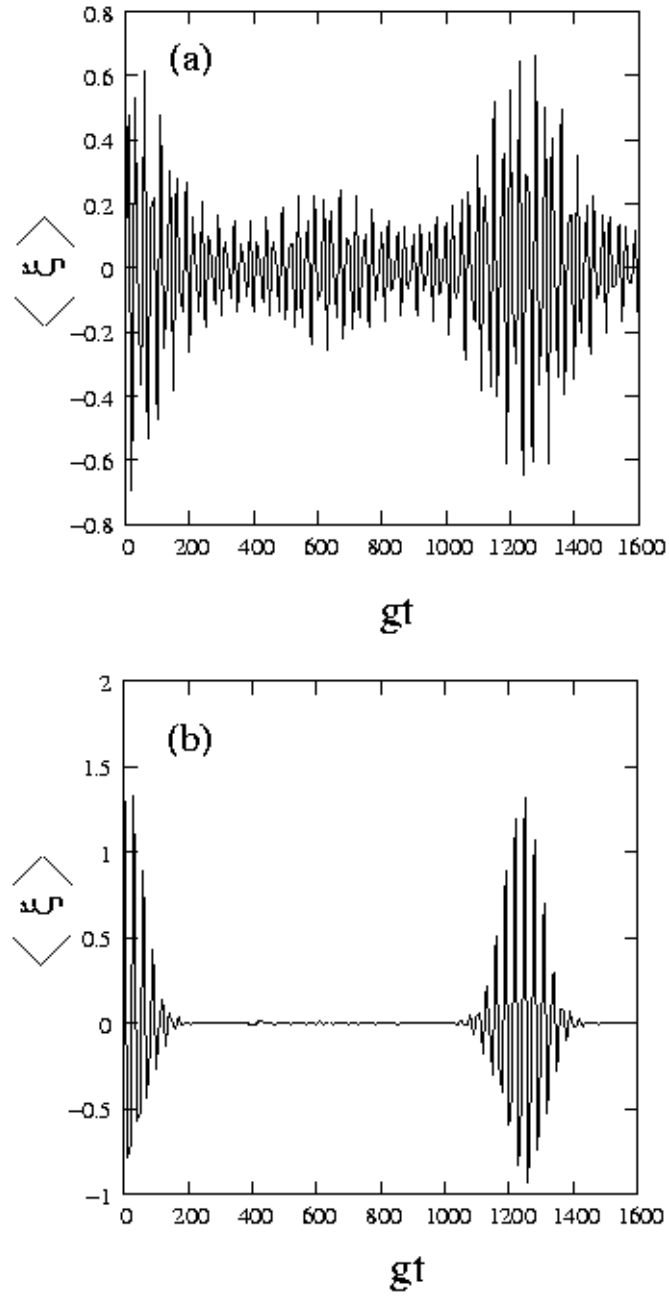


Figure 5.3:  $\langle \xi \rangle$  versus  $gt$  for an initial state  $|\alpha; 0\rangle$  with (a)  $\nu = 1$  and (b)  $\nu = 5$ , respectively.



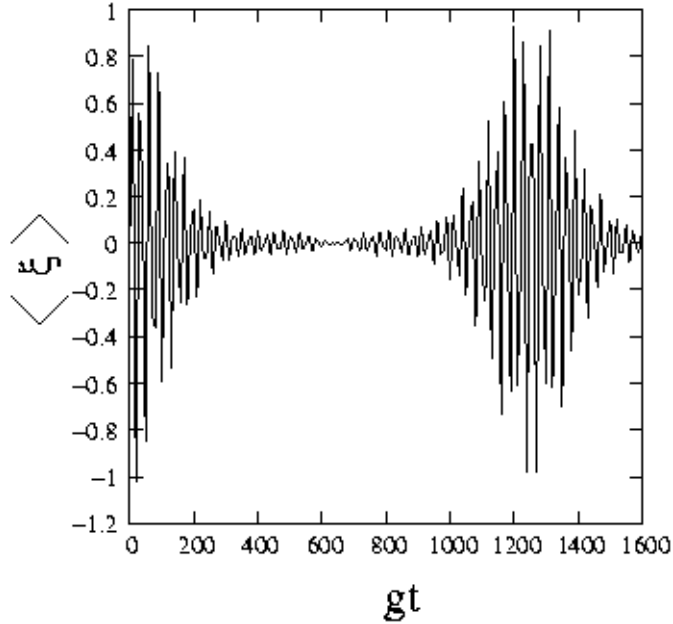


Figure 5.4:  $\langle \xi \rangle$  versus  $gt$  for an initial state  $|(\alpha, 1); 0\rangle$  with  $\nu = 1$ .

lations in the neighborhood of  $T_{\text{rev}}$  decreases significantly with an increase in  $m$ . Thus, for small values of  $\nu$ , it is easy to distinguish between an initial CS and an initial PACS. The expectation value of  $\eta$  also displays these signatures. While the sub-system variables  $x_a$ ,  $x_b$ ,  $p_a$  and  $p_b$  do exhibit revivals in their expectation values, their higher moments do not capture the occurrence of fractional revivals. However, the higher moments of the combinations  $\xi$  and  $\eta$  *do* carry distinguishing signatures to selectively pin-point the analogs of the different fractional revivals that occur in the single-mode case. Hence  $\xi$  and  $\eta$  are the appropriate dynamical variables for the interacting system under consideration.

The standard deviation  $\Delta\xi$  of  $\xi$  reflects the occurrence of the dips in the plots of the SVNE and SLE at  $\frac{1}{2}T_{\text{rev}}$ . Consider, first, the case when the initial state is of the form  $|N; 0\rangle$ . Then a plot of  $\Delta\xi$  versus  $gt$  shows a burst of rapid oscillations at  $t \approx \pi$  ( $\approx \frac{1}{2}T_{\text{rev}}$ ). Fig. 5.5 illustrates this for  $N = 10$ . (Note that the case  $N = 1$  is exceptional in this regard, since  $\Delta\xi$  reduces to a constant in this instance.) This feature holds for an initial CS or PACS as well, as is evident (see Fig. 5.6) from the sudden burst of oscillations in  $\Delta\xi$  around  $t \approx 2\pi \approx \frac{1}{2}T_{\text{rev}}$  for initial states  $|\alpha; 0\rangle$ ,  $|(\alpha, 1); 0\rangle$  and  $|(\alpha, 5); 0\rangle$  (recall that  $T_{\text{rev}} \approx 4\pi$  in this case).

We note that *squeezing* occurs in the neighborhood of  $\frac{1}{2}T_{\text{rev}}$  when the initial

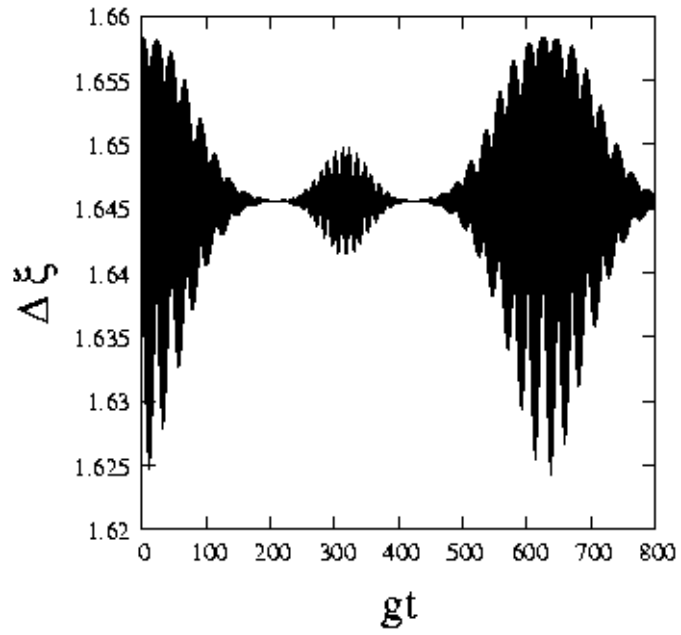


Figure 5.5:  $\Delta\xi$  versus  $gt$  for an initial state  $|10; 0\rangle$ .

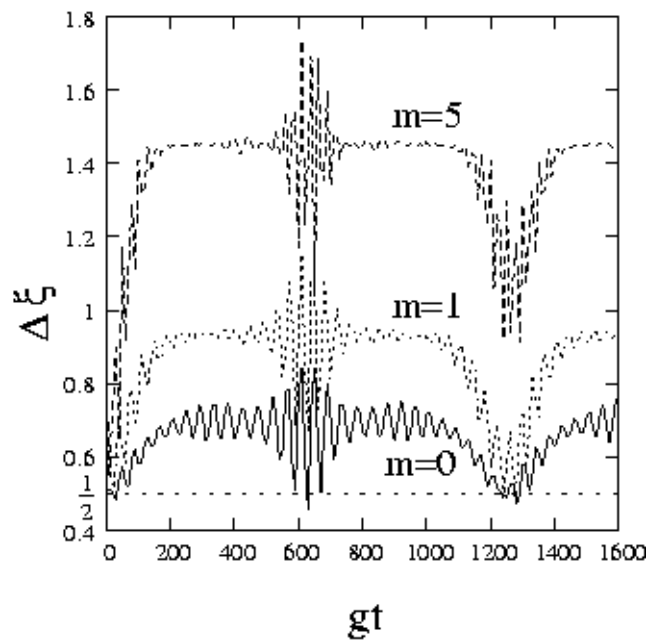


Figure 5.6:  $\Delta\xi$  versus  $gt$  for an initial state  $|(\alpha, m); 0\rangle$  with  $\nu = 1$  and  $m = 0, 1$  and  $5$ , respectively.

state of the field is a coherent state:  $\Delta\xi$  drops below the value  $\frac{1}{2}$  (the horizontal dotted line in Fig. 5.6) in the case when the initial state is  $|\alpha; 0\rangle$ , in contrast to what happens for an initial PACS  $|(\alpha, m); 0\rangle$ . While this is similar to the squeezing property seen in the single-mode case, such parallels do not hold in the case of higher-order squeezing. The relevant quadrature variables in this case (analogous to those in Eq.(4.7)) are

$$Z_1 = \frac{(a^q + a^{\dagger q} + b^q + b^{\dagger q})}{2\sqrt{2}}, \quad Z_2 = \frac{(a^q - a^{\dagger q} + b^q - b^{\dagger q})}{2i\sqrt{2}}. \quad (5.12)$$

For  $q = 1$ ,  $Z_1$  and  $Z_2$  reduce to  $\xi$  and  $\eta$ , respectively. The indicator of higher-order squeezing is defined, analogous to  $D_q(t)$  in Eq. (4.11) of Chapter 4, as

$$D_q(t) = \frac{(\Delta Z_1)^2 - \frac{1}{2}|\langle[Z_1, Z_2]\rangle|}{\frac{1}{2}|\langle[Z_1, Z_2]\rangle|}, \quad (5.13)$$

where  $\Delta Z_1$  denotes the standard deviation in the variable  $Z_1$  defined in Eq. (5.12). We note that  $[Z_1, Z_2]$  is no longer a polynomial function of the (total) number operator  $\mathbf{N}_{\text{tot}}$  alone. Extending the notation used in Chapter 4, we shall write  $D_q^{(m)}$  for  $D_q$  in the case of an initial state  $|(\alpha, m); 0\rangle$ , and  $D_q^{(N)}$  to denote  $D_q$  for an initial state  $|N; 0\rangle$ . In contrast to the single-mode case, even for weak nonlinearity ( $\gamma/g = 10^{-2}$ ) and  $\nu = 1$ , amplitude-squared squeezing ( $q = 2$ ) is absent at  $t = \frac{1}{2}T_{\text{rev}}$  whether the field is in a Fock state, or a CS, or a PACS. For  $N = 10$ , and an initial state  $|10; 0\rangle$ , we have plotted  $D_2^{(N)}$  versus time in Fig. 5.7. The state is never squeezed, as  $D_2^{(N)}$  is always positive. Similar plots for an initial state  $|\alpha; 0\rangle$  and  $|(\alpha, 1); 0\rangle$  are given in Fig. 5.8. While  $D_2^{(0)}$  is almost zero at certain instants for a coherent initial field state  $|\alpha\rangle_a$ , it is clear that it does not drop below the horizontal line indicating the value below which amplitude-squared squeezing occurs.

Turning to the higher moments of  $\xi$  and  $\eta$ , we note that all the odd moments of  $\xi$  vanish identically for all  $t$  if the initial state is a direct product of Fock states (see Appendix D). Analogous to the single-mode case, for small values of  $\nu$ , the higher moments of  $\xi$  show distinct signatures at fractional revivals only if  $m$  is sufficiently large. This is evident from Fig. 5.9, where we have plotted  $\langle(\xi - \langle\xi\rangle)^3\rangle \equiv \langle(\delta\xi)^3\rangle$

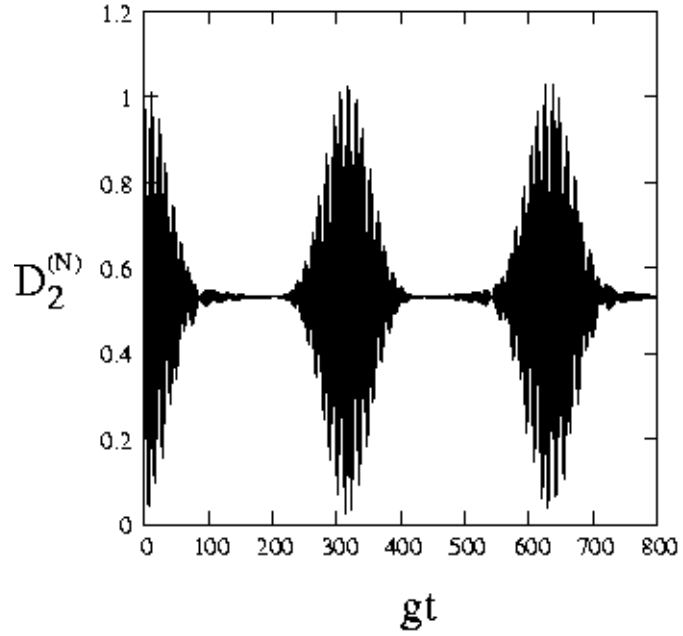


Figure 5.7:  $D_2^{(N)}$  versus  $gt$  for an initial state  $|N; 0\rangle$  with  $N = 10$ .

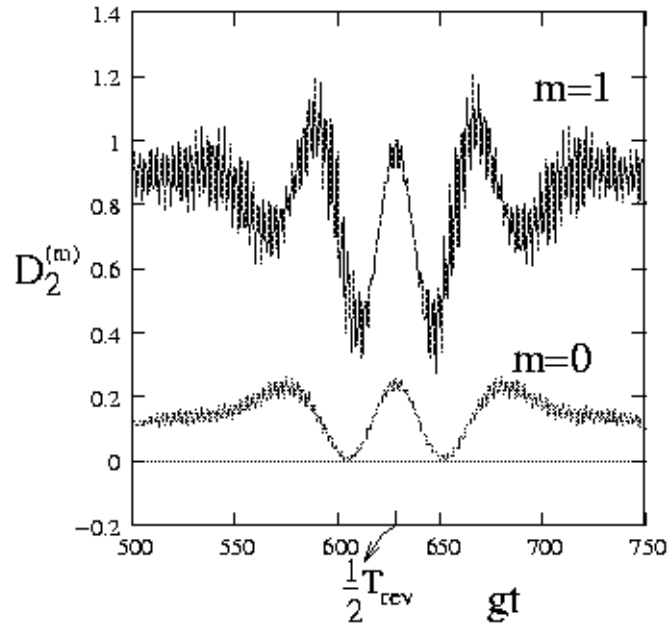


Figure 5.8:  $D_2^{(m)}$  versus  $gt$  for an initial state  $|\alpha; 0\rangle$  and  $|(\alpha, 1); 0\rangle$  with  $\nu = 1$ .

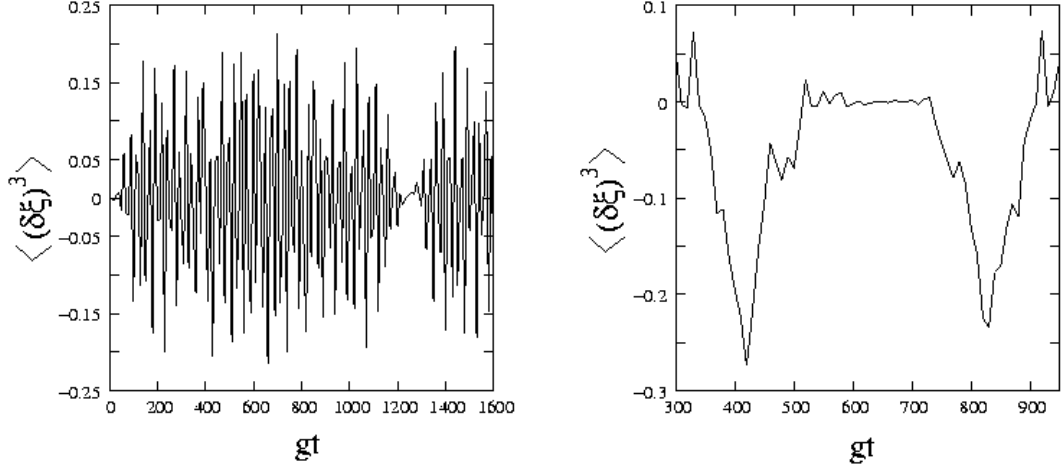


Figure 5.9:  $\langle (\delta\xi)^3 \rangle$  versus  $gt$  for an initial state (a)  $|\alpha; 0\rangle$  (b)  $|(\alpha, 3); 0\rangle$  with  $\nu = 1$  and  $\gamma/g = 10^{-2}$ .

versus time for initial states  $|\alpha; 0\rangle$  and  $|(\alpha, 3); 0\rangle$ , respectively, with  $\nu = 1$  and  $\gamma/g = 10^{-2}$ . In the latter case, the signatures are manifested in the pronounced dips in  $\langle (\delta\xi)^3 \rangle$  at  $\frac{1}{3}T_{\text{rev}}$  and  $\frac{2}{3}T_{\text{rev}}$ . However, for larger values of  $\nu$ , such signatures

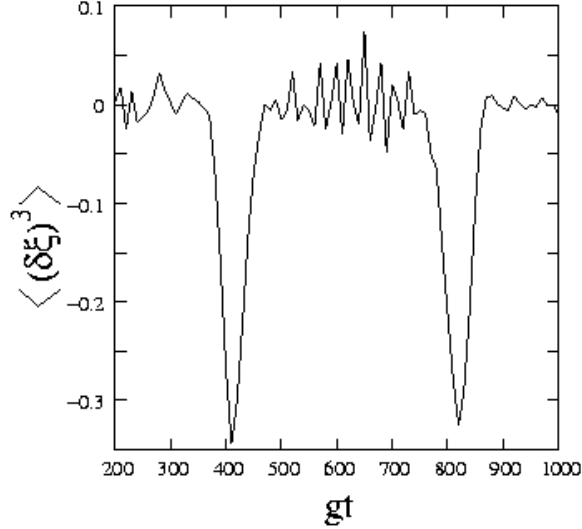


Figure 5.10:  $\langle (\delta\xi)^3 \rangle$  versus  $gt$  for an initial state  $|\alpha; 0\rangle$  with  $\nu = 5$ .

appear even in the case of an initial CS ( $m = 0$ ), as is evident from Fig. 5.10. In contrast to this, the variances and higher moments of the subsystem variables  $x_a$ ,  $x_b$ ,  $p_a$  and  $p_b$  do not display these signatures. For instance, the plot of  $\Delta x_a$  versus time shown in Fig. 5.11 does not display a distinctive signature at  $\frac{1}{2}T_{\text{rev}}$  alone: apart from oscillations in the vicinity of this instant, we see marked dips around

$\frac{1}{3}T_{\text{rev}}$  and  $\frac{2}{3}T_{\text{rev}}$  as well.

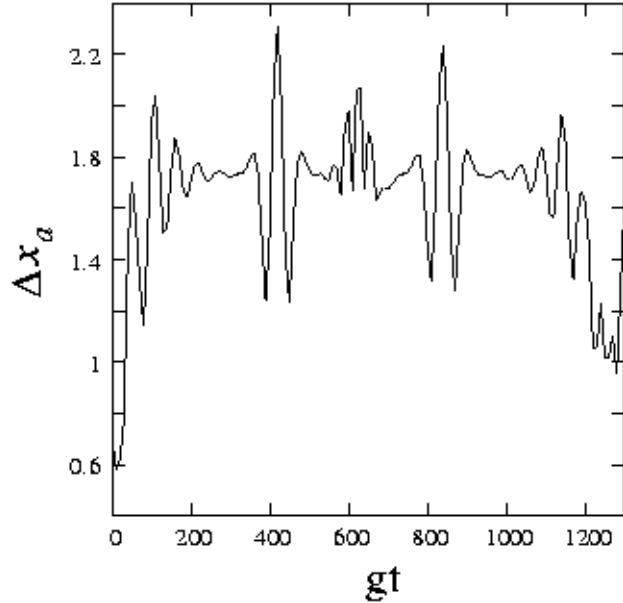


Figure 5.11:  $\Delta x_a$  versus  $gt$  for an initial state  $|\alpha; 0\rangle$  with  $\nu = 5$ .

## 5.4 Concluding remarks

In the light of our discussion, it is clear that the quadrature variables  $\xi$  and  $\eta$  corresponding to the full system are the appropriate observables whose dynamics signals the occurrence of the analogs of revival phenomena, while the expectation values of sub-system variables would seem to be less suitable choices for highlighting collapse and revival phenomena. On heuristic grounds, we may, however, expect them to be better candidates for investigating non-periodic temporal behavior — in particular, time evolution that is actually indicative of exponential instability. We address this issue in the next chapter, in which we analyze the dynamics of the sub-system variable  $\langle a^\dagger a \rangle$  for a wide range of values of the parameter  $\nu$  and the ratio  $\gamma/g$ .

# CHAPTER 6

## Ergodicity properties of entangled two-mode states - II

### 6.1 Properties of the coupled-system Hamiltonian

In this chapter, we continue our investigation of the dynamics of a single-mode electromagnetic field propagating in a nonlinear medium, with the model Hamiltonian of Eq. (5.1). We write down  $H$  again for ready reference, restoring the over-all factor of  $\hbar$  for the moment, as in Eq. (1.9):

$$H = \hbar [\omega a^\dagger a + \omega_0 b^\dagger b + \gamma b^{\dagger 2} b^2 + g (a^\dagger b + b^\dagger a)]. \quad (6.1)$$

We recall that the operators  $a$  and  $a^\dagger$  pertain to the sub-system represented by the field, while  $b$  and  $b^\dagger$  are the ladder operators for the other sub-system, the anharmonic oscillator modeling an atom of the medium. We have found in Chapter 5 that sub-system variables do not adequately capture the effects of revival phenomena. On the other hand, this would make them potentially good candidates for examining the ergodicity properties of the system. The mean photon number  $\langle \mathbf{N} \rangle = \langle a^\dagger a \rangle$ , which is also essentially the average energy of the field mode, turns out to be an ideal candidate for this purpose. Our reasons for this choice are as follows.

In the single-mode model with Hamiltonian  $\hbar \chi \mathbf{N}(\mathbf{N} - 1)$  considered in Chapters 2, 3 and 4, it is evident that the expectation value of  $\mathbf{N}$ , as well as all its higher moments, are constants of the motion for any initial state. In contrast to this,  $\mathbf{N}$  does not commute with the Hamiltonian (6.1) of the coupled system. As a consequence of the entanglement between the atom and field modes, the mean

photon number is no longer a constant of the motion for any non-zero value of the coupling constant  $g$ . However, as already stated, the total number operator  $\mathbf{N}_{\text{tot}} = a^\dagger a + b^\dagger b$  commutes with  $H$  for all values of the parameters in  $H$ . Its expectation value is therefore always a constant of the motion. In the absence of the anharmonicity parameter  $\gamma$ , the coupled Hamiltonian is essentially linear in each of the sub-system variables, and can be diagonalized in terms of linear combinations of the original ladder operators. In physical terms, this leads to fairly simple dynamics, essentially entailing a simple periodic exchange of energy between the two sub-systems or modes. (This mechanism becomes even more transparent if we set  $\omega = \omega_0$ .) When  $\gamma$  is non-zero, the dynamics is more complicated, but the existence of the operator  $\mathbf{N}_{\text{tot}}$  ensures that the system as a whole is “well-behaved”, with a discrete spectrum (labeled, as we have seen, by the quantum numbers  $N$  and  $s$ , where  $N = 0, 1, \dots$  and  $s = 0, 1, \dots, N$ ). The *time-dependence* of  $\langle \mathbf{N} \rangle$  is thus a direct consequence of the *coupling* of the field mode to another degree of freedom; and the *deviation* of  $\langle \mathbf{N} \rangle$  from *periodic* temporal variation is a probe of the effects of the *nonlinearity* in the latter. It turns out that a remarkable diversity of temporal behavior is exhibited by  $\langle \mathbf{N} \rangle$ , in different ranges of the parameters in  $H$ .

In this context, it is very helpful to understand the dynamical behavior of the completely *classical* counterpart of the Hamiltonian of Eq. (6.1). This analysis is also needed in order to facilitate subsequent comparison of the quantum dynamics with the classical one. We may obtain the classical Hamiltonian as follows. Let the linear harmonic oscillator associated with  $a$  and  $a^\dagger$  have a mass  $m$ , position  $x$  and momentum  $p_x$ . Similarly, let the oscillator associated with  $b$  and  $b^\dagger$  have a mass  $M$ , position  $y$  and momentum  $p_y$ . Putting in all constant factors (including  $\hbar$ ), we have

$$a = \sqrt{\frac{m\omega}{2\hbar}} x + \frac{ip_x}{\sqrt{2m\hbar\omega}}, \quad b = \sqrt{\frac{M\omega_0}{2\hbar}} y + \frac{ip_y}{\sqrt{2M\hbar\omega_0}}. \quad (6.2)$$

The hermitian conjugates  $a^\dagger$  and  $b^\dagger$  are of course obtained by replacing  $i$  with  $-i$  in the above. Substituting the foregoing in Eq. (6.1), we get  $H$  in terms of  $x$ ,  $p_x$ ,  $y$  and  $p_y$ . Passing to the classical limit in which  $\hbar \rightarrow 0$ , we find that



the only consistent way to obtain a non-trivial, finite expression for the classical Hamiltonian in this limit is to let  $\gamma$  also tend to zero simultaneously, such that the ratio  $\gamma/\hbar$  tends to a finite value  $\lambda$ , say. When this is done, the classical Hamiltonian obtained is

$$H_{\text{cl}} = \frac{p_x^2}{2m} + \frac{1}{2}m\omega^2x^2 + \frac{p_y^2}{2M} + \frac{1}{2}M\omega_0^2y^2 + \frac{\lambda}{\omega_0^2} \left( \frac{p_y^2}{2M} + \frac{1}{2}M\omega_0^2y^2 \right)^2 + \frac{g}{\sqrt{\omega\omega_0}} \left( \sqrt{mM}\omega\omega_0xy + \frac{p_xp_y}{\sqrt{mM}} \right), \quad (6.3)$$

with the canonical Poisson bracket relations  $\{x, p_x\} = \{y, p_y\} = 1$ . As it stands, it is not immediately obvious that the corresponding motion is bounded for all initial conditions, owing to the presence of the cross terms  $xy$  and  $p_xp_y$  that can assume either sign. However, the counterpart of  $\mathbf{N}_{\text{tot}} = a^\dagger a + b^\dagger b$ , namely,

$$N_{\text{cl}} = \frac{1}{\omega} \left( \frac{p_x^2}{2m} + \frac{1}{2}m\omega^2x^2 \right) + \frac{1}{\omega_0} \left( \frac{p_y^2}{2M} + \frac{1}{2}M\omega_0^2y^2 \right), \quad (6.4)$$

is a second, analytic, constant of the motion ( $\{N_{\text{cl}}, H_{\text{cl}}\} = 0$ ). This ensures, of course, that the two-freedom system is Liouville-Arnold integrable. Further, since  $N_{\text{cl}} = \text{constant}$  is evidently a bounded hypersurface (an ellipsoid) in the four-dimensional phase space, it is clear that motion under  $H_{\text{cl}}$  is indeed bounded for any set of initial conditions. All four Lyapunov exponents vanish, and the classical motion is always regular (and restricted to a 2-torus) for each set of initial conditions. The dynamics can be analyzed in further detail, including the identification of the location and nature of the corresponding critical or equilibrium points. Several features emerge that are interesting in their own right, but we do not go into these here, as they are not directly germane to our present purposes. We note, though, that the equation of motion of the classical counterpart of  $\mathbf{N}$  ( $= a^\dagger a$ ), on evaluating the Poisson bracket concerned, is

$$\frac{d}{dt} \left[ \frac{1}{\omega} \left( \frac{p_x^2}{2m} + \frac{1}{2}m\omega^2x^2 \right) \right] = g \left( \sqrt{\frac{m\omega}{M\omega_0}} x p_y - \sqrt{\frac{M\omega_0}{m\omega}} y p_x \right). \quad (6.5)$$

The equation of motion of the combination on the right-hand side of Eq. (6.5) involves other functions of the dynamical variables, and so on. The resulting set

of equations does not close. This is brought out more clearly in the quantum mechanical problem, to which we now revert.

Returning to the quantum mechanical Hamiltonian (6.1), some additional insight into its precise nature is provided by re-writing it in terms of angular momentum operators [34]. The latter are defined in the standard manner in terms of the two mutually commuting sets of boson operators, according to

$$J_+ = a^\dagger b, \quad J_- = ab^\dagger, \quad J_z = \frac{1}{2}(a^\dagger a - b^\dagger b). \quad (6.6)$$

The Hamiltonian in Eq. (6.1) becomes

$$H = \hbar \left[ \frac{1}{2}(\omega + \omega_0 - \gamma)\mathbf{N}_{\text{tot}} + (\omega - \omega_0 + \gamma)J_z + \frac{1}{4}\gamma(\mathbf{N}_{\text{tot}} - 2J_z)^2 + 2gJ_x \right]. \quad (6.7)$$

We also have the well known relation  $J^2 = \frac{1}{2}\mathbf{N}_{\text{tot}}(\frac{1}{2}\mathbf{N}_{\text{tot}} + 1)$ . Therefore, as  $J^2$  is a function of  $\mathbf{N}_{\text{tot}}$ , it is evident that  $\mathbf{N}_{\text{tot}}$  commutes not only with  $H$ , but also with every component  $J_i$  of the angular momentum. However,  $[J_z, J_x] \neq 0$ , of course, and this suffices to preclude exact diagonalization of  $H$ . It is clear that we have a problem similar to that of an Ising spin in a transverse magnetic field. The quantity whose time evolution we shall track is the expectation value of  $\mathbf{N} = a^\dagger a = J_z + \frac{1}{2}\mathbf{N}_{\text{tot}}$ . Using the standard algebra of angular momentum generators, the equation of motion of this operator works out to

$$\frac{d\mathbf{N}}{dt} = \frac{dJ_z}{dt} = (i\hbar)^{-1} [\mathbf{N}, H] = -ig(a^\dagger b - ab^\dagger) = 2gJ_y. \quad (6.8)$$

But we also find

$$\frac{dJ_y}{dt} = (\omega - \omega_0 - \gamma\mathbf{N}_{\text{tot}})J_x - 2gJ_z + \gamma[J_z, J_x]_+ \quad (6.9)$$

and

$$\frac{dJ_x}{dt} = (\gamma\mathbf{N}_{\text{tot}} - \omega + \omega_0 - \gamma)J_y - \gamma[J_y, J_z]_+, \quad (6.10)$$

where  $[\dots, \dots]_+$  stands for the anti-commutator of the operators concerned. When differentiated with respect to  $t$ , these terms lead to trilinear combinations of

the angular momentum operators, and so on. It is easily checked that the system of equations does not close.

Having obtained some idea of the dynamics we can expect of the operator  $\mathbf{N}$ , we now turn to a numerical study. We shall regard the mean photon number  $\langle \mathbf{N} \rangle$  (equivalently, the mean energy of the field mode) as an effective classical dynamical variable, and analyze its time series over long intervals of time. We carry out this analysis for a wide range of values of the ratio  $\gamma/g$ , which is a measure of the relative strengths of the nonlinearity and the interaction present in the coupled system. As in Chapter 5, we shall take the atomic oscillator to be initially in the ground state, and the field to be in a CS or a PACS.

In order to set the framework, in the next section we briefly outline the relevant features of time-series analysis [35], as this topic is quite distinct from those involved in the preceding parts of this thesis.

## 6.2 Time-series analysis in brief

We consider a typical situation, in which the time-series data of just one observable (signal), or that of a certain sub-set of observables corresponding to a given physical system, are available for analysis. In general, there will be other dynamical variables whose time series are not readily accessible, but which also control the full dynamics of the system. The dynamical equations are typically a set of nonlinear coupled evolution equations for the complete set of dynamical variables. In time-series analysis one attempts to ascertain, from the available data, the *effective* number of variables that are actually relevant in determining the temporal behavior of the system, consequently establishing the minimum number of effective dimensions  $d_{\text{emb}}$  (the *embedding dimension*) of the “phase space” of these relevant variables. Evidently, these variables have to be generated from the values of the observed variables at a given time and those corresponding to their time-delayed copies. Hence this space is only formally equivalent to the actual phase space of the system, and the dynamical variables generated from the data are merely effective variables. However, if the analysis is carried out appropriately, they will

(in most cases) capture the salient features of the dynamics in the actual phase space of the system — in particular, of dynamical chaos, if any.

The embedding theorem [61] indicates how  $d_{\text{emb}}$  can be obtained. To begin with, one assumes different integer values  $d$  for the dimensionality of the effective phase space, and generates the  $d$  dynamical variables from the time-series data available. Each of these variables is regarded as a component of a  $d$ -dimensional vector. The embedding dimension will turn out to be one of the values assumed for  $d$ , obtained by the procedure described below.

Generating the set of effective dynamical variables at any instant involves the identification of a *time delay*  $\tau$  such that, from the available time-series of the signal, data points separated by time intervals  $\geq \tau$  are sufficiently independent of each other to be treated as the independent dynamical variables. We assume that the time series is obtained by sampling the variable(s) concerned at time steps  $\delta t$ . Clearly, if two data points  $s(n)$  and  $s(n+T)$  at discrete times  $n$  and  $(n+T)$  (in units of  $\delta t$ ) are sufficiently independent of each other, the information deducible regarding the measured value of  $s(n)$  through the measurement of  $s(n+T)$  must tend to zero, for sufficiently large  $T$ . More precisely, if  $p(s(n))$  and  $p(s(n+T))$  are the individual probability densities for obtaining the values  $s(n)$  and  $s(n+T)$  at times  $n$  and  $(n+T)$ , respectively, and  $p(s(n), s(n+T))$  is the corresponding joint probability density, the average mutual information

$$I(T) = \sum_{s(n), s(n+T)} p(s(n), s(n+T)) \log_2 \left[ \frac{p(s(n), s(n+T))}{p(s(n)) p(s(n+T))} \right] \quad (6.11)$$

should tend to zero for sufficiently large  $T$ . In practice, a frequently-used prescription [37] is to take  $\tau$  to be that value of  $T$  at which the first minimum in  $I(T)$  occurs. Thus, from a time series  $s(0), s(1), s(2), \dots$  of the signal measured at discrete times  $t = 0, 1, 2, \dots$ , one constructs the phase space vector  $\mathbf{s}_0$  at  $t = 0$ , with components  $s(0), s(\tau), s(2\tau), \dots, s((d-1)\tau)$ . After the first time step, the vector  $\mathbf{s}_0$  evolves to  $\mathbf{s}_1$ , with components  $s(1), s(1+\tau), s(1+2\tau), \dots, s(1+(d-1)\tau)$ , and so on. This procedure is used to reconstruct sets of time-delayed vectors in the  $d$ -dimensional phase space. Each vector defines a point in the space. Taken

in the correct sequence, these points describe the time evolution of the underlying dynamical system.

This procedure is carried out for different values of  $d$ . The next task is to identify the value of  $d$  that corresponds to  $d_{\text{emb}}$ . For this purpose, we evaluate the correlation integral

$$C(r) = \lim_{n \rightarrow \infty} \frac{1}{n^2} \sum_{i,j=0}^{n-1} \theta(r - |\mathbf{s}_i - \mathbf{s}_j|) = \int_0^r d^d r' c(\mathbf{r}'). \quad (6.12)$$

$C(r)$  is an estimate of the average correlation between the various points in a phase space of a given dimensionality  $d$  that contains a large number of points  $n$  generated from the time series data. The integrand  $c(\mathbf{r})$  itself is the standard correlation function. It has been argued [36] that, for sufficiently small  $r$ ,  $C(r)$  scales like a power  $r^\zeta$  of  $r$ ; moreover, once  $d$  reaches the correct minimum embedding dimension  $d_{\text{emb}}$ , the exponent  $\zeta$  will not change with an increase in  $d$  beyond  $d_{\text{emb}}$ . This determines the exact value of  $d_{\text{emb}}$ . In practice,  $d_{\text{emb}}$  could be much smaller than the dimension of the actual phase space of the system considered. However, in a generic situation, the dynamics of the effective variables alone, in the phase space of dimensionality  $d_{\text{emb}}$ , should suffice to extract quantitative information about the dynamical chaos in the signal.

A specific objective of our study is to determine whether a sub-system variable (an appropriately chosen expectation value) can exhibit exponential sensitivity and instability, i. e., “chaotic” behavior. For this purpose we need to calculate the maximal Lyapunov exponent in the reconstructed phase space of dimensionality  $d_{\text{emb}}$ . There are, in general,  $d_{\text{emb}}$  Lyapunov exponents corresponding to the dynamics in the reconstructed phase space. For our purposes, it suffices to estimate the largest Lyapunov exponent  $\lambda_{\text{max}}$  of this set. If this quantity turns out to be a positive number, we have chaotic behavior. We use a robust algorithm [62] developed for the estimation of the maximal Lyapunov exponent from data sets represented by time series (see also [63]). We start with the set of “distances”  $\{d_j(0)\}$ , where  $d_j(0)$  is the separation between the  $j^{\text{th}}$  pair of nearest neighbors in the phase space. This evolves under the dynamics to the set of distances  $\{d_j(k)\}$

after  $k$  time steps  $\delta t$ , i. e., at time  $t = k \delta t$ . The quantity  $\langle \ln d_j(k) \rangle$ , where the angular brackets denote the average over all values of  $j$ , is plotted against the time,  $k \delta t$ . The result is, in general, a curve that has a short initial transient region, a long, clear-cut linear region, and a subsequent saturation region. The slope of the linear region, identified by a least squares fit, is precisely the largest Lyapunov exponent sought,  $\lambda_{\max}$ . Once again, it can be established that, if the procedure for phase-space reconstruction is implemented carefully and the minimum embedding dimension  $d_{\text{emb}}$  obtained correctly, any further increase in the dimensionality of the reconstructed phase space should not alter the inferences made regarding the exponential instability, if any, of the system.

With this summary of the relevant aspects of time series analysis, we proceed to carry out a detailed time series analysis of the values of the mean photon number obtained at regular intervals of time, as the single-mode field propagates in the nonlinear medium. The corresponding power spectra of the signal have been obtained using a standard package (Labview).

### 6.3 Ergodicity properties of the mean photon number

As already stated, we take the atomic oscillator in its ground state and the field to be either in a CS or a PACS, initially. Again, as in Chapter 5, we set  $\omega = \omega_0 = 1$  for illustrative purposes. We first consider the case of weak nonlinearity, i. e.,  $\gamma/g \ll 1$ , with  $\nu = 1$ . We recall from Chapter 5 that, if  $\gamma/g \ll 1$  and  $\nu$  is sufficiently small, then the state exhibits revivals (or approximate revivals) if the field mode is initially a CS or a PACS. Distinctive signatures of such revivals show up both in the entropy of entanglement and in the dynamics of appropriately chosen quadrature variables. At revivals (or near revivals), the expectation values of all observables return to their initial values (or to the neighborhood of those values). In a classical phase space spanned by these expectation values, the trajectories may therefore be expected to be periodic or ergodic (as in the case of quasi-periodicity), but

not chaotic, in any case. However, while this indicates that the system as a whole (comprising, in our case, the field and atom modes in interaction with each other) is a non-chaotic dynamical system, there is no *à priori* reason to assume that this remains true for the field or atom sub-systems taken individually — particularly because the sub-system variables do not necessarily capture signatures of the revival phenomena, as pointed out in the preceding chapter. Keeping these aspects in mind, we have analyzed the time series data of the mean photon number  $N$ , and examined the plots of the corresponding power spectrum  $S(f)$  (which is essentially the Fourier transform of the autocorrelation function of the mean photon number,  $f$  denoting the frequency), in order to make deductions regarding the nature of the dynamics. The frequency ratio  $f/g$  is clearly the counterpart of the dimensionless time variable  $gt$  in terms of which the dynamics of the field mode has been investigated in Chapter 5. As a representative case of weak nonlinearity, we have chosen (as before) the parameter values  $\gamma = 1$  and  $g = 100$ . The time step we have used in the numerical work related to this case is  $\delta t = 10^{-2}$ . Figure 6.1 (a), which is a plot of the logarithm of the power spectrum versus  $f/g$  when the initial state is  $|\alpha; 0\rangle$ , corresponds to quasi-periodic behavior. With increasing departure

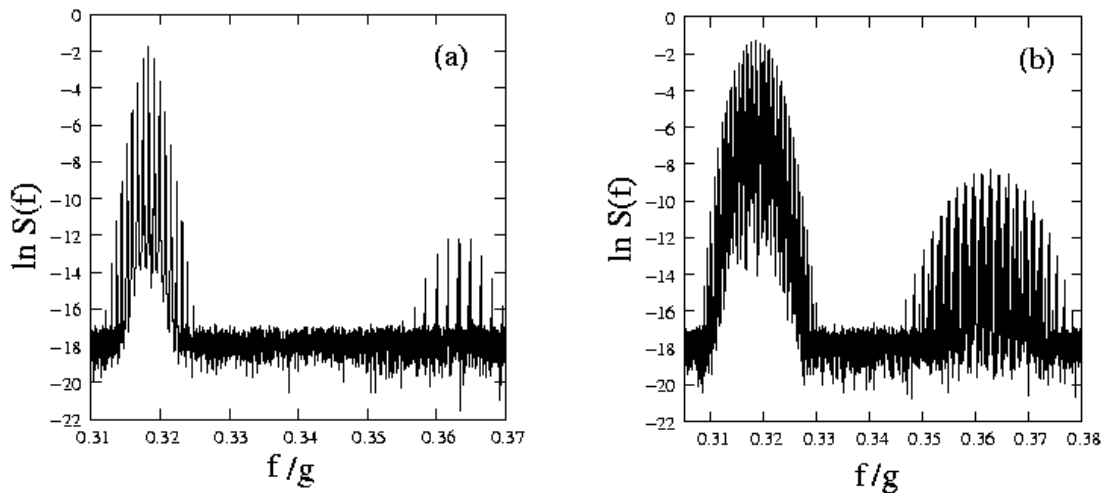


Figure 6.1: Power spectrum of the mean photon number for the initial states (a)  $|\alpha; 0\rangle$  and (b)  $|(\alpha, 5); 0\rangle$  with  $\gamma/g = 10^{-2}$  and  $\nu = 1$ .

from coherence of the initial field mode, the number of frequencies seen in the power spectrum increases, as is evident from Fig. 6.1 (b), which corresponds to an initial state  $|(\alpha, 5); 0\rangle$ . Further, for a given initial state, the number of

characteristic frequencies in the power spectrum increases with an increase in  $\nu$ . This is evident when we compare Figs. 6.1 (b) and Fig. 6.2, which depicts the

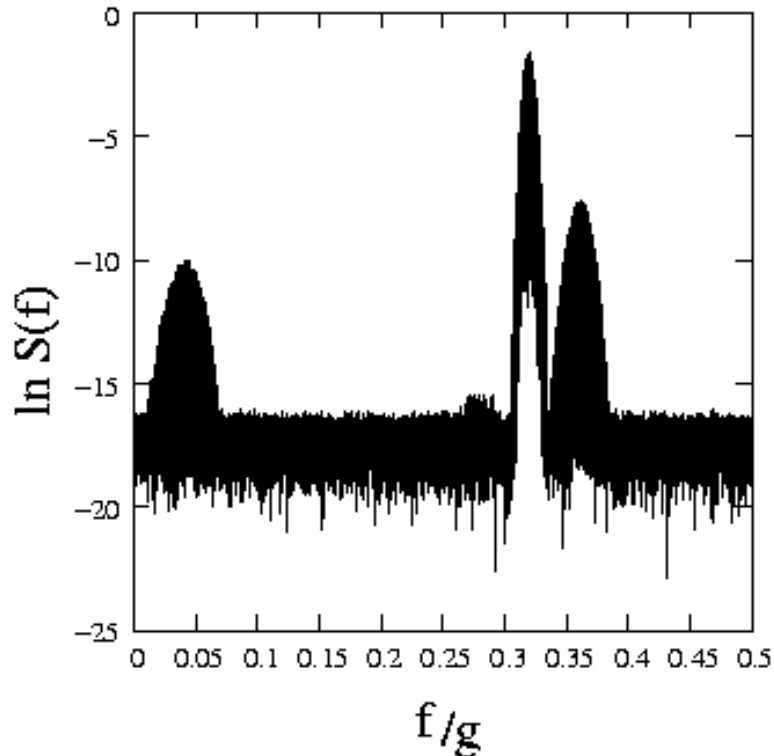


Figure 6.2: Power spectrum of  $\langle N \rangle$  for an initial state  $|(\alpha, 5); 0\rangle$  with  $\gamma/g = 10^{-2}$  and  $\nu = 5$ .

power spectrum for the same situation, but with  $\nu = 5$ . The embedding dimension turns out to be  $d_{\text{emb}} = 3$  in all these cases, and a detailed time-series analysis confirms that the maximum Lyapunov exponent is zero.

In contrast to the case of weak nonlinearity, the nature of the dynamics of the sub-system changes drastically when  $\gamma/g \gtrsim 1$ . It ranges from quasi-periodicity to fully-developed chaos, depending on the precise nature of the initial state. As representative values for this nonlinearity-dominated regime, we have set  $\gamma = 5$ ,  $g = 1$ . We use a time step  $\delta t = 10^{-1}$  in this instance, so that  $g \delta t = 10^{-1}$ , as this suffices to pick up the oscillations in the variables concerned. We first examine the case corresponding to  $\nu = 1$ . For an initial field mode which is a CS, both the time series and the power spectrum confirm that the sub-system dynamics is not chaotic. In contrast to this, an initial field state that is a PACS leads to chaotic behavior, for sufficiently large values of  $m$ . The time series analysis yields a value



$d_{\text{emb}} = 5$  in this case. Figure 6.3 shows the variation of  $\langle \ln d_j(k) \rangle$  with  $t$  for an

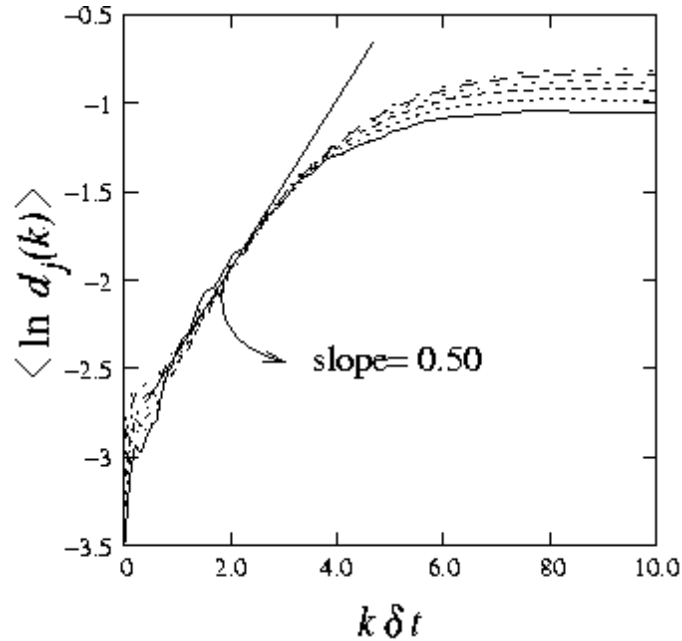


Figure 6.3:  $\langle \ln d_j(k) \rangle$  versus  $t = k \delta t$  for an initial state  $|(\alpha, 5); 0\rangle$  with  $\gamma/g = 5$  and  $\nu = 1$ . The solid line corresponds to  $d_{\text{emb}} = 5$ . The dotted lines correspond to values of  $d_{\text{emb}}$  from 6 to 10.

initial state  $|(\alpha, 5); 0\rangle$ . It is evident that the slope is positive (the actual value being  $\approx 0.5$ ), indicating that the mean energy of the field mode varies chaotically in time.

In each case, we have increased the dimensions of the phase space beyond the embedding dimension, and verified that the value of the maximal Lyapunov exponent is a constant independent of this increase. Further, we have verified in each case that, if  $\langle b^\dagger b \rangle$  is chosen as the signal for which the time series data is computed, the behavior is similar to that inferred from the dynamics of  $\langle a^\dagger a \rangle$ , in such a manner that  $\langle a^\dagger a \rangle + \langle b^\dagger b \rangle$  is a constant, as required. This lends support to the conclusion that round-off or truncation errors may be ruled out as the source of the computed chaotic behavior.

For a given value of  $\gamma/g$ , an increase in either  $\nu$  or  $m$  in the initial PACS results in an increase in the value of  $\lambda_{\text{max}}$ . This is evident from Figs. 6.4 and 6.5, where plots of  $\langle \ln d_j(k) \rangle$  versus  $t$  are shown for initial states  $|(\alpha, 1); 0\rangle$  and  $|(\alpha, 5); 0\rangle$  for  $\nu = 5$ . We find that  $\lambda_{\text{max}} \approx 0.58$  and  $0.85$ , respectively, in these two

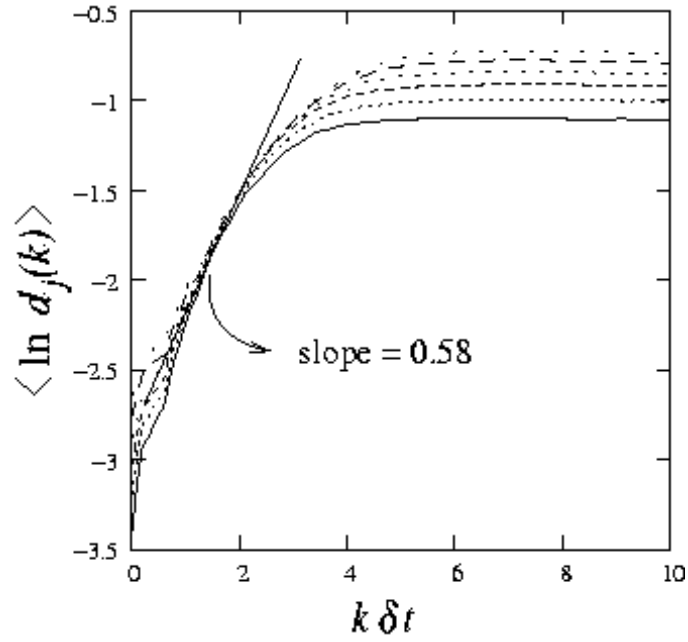


Figure 6.4:  $\langle \ln d_j(k) \rangle$  versus  $t$  for an initial state  $|(\alpha, 1); 0\rangle$  with  $\gamma/g = 5$  and  $\nu = 5$ . The solid line corresponds to embedding dimension equal to 5. The dotted lines correspond to values of  $d_{\text{emb}}$  from 6 to 10.

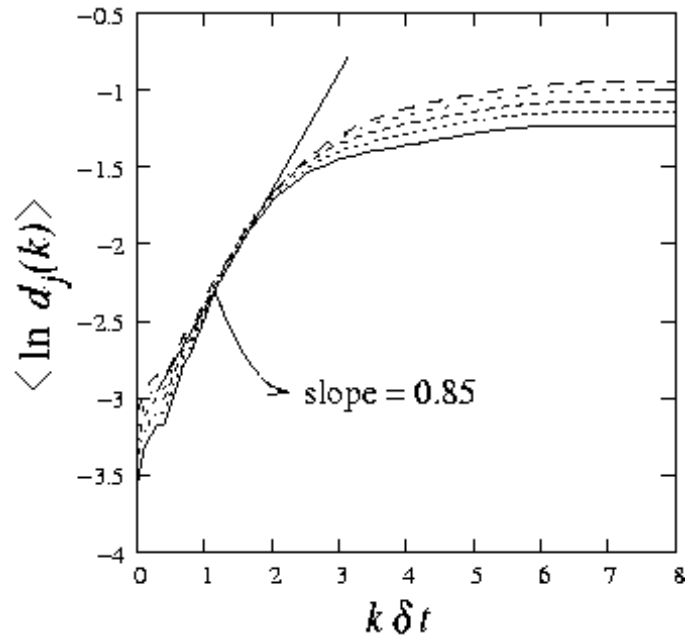


Figure 6.5:  $\langle \ln d_j(k) \rangle$  versus  $t$  for an initial state  $|(\alpha, 5); 0\rangle$  with  $\gamma/g = 5$  and  $\nu = 5$ . The solid line corresponds to  $d_{\text{emb}} = 6$ . The dotted lines correspond to values of  $d_{\text{emb}}$  from 7 to 10.

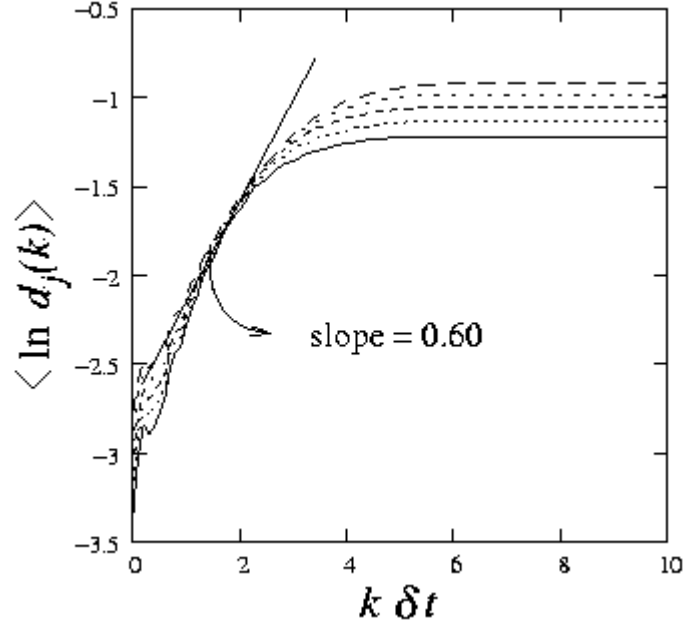


Figure 6.6:  $\langle \ln d_j(k) \rangle$  versus  $t$  for an initial state  $|\alpha; 0\rangle$  with  $\gamma/g = 5$  and  $\nu = 10$ . The solid line corresponds to embedding dimension equal to 5. The dotted lines correspond to values of  $d_{\text{emb}}$  from 6 to 10.

cases. In contrast, there is no chaotic behavior for these values of the parameters if the initial state of the field is coherent. However, with a further increase in  $\nu$ , this situation changes, and  $\langle N \rangle$  varies chaotically even for an initial coherent field mode. This is demonstrated in Fig. 6.6 showing  $\langle \ln d_j(k) \rangle$  versus  $t$  for an initial state  $|\alpha; 0\rangle$  with  $\nu = 10$ . The corresponding value of  $\lambda_{\text{max}}$  is also quite large,  $\approx 0.60$ .

To summarize: a time series and power spectrum analysis shows that, for small values of the ratio of the anharmonicity parameter to the strength of the inter-mode coupling, the dynamics of the expectation value of the mean photon number (or mean energy) of the field mode ranges from periodic to ergodic, but not chaotic, essentially independent of the nature of the initial state. On the other hand, for sufficiently large values of this ratio, the ergodicity properties of the sub-system representing the field mode depend significantly on the extent of departure from coherence of the initial field mode. In particular,  $\lambda_{\text{max}}$  is larger in the case of an initial field state that is a photon-added coherent state, compared to its value for initial coherent state. Table 6.1 provides a bird's eye view of these conclusions.

		Increasing departure from coherence $\longrightarrow$		
		Initial state		
		$ \alpha ; 0\rangle$	$ (\alpha, 1) ; 0\rangle$	$ (\alpha, 5) ; 0\rangle$
Increasing nonlinearity $\downarrow$	$\gamma/g=10^{-2}$ $ \alpha ^2=v=1$	regular	regular	regular
	$\gamma/g=10^{-2}$ $v=5$	regular	regular	regular
	$\gamma/g=5$ $v=1$	regular	regular	chaotic $\lambda_{\max} \approx 0.50$
	$\gamma/g=5$ $v=5$	regular	chaotic $\lambda_{\max} \approx 0.58$	chaotic $\lambda_{\max} \approx 0.85$
	$\gamma/g=5$ $v=10$	chaotic $\lambda_{\max} \approx 0.60$	chaotic $\lambda_{\max} \approx 0.80$	chaotic $\lambda_{\max} \approx 1.00$

Table 6.1: Qualitative dynamical behavior of the mean photon number of a single-mode electromagnetic field interacting with a nonlinear medium. “Regular”  $\Rightarrow \lambda_{\max} = 0$ .

We have already shown that the classical counterpart of the Hamiltonian under study (Eq. (6.3)) corresponds to bounded motion in phase space, and that the system is integrable, with all its Lyapunov exponents equal to zero. We have also seen that the quantum Hamiltonian (Eq.(6.1)) commutes with the total number operator  $N_{\text{tot}}$ , and has a discrete energy spectrum for all values of the parameters in  $H$ . What is the interpretation, then, of a positive value for  $\lambda_{\max}$  as deduced from the time series for the sub-system variable  $\langle a^\dagger a \rangle$  (equivalently,  $\langle b^\dagger b \rangle$ )?

This is best understood by appreciating the role of recurrence theorems and ergodicity in both classical and quantum dynamics. In classical physics, ergodicity itself is intimately linked with the Poincaré recurrence theorem. This theorem essentially states that any phase space configuration of a system enclosed in a finite volume will be repeated to an arbitrary degree of accuracy after a finite, though perhaps very long, time. Quantum analogs of this classical recurrence theorem have been established and applied to diverse situations. Exact revivals or near-revivals of a quantum state occur [64] in systems with discrete energy eigenvalues.

Further, it has been argued [65] that under any time-periodic Hamiltonian, a non-resonant, bounded quantum system will return to its original form several times during its dynamics, and this has been illustrated using computer experiments. Further, the link between wave packet revivals, and geometric phases in quantum physics and classical recurrences on the circle map has been examined [66]. Inspired by the seminal work of Fermi, Pasta and Ulam [67] on the recurrences of the initial state of a chain of nonlinearly coupled oscillators, several investigations have been carried out over the years on a wide variety of physical systems, in order to understand the conditions under which recurrences occur. In particular, it has been argued [68] that wave packet recurrences (exact revivals and near-revivals) and the Fermi-Pasta-Ulam recurrences have the same origin: if the initial quantum state can be represented as a superposition of eigenstates, and the spectrum is non-equispaced, recurrences are bound to occur.

On the other hand, high-resolution tracking of quantum and classical evolutions of a system will reveal differences in the dynamics of the expectation values of corresponding observables in these two cases. As indicated in Chapter 1, the origin of this dichotomy can be traced back to the inadequacy of the naive Ehrenfest theorem (which does not generally take into account the non-commutativity between  $x$  and  $p$ , as seen from Eq.(1.6)) in retrieving the classical regime of the quantum system. An outcome of this feature is that *the Lyapunov exponents that characterize the dynamical behavior of classical and quantum expectation values of the same observable can indeed be very different from each other* [69]. Two interesting observations [70] have been made in this context: (a) In isolated quantum systems with a discrete energy spectrum, using unitarity and the Schwarz inequality, it can be established that the Lyapunov exponents would vanish, if computed from time-series data collected over a sufficiently long time (which, in practice, could even turn out to be considerably longer than the characteristic time scales in the problem), indicative of non-chaotic behavior. (b) However, once measurement upon the system is included through appropriate interaction with an external system, the corresponding Lyapunov exponents need not vanish. This would suggest that, in principle, the dynamics of a *sub*-system, as deduced from time-series data of certain variables, may show exponential instability, even if the

system as a whole does not. The presence of hyperbolic (sets of) critical points in the corresponding classical version of the dynamical system plays a significant role in this regard. The “chaotic” behavior displayed by the mean photon number  $\langle a^\dagger a \rangle$  in the system we have considered may be understood in the light of these observations. Ultimately, the exponential instability associated with a positive Lyapunov exponent is an indication of the manner in which an initial wave packet spreads as it evolves in time.

# CHAPTER 7

## Conclusion

In the preceding chapters, we have described our results in detail, and also summarized them at appropriate places throughout the text. It remains to place the work in a broader perspective, and to list interesting open problems and avenues for future work.

In general terms, the present work may be viewed as addressing an aspect of the broad theme of understanding the manner in which the notions of ergodicity and varying degrees of randomness, that are well-defined and notable features of classical dynamics, get modified in quantum dynamics. In specific terms, we have studied several aspects of wave packet dynamics that shed light on non-classical effects such as revivals and fractional revivals. As emphasized in the preceding chapters, such effects are striking manifestations of quantum mechanical interference phenomena. They show up in distinctive fashion in the expectation values of observables and their higher moments, in different kinds of squeezing, and in other indicators such as entropies and quasi-probability distributions, as elaborated upon in the foregoing. We have worked in the framework of two specific, rather simple, model Hamiltonians pertinent to a nonlinear medium. However, these models capture many of the essential features of nonlinearity, anharmonicity and inter-mode coupling. In this sense, the results arrived at enable us to draw conclusions that may be expected to remain valid in their broad features, if not in detail, in other modified situations as well.

Our results also suggest a number of avenues for further exploration. We list some of these here, roughly in the order of progression of the text of this thesis.

We have examined the revival phenomena exhibited by a single-mode coherent state or a photon-added coherent state as it propagates through a Kerr-like medium. It would be of interest to investigate their counterparts for other initial

states, such as photon-*subtracted* coherent states [9] and various squeezed states of light.

The Wigner function is only one particular way of arriving at a non-classicality indicator in the situations considered in this thesis. Others, such as the Sudarshan-Glauber  $P$ -representation [32] and the Husimi-Kano function [71], are also worth exploring, as is the extension of these considerations to the interacting two-mode case.

The interacting two-mode case we have considered involves a bipartite Hamiltonian. What would happen if this were not the case — for instance, if we considered three sub-systems coupled to each other? Further, if such a system were classically non-integrable, what sort of dynamical behavior would the quantum mechanical counterpart exhibit?

The sub-system entropies we have considered (the von Neumann entropy and the linear entropy) are just two of several possible measures of entanglement, and they seem to exhibit essentially similar behavior, at least in the cases we have examined. What about other measures of entanglement, and what is the most appropriate or optimal measure for the purposes at hand?

Finally, as perhaps the most interesting general question that arises in the present context: what are the possibilities and implications for quantum computation using continuous variables (e. g., Gaussian wave packets), exploiting revival phenomena? It is evident that there exists a rich vein of interesting problems for further research in this area.



# Appendices

# APPENDIX A

## Calculation of $\langle a^{\dagger r} a^{r+s} \rangle$ for an initial PACS $|\alpha, m\rangle$ propagating in a Kerr-like medium

The Hamiltonian governing the dynamics of the wave packet  $|\psi\rangle$  is given by  $H = \chi \mathbf{N}(\mathbf{N} - 1)$  where  $\mathbf{N} = a^{\dagger}a$ . The initial state  $|\psi(0)\rangle$  is the PACS  $|\alpha, m\rangle$ . The state at any  $t \geq 0$  is given by

$$|\psi(t)\rangle = e^{-i\chi \mathbf{N}(\mathbf{N}-1)t} |\alpha, m\rangle. \quad (\text{A.1})$$

Introducing complete sets of Fock states  $\sum_{l=0}^{\infty} |l\rangle \langle l|$  ( $= 1$ ) at appropriate places, we have

$$\begin{aligned} \langle \psi(t) | a^{\dagger r} a^{r+s} | \psi(t) \rangle &= \sum_{l=0}^{\infty} \sum_{n=0}^{\infty} \sum_{u=0}^{\infty} \sum_{v=0}^{\infty} \langle \alpha, m | l \rangle \langle l | e^{i\chi \mathbf{N}(\mathbf{N}-1)t} | n \rangle \\ &\times \langle n | a^{\dagger r} a^{r+s} | u \rangle \langle u | e^{-i\chi \mathbf{N}(\mathbf{N}-1)t} | v \rangle \langle v | \alpha, m \rangle. \end{aligned} \quad (\text{A.2})$$

Since our initial state is the PACS  $|\alpha, m\rangle$ , it is convenient to use the notation

$$\langle a^{\dagger r} a^{r+s} \rangle_m = \langle \psi(t) | a^{\dagger r} a^{r+s} | \psi(t) \rangle. \quad (\text{A.3})$$

When  $m = 0$  (corresponding to an initial CS), we will write the expectation value as simply  $\langle a^{\dagger r} a^{r+s} \rangle$ . On using

$$a^p |u\rangle = \left[ \frac{u!}{(u-p)!} \right]^{1/2} |u-p\rangle$$

and the orthogonality property of the basis states, Eq. (A.2) simplifies to

$$\begin{aligned} \langle a^{\dagger r} a^{r+s} \rangle_m &= \sum_{l=0}^{\infty} \left[ \frac{(l+s)!}{l!} \right]^{1/2} \frac{l!}{(l-r)!} e^{-i\chi[(l+s)(l+s-1)-l(l-1)]t} \\ &\times \langle \alpha, m | l \rangle \langle l+s | \alpha, m \rangle. \end{aligned} \quad (\text{A.4})$$

Here, and in the rest of this Appendix, it is understood that contributions from terms of the form  $1/(-n)!$ , where  $n$  is a positive integer, vanish. (Note that the gamma function  $\Gamma(1-n)$  diverges for  $n = 1, 2, \dots$ .) Expanding  $|\alpha, m\rangle$  in the Fock basis, we find

$$\langle \alpha, m | l \rangle = \frac{e^{-\nu/2} (\alpha^*)^{l-m} \sqrt{l!}}{\sqrt{m! L_m(-\nu)} (l-m)!}, \quad (\text{A.5})$$

where  $\nu = |\alpha|^2$  and  $L_m$  is the Laguerre polynomial of order  $m$ . We use the definitions [72]

$$L_m(\mu) = \sum_{n=0}^m \binom{m}{n} \frac{(-\mu)^n}{n!} = \frac{e^\mu}{m!} \frac{d^m}{d\mu^m} (\mu^m e^{-\mu}) \quad (\text{A.6})$$

and

$$L_m^s(\mu) = \sum_{n=0}^m \binom{m+s}{n+s} \frac{(-\mu)^n}{n!} = \frac{e^\mu \mu^{-s}}{m!} \frac{d^m}{d\mu^m} (\mu^{m+s} e^{-\mu}) \quad (\text{A.7})$$

for the Laguerre and associated Laguerre polynomials. Equation (A.4) reduces to

$$\langle a^{\dagger r} a^{r+s} \rangle_m = \frac{e^{-\nu}}{m! L_m(-\nu)} \sum_{l=0}^{\infty} \frac{l!}{(l-r)! (l+s-m)!} \frac{(l+s)!}{(l-m)!} \frac{\alpha^s \nu^{l-m}}{(l-m)!} e^{-i\chi s(s-1)t} e^{-2i\chi l s t}. \quad (\text{A.8})$$

But

$$\frac{(l+s)!}{(l+s-m)!} \nu^{l-m} = \nu^{-s} \frac{d^m}{d\nu^m} (\nu^{l+s}), \quad (\text{A.9})$$

so that

$$\langle a^{\dagger r} a^{r+s} \rangle_m = \frac{\alpha^s e^{-\nu} e^{-i\chi s(s-1)t}}{\nu^s m! L_m(-\nu)} \sum_{l=0}^{\infty} \frac{e^{-2i\chi l s t}}{(l-m)!} \frac{d^m}{d\nu^m} \left( \nu^{r+s} \frac{d^r \nu^l}{d\nu^r} \right). \quad (\text{A.10})$$

This can be re-expressed as

$$\langle a^{\dagger r} a^{r+s} \rangle_m = \frac{\alpha^s e^{-\nu} e^{-i\chi s(s-1)t}}{\nu^s m! L_m(-\nu)} \sum_{n=0}^m \binom{m}{n} \left( \frac{d^n \nu^{r+s}}{d\nu^n} \right) \frac{d^{m-n+r}}{d\nu^{m-n+r}} \sum_{l=0}^{\infty} \frac{e^{-2i\chi l s t} \nu^l}{(l-m)!}. \quad (\text{A.11})$$

Simplifying, we find (after some straightforward algebra)

$$\langle a^{\dagger r} a^{r+s} \rangle_m = \frac{\alpha^s e^{-\nu} e^{-i\chi(s-1+2m)st}}{\nu^s L_m(-\nu) m!} \frac{d^m}{d\nu^m} \left( \nu^{r+s} \frac{d^r}{d\nu^r} [\nu^m \exp(\nu e^{-2is\chi t})] \right). \quad (\text{A.12})$$

This can be re-cast in the form

$$\begin{aligned} \langle a^{\dagger r} a^{r+s} \rangle_m &= \frac{\alpha^s e^{-\nu} e^{-i\chi(s-1+2m)st}}{\nu^s L_m(-\nu)} \sum_{n=n_{\min}}^r \binom{r}{n} \frac{e^{-2is\chi nt}}{(m-r+n)!} \\ &\times \frac{d^m}{d\nu^m} [\nu^{m+s+n} \exp(\nu e^{-2is\chi t})], \end{aligned} \quad (\text{A.13})$$

where  $n_{\min} = \max(0, r-m)$ . Using the definition in Eq. (A.7) for the associated Laguerre polynomial  $L_m^s$  we get, finally,

$$\begin{aligned} \langle a^{\dagger r} a^{r+s} \rangle_m &= \alpha^s \exp[-\nu - i\chi(s-1+2m)st + \nu e^{-2is\chi t}] \\ &\times \sum_{n=n_{\min}}^r \binom{r}{n} \frac{m! (\nu e^{-2is\chi t})^n}{(m-r+n)!} \frac{L_m^{s+n}(-\nu e^{-2is\chi t})}{L_m(-\nu)}. \end{aligned} \quad (\text{A.14})$$

This form of the expression for  $\langle a^{\dagger r} a^{r+s} \rangle_m$  at an arbitrary time  $t$ , corresponding to the initial state  $|\alpha, m\rangle$ , is used for numerical calculations.

Setting  $m = 0$  in Eq. (A.14), we obtain

$$\langle a^{\dagger r} a^{r+s} \rangle = \alpha^s \nu^r e^{-\nu(1-\cos 2s\chi t)} \exp[-i\chi(s(s-1) + 2rs)t - i\nu \sin 2s\chi t] \quad (\text{A.15})$$

as the corresponding expression for an initial coherent state  $|\alpha\rangle$ .

## APPENDIX B

### Analytic expressions for $\langle x(t) \rangle$ and $\langle p(t) \rangle$ for an initial PACS

Setting  $r = 0$  and  $s = 1$  in Eq. (A.14), we get

$$\langle a \rangle_m = \frac{\alpha e^{-\nu}}{L_m(-\nu)} e^{-2im\chi t} \exp(\nu e^{-2i\chi t}) L_m^1(-\nu e^{-2i\chi t}). \quad (\text{B.1})$$

The expectation values  $\langle x(t) \rangle_m$  and  $\langle p(t) \rangle_m$  (i.e., the mean values of  $x$  and  $p$  at time  $t$  in the case of the initial PACS  $|\alpha, m\rangle$ ) can now be calculated using Eq. (B.1) and its complex conjugate, which yields  $\langle a^\dagger \rangle_m$ .

Recall that

$$\langle x(t) \rangle_m = \sqrt{2} \operatorname{Re} \langle a \rangle_m \quad \text{and} \quad \langle p(t) \rangle_m = \sqrt{2} \operatorname{Im} \langle a \rangle_m, \quad (\text{B.2})$$

where we emphasize that  $\langle a \rangle_m$  is computed at time  $t$ , and the suffix  $m$  is meant to denote the fact that the initial state considered is  $|\alpha, m\rangle$ . We find

$$\langle x(t) \rangle_m = \frac{\sqrt{2} e^{-\nu(1-\cos 2\chi t)}}{L_m(-\nu)} \operatorname{Re} \left\{ \alpha \exp[-i(2m\chi t + \nu \sin 2\chi t)] L_m^1(-\nu e^{-2i\chi t}) \right\} \quad (\text{B.3})$$

and

$$\langle p(t) \rangle_m = \frac{\sqrt{2} e^{-\nu(1-\cos 2\chi t)}}{L_m(-\nu)} \operatorname{Im} \left\{ \alpha \exp[-i(2m\chi t + \nu \sin 2\chi t)] L_m^1(-\nu e^{-2i\chi t}) \right\}. \quad (\text{B.4})$$

Setting  $m = 0$  in the above equations, we obtain the corresponding expressions for the case of an initial CS, as written down in Eqs. (2.19) and (2.20).

Returning to the case of an initial PACS  $|\alpha, m\rangle$ , we see from Eqs. (B.3) and

(B.4) that the initial values of the expectation values concerned are given by

$$\langle x(0) \rangle_m = \frac{L_m^1(-\nu)}{L_m(-\nu)} x_0, \quad \langle p(0) \rangle_m = \frac{L_m^1(-\nu)}{L_m(-\nu)} p_0, \quad (\text{B.5})$$

where  $x_0 + ip_0 = \alpha\sqrt{2}$ . The difference

$$\langle x(t) \rangle_m - i \langle p(t) \rangle_m = \sqrt{2} \langle a^\dagger \rangle_m \quad (\text{B.6})$$

deserves special mention. We find

$$\langle x(t) \rangle_m - i \langle p(t) \rangle_m = \sqrt{2} \frac{\alpha^* e^{-\nu}}{L_m(-\nu)} e^{2im\chi t} \exp(\nu e^{2i\chi t}) L_m^1(-\nu e^{2i\chi t}). \quad (\text{B.7})$$

This can be rewritten in the compact form

$$\langle x(t) \rangle_m - i \langle p(t) \rangle_m = (x_0 - ip_0) \frac{e^{-\nu(1-\zeta)} \zeta^m L_m^1(-\nu \zeta)}{L_m(-\nu)}, \quad (\text{B.8})$$

where  $\zeta(t) = \exp(2i\chi t)$ .

It is convenient to define the quantities

$$X_m(t) = \langle x(t) \rangle_m \exp[\nu(1 - \cos 2\chi t)] \quad \text{and} \quad P_m(t) = \langle p(t) \rangle_m \exp[\nu(1 - \cos 2\chi t)]. \quad (\text{B.9})$$

Using the expressions for  $\langle x(t) \rangle_m$  and  $\langle p(t) \rangle_m$  in Eqs. (B.3) and (B.4), we get

$$\begin{aligned} X_m(t) &= \frac{1}{L_m(-\nu)} \operatorname{Re} \left\{ (x_0 + ip_0) \exp[-i(2m\chi t + \nu \sin 2\chi t)] L_m^1(-\nu e^{-2i\chi t}) \right\}, \\ P_m(t) &= \frac{1}{L_m(-\nu)} \operatorname{Im} \left\{ (x_0 + ip_0) \exp[-i(2m\chi t + \nu \sin 2\chi t)] L_m^1(-\nu e^{-2i\chi t}) \right\}. \end{aligned} \quad (\text{B.10})$$

These can be written after some straightforward algebra in the concise form

$$\left. \begin{aligned} X_m(t) &= x_0 \operatorname{Re} z_m(t) + p_0 \operatorname{Im} z_m(t), \\ P_m(t) &= p_0 \operatorname{Re} z_m(t) - x_0 \operatorname{Im} z_m(t), \end{aligned} \right\} \quad (\text{B.11})$$

where

$$z_m(t) = \frac{L_m^1(-\nu e^{2i\chi t})}{L_m(-\nu)} \exp [i(2m\chi t + \nu \sin 2\chi t)]. \quad (\text{B.12})$$

For ready reference, we have written out Eqs. (B.11) and (B.12) once again in Chapter 3 (Eqs. (3.8) and (3.9), respectively). In deriving the expressions above, we have made frequent use of the fact that  $e^z$  and  $L_m^s(z)$  are real analytic functions of  $z$ : that is, they satisfy  $f(z^*) = f^*(z)$ .

## APPENDIX C

### Calculation of $D_q^{(m)}(t)$ for an initial PACS $|\alpha, m\rangle$

Setting  $r = 0$  and  $s = q$  (a non-negative integer) in Eq. (A.14) of Appendix A and using the series expansion for the associated Laguerre polynomial, we get

$$\begin{aligned} \langle a^q \rangle_m &= \frac{e^{-\nu(1-\cos 2q\chi t)}}{L_m(-\nu)} \nu^q \sum_{n=0}^m \frac{(m+q)! \nu^n}{(m-n)! (n+q)! n!} \\ &\times \exp \left\{ -i [(q-1 + 2m + 2n) \chi q t + \nu \sin 2\chi q t - q\theta] \right\}, \end{aligned} \quad (\text{C.1})$$

where  $\theta$  is the argument of  $\alpha$ , that is,  $\alpha = \nu^{1/2} e^{i\theta}$ . Similarly, when  $r = q$  and  $s = 0$ , Eq. (A.14) gives

$$\langle a^{\dagger q} a^q \rangle_m = \frac{1}{L_m(-\nu)} \sum_{n=n_{\min}}^q \binom{q}{n} \frac{m!}{(m-q+n)!} \nu^n L_m^n(-\nu), \quad (\text{C.2})$$

where  $n_{\min}$  is now given by  $\max(0, q-m)$ . The quantity  $D_q^{(m)}(t)$  for an initial state  $|\alpha, m\rangle$  can now be calculated using the definition (see Chapter 4, Eq. (4.12))

$$D_q^{(m)}(t) = \frac{2 \left[ \text{Re} \langle a^{2q} \rangle_m - 2 (\text{Re} \langle a^q \rangle_m)^2 + \langle a^{\dagger q} a^q \rangle_m \right]}{\langle F_q(\mathbf{N}) \rangle_m}. \quad (\text{C.3})$$

Here  $F_q(\mathbf{N}) = [a^q, a^{\dagger q}]$ . After some algebra, we find that the operator  $F_q(\mathbf{N})$  is a polynomial of order  $(q-1)$  in the number operator  $\mathbf{N} = a^\dagger a$ , given by

$$F_q(\mathbf{N}) = q! \left[ 1 + \sum_{n=1}^{q-1} \binom{q}{n} \frac{1}{n!} \left\{ \mathbf{N}(\mathbf{N}-1) \cdots (\mathbf{N}-(n-1)) \right\} \right]. \quad (\text{C.4})$$

Since  $\mathbf{N}$  commutes with the Hamiltonian  $H = \chi \mathbf{N}(\mathbf{N}-1)$ , it follows that  $\langle F_q(\mathbf{N}) \rangle$  is also a constant of the motion, and its value remains the same as its initial value computed in the state  $|\alpha, m\rangle$ .

Substituting the values for  $\text{Re} \langle a^q \rangle_m$ ,  $\text{Re} \langle a^{2q} \rangle_m$  and  $\langle a^{\dagger q} a^q \rangle_m$  in Eq. (C.3), we



get

$$\begin{aligned}
\frac{1}{2} L_m(-\nu) \langle F_q(\mathbf{N}) \rangle_m D_q^{(m)}(t) &= e^{-\nu(1-\cos 4\chi qt)} \sum_{n=0}^m \binom{m+2q}{n+2q} \frac{\nu^{n+q}}{n!} \\
&\times \cos \left[ 2(2m+2n+2q-1)\chi qt + \nu \sin 4\chi qt - 2q\theta \right] \\
&- \frac{2e^{-2\nu(1-\cos 2\chi qt)}}{L_m(-\nu)} \left\{ \sum_{n=0}^m \binom{m+q}{n+q} \frac{\nu^{n+q/2}}{n!} \right. \\
&\times \cos \left[ (q-1+2m+2n)\chi qt + \nu \sin 2\chi qt - q\theta \right] \left. \right\}^2 \\
&+ \sum_{n=n_{\min}}^q \binom{q}{n} \frac{m!}{(m-q+n)!} \nu^n L_m^n(-\nu), \quad (C.5)
\end{aligned}$$

where  $n_{\min} = \text{Max}(0, q-m)$ . When  $m=0$  (corresponding to an initial CS),  $D_q^{(0)}$  simplifies to

$$\begin{aligned}
D_q^{(0)}(t) &= \frac{2\nu^q}{\langle F_q(\mathbf{N}) \rangle} \left\{ 1 + e^{-2\nu \sin^2 2\chi qt} \cos(2\chi q(2q-1)t + \nu \sin 4\chi qt - 2q\theta) \right. \\
&\quad \left. - 2e^{-4\nu \sin^2 q\chi t} \cos^2(\chi q(q-1)t + \nu \sin 2\chi qt - q\theta) \right\}. \quad (C.6)
\end{aligned}$$

As mentioned in the text,  $D_q^{(0)}(t)$  has been written as simply  $D_q(t)$  in Sec. 4.2, in the case of an initial CS.

## APPENDIX D

### Density matrix for a field mode interacting with a nonlinear medium

The Hamiltonian which describes the interaction of a single-mode field interacting with the nonlinear medium is given by [34]

$$H = \omega a^\dagger a + \omega_0 b^\dagger b + \gamma b^{\dagger 2} b^2 + g (a^\dagger b + b^\dagger a). \quad (\text{D.1})$$

The total number operator  $\mathbf{N}_{\text{tot}} = (a^\dagger a + b^\dagger b)$  commutes with  $H$ . We use  $N$  to denote its eigenvalues. The eigenstates  $|\psi_{Ns}\rangle$  of  $H$  are then labeled by integers  $N$  and  $s$ , where  $N = 0, 1, \dots$  *ad inf.* and  $s = 0, 1, \dots, N$  for a given value of  $N$ , as in Chapter 5, Sec. 5.2. These can be expanded in terms of the basis states  $|N-n\rangle_a \otimes |n\rangle_b \equiv |N-n; n\rangle$  as

$$|\psi_{Ns}\rangle = \sum_{n=0}^N d_n^{Ns} |N-n; n\rangle, \quad (\text{D.2})$$

with expansion coefficients

$$d_n^{Ns} = \langle N-n; n | \psi_{Ns} \rangle. \quad (\text{D.3})$$

The Hamiltonian in Eq. (D.1) can be represented in the basis  $|N-n; n\rangle$  as a real, symmetric, tridiagonal matrix. The eigenvalues  $\lambda_{Ns}$  and eigenstates  $|\psi_{Ns}\rangle$  of  $H$  can be found numerically using appropriate matrix algebra routines [73, 74].

The unitary time evolution operator is given by

$$U(t) = \sum_{N=0}^{\infty} \sum_{s=0}^N \exp(-i\lambda_{Ns}t) |\psi_{Ns}\rangle \langle \psi_{Ns}|. \quad (\text{D.4})$$

Hence, an initial state  $|\psi(0)\rangle$  evolves in time to the state

$$|\psi(t)\rangle = U(t) |\psi(0)\rangle = \sum_{N=0}^{\infty} \sum_{s=0}^N \exp(-i\lambda_{Ns}t) \langle\psi_{Ns}|\psi(0)\rangle |\psi_{Ns}\rangle. \quad (\text{D.5})$$

The corresponding time-dependent density matrix  $\rho(t)$  is

$$\rho(t) = \sum_{N=0}^{\infty} \sum_{s=0}^N \sum_{N'=0}^{\infty} \sum_{s'=0}^{N'} \exp[-i(\lambda_{Ns} - \lambda_{N's'})t] \langle\psi_{Ns}|\psi(0)\rangle \langle\psi(0)|\psi_{N's'}\rangle |\psi_{Ns}\rangle \langle\psi_{N's'}|. \quad (\text{D.6})$$

If the atomic oscillator is initially in the ground state  $|0\rangle_b$  and the field is in the Fock state  $|N\rangle_a$ , we have  $|\psi(0)\rangle = |N; 0\rangle$ , and

$$\rho(t) = \sum_{s=0}^N \sum_{s'=0}^N \exp[-i(\lambda_{Ns} - \lambda_{Ns'})t] \langle\psi_{Ns}|N; 0\rangle \langle N; 0|\psi_{Ns'}\rangle |\psi_{Ns}\rangle \langle\psi_{Ns'}|. \quad (\text{D.7})$$

(This expression is explicitly  $N$ -dependent, as expected.) Substituting for  $d_n^{Ns}$  from Eq. (D.3),  $\rho(t)$  can be re-expressed in the form

$$\rho(t) = \sum_{s=0}^N \sum_{s'=0}^N \exp[-i(\lambda_{Ns} - \lambda_{Ns'})t] d_0^{Ns} d_0^{Ns'} |\psi_{Ns}\rangle \langle\psi_{Ns'}|. \quad (\text{D.8})$$

Hence

$$\langle\psi_{Ml}|\rho(t)|\psi_{M'l'}\rangle = \exp[-i(\lambda_{Ml} - \lambda_{M'l'})t] d_0^{Ml} d_0^{M'l'} \delta_{MN} \delta_{NM'}. \quad (\text{D.9})$$

It is evident that  $\rho(t)$  is an  $(N+1)$ -dimensional diagonal matrix in this case.

For an initial state  $|(\alpha, m); 0\rangle$  we find, using Eq. (D.6),

$$\begin{aligned} \rho(t) &= \frac{e^{-\nu}}{m! L_m(-\nu)} \sum_{N=m}^{\infty} \sum_{s=0}^N \sum_{N'=m}^{\infty} \sum_{s'=0}^{N'} \frac{\sqrt{N! N'} (\alpha)^{N-m} (\alpha^*)^{N'-m}}{(N-m)! (N'-m)!} \\ &\times \exp[-i(\lambda_{Ns} - \lambda_{N's'})t] d_0^{Ns} d_0^{N's'} |\psi_{Ns}\rangle \langle\psi_{N's'}|, \end{aligned} \quad (\text{D.10})$$

where we have used Eq. (3.1) of Chapter 3, and expanded  $|\alpha, m\rangle$  in the Fock basis.

The corresponding matrix elements of the density matrix are given by

$$\begin{aligned} \langle \psi_{Ml} | \rho(t) | \psi_{M'l'} \rangle &= \frac{e^{-\nu}}{m! L_m(-\nu)} \frac{\sqrt{M! M'!} (\alpha)^{M-m} (\alpha^*)^{M'-m}}{(M-m)! (M'-m)!} \\ &\times \exp[-i(\lambda_{Ml} - \lambda_{M'l'}) t] d_0^{Ml} d_0^{M'l'}. \end{aligned} \quad (\text{D.11})$$

Here, and in the rest of this Appendix, it is understood that contributions from terms of the form  $1/(-n)!$ , where  $n$  is a positive integer, vanish.

The expectation values and higher moments of the quadrature variables  $\xi(t)$  and  $\eta(t)$ , defined in Eq. (5.9) of Chapter 5, can now be obtained numerically, using the above expressions for the density matrix and the matrix elements of the operators  $a$  and  $b$  in the basis  $|\psi_{Ns}\rangle$ . The latter are given by

$$\langle \psi_{Ns} | a | \psi_{N's'} \rangle = \sum_{n=0}^{N'} (N' - n)^{1/2} d_n^{Ns} d_n^{N's'} \delta_{N, N'-1} \quad (\text{D.12})$$

and

$$\langle \psi_{Ns} | b | \psi_{N's'} \rangle = \sum_{n=1}^{N'} n^{1/2} d_{n-1}^{Ns} d_n^{N's'} \delta_{N, N'-1}, \quad (\text{D.13})$$

respectively. As these are purely off-diagonal, and  $\rho(t)$  is diagonal for an initial state that is a direct product of Fock states, it follows that all the odd moments of  $\xi$  and  $\eta$  vanish identically for all  $t$ , as asserted in the text. This is no longer true for the other classes of initial states considered.

The time-dependent reduced density matrices  $\rho_k(t)$  ( $k = a, b$ ) are given by

$$\begin{aligned} \rho_a(t) &= \text{Tr}_b [\rho(t)] = \sum_{n=0}^{\infty} {}_b \langle n | \rho(t) | n \rangle_b, \\ \rho_b(t) &= \text{Tr}_a [\rho(t)] = \sum_{n=0}^{\infty} {}_a \langle n | \rho(t) | n \rangle_a. \end{aligned} \quad (\text{D.14})$$

Corresponding to an initial state  $|N; 0\rangle$ , these reduced density matrices  $\rho_k(t)$  take the form

$$\begin{aligned} \rho_a(t) &= \sum_{n=0}^N \sum_{s=0}^N \sum_{s'=0}^N \exp[-i(\lambda_{Ns} - \lambda_{Ns'}) t] \\ &\times d_0^{Ns} d_0^{N's'} d_n^{Ns} d_n^{N's'} |(N-n)\rangle_a {}_a \langle (N-n)| \end{aligned} \quad (\text{D.15})$$

and

$$\begin{aligned} \rho_b(t) &= \sum_{n=0}^N \sum_{s=0}^N \sum_{s'=0}^N \exp[-i(\lambda_{Ns} - \lambda_{Ns'}) t] \\ &\quad \times d_0^{Ns} d_0^{Ns'} d_{N-n}^{Ns} d_{N-n}^{Ns'} |(N-n)\rangle_b \langle(N-n)|. \end{aligned} \quad (\text{D.16})$$

Hence we have, in the Fock basis,

$${}_a \langle n | \rho_a(t) | n' \rangle_a = \sum_{s=0}^N \sum_{s'=0}^N \exp[-i(\lambda_{Ns} - \lambda_{Ns'}) t] d_0^{Ns} d_0^{Ns'} d_{N-n}^{Ns} d_{N-n'}^{Ns'} \delta_{nn'} \quad (\text{D.17})$$

and

$${}_b \langle n | \rho_b(t) | n' \rangle_b = \sum_{s=0}^N \sum_{s'=0}^N \exp[-i(\lambda_{Ns} - \lambda_{Ns'}) t] d_0^{Ns} d_0^{Ns'} d_n^{Ns} d_n^{Ns'} \delta_{nn'}. \quad (\text{D.18})$$

As before, these are explicitly  $N$ -dependent finite-dimensional matrices.

For an initial state  $|(\alpha, m); 0\rangle$  the expressions for  $\rho_k(t)$  are given by

$$\begin{aligned} \rho_a(t) &= \frac{e^{-\nu}}{m! L_m(-\nu)} \sum_{n=0}^{\infty} \sum_{N=N_{\min}}^{\infty} \sum_{s=0}^N \sum_{N'=N_{\min}}^{\infty} \sum_{s'=0}^{N'} \frac{\sqrt{N! N'} (\alpha)^{N-m} (\alpha^*)^{N'-m}}{(N-m)! (N'-m)!} \\ &\quad \times \exp[-i(\lambda_{Ns} - \lambda_{N's'}) t] d_0^{Ns} d_0^{N's'} d_n^{Ns} d_n^{N's'} |(N-n)\rangle_a \langle(N'-n)| \end{aligned} \quad (\text{D.19})$$

and

$$\begin{aligned} \rho_b(t) &= \frac{e^{-\nu}}{m! L_m(-\nu)} \sum_{n=0}^{\infty} \sum_{N=N_{\min}}^{\infty} \sum_{s=0}^N \sum_{N'=N_{\min}}^{\infty} \sum_{s'=0}^{N'} \frac{\sqrt{N! N'} (\alpha)^{N-m} (\alpha^*)^{N'-m}}{(N-m)! (N'-m)!} \\ &\quad \times \exp[-i(\lambda_{Ns} - \lambda_{N's'}) t] d_0^{Ns} d_0^{N's'} d_{N-n}^{Ns} d_{N'-n}^{N's'} |(N-n)\rangle_b \langle(N'-n)|, \end{aligned} \quad (\text{D.20})$$

where  $N_{\min} = \max(n, m)$ . These are infinite-dimensional matrices. The corre-

sponding matrix elements of  $\rho_k(t)$  in the Fock basis are given by

$$\begin{aligned}
{}_a\langle l | \rho_a(t) | l' \rangle_a &= \frac{e^{-\nu}}{m! L_m(-\nu)} \sum_{n_{\min}}^{\infty} \sum_{s=0}^{n+l} \sum_{s'=0}^{n+l'} \frac{\sqrt{(n+l)!(n+l')!} (\alpha)^{n+l-m} (\alpha^*)^{n+l'-m}}{(n+l-m)!(n+l'-m)!} \\
&\times \exp[-i(\lambda_{(n+l)s} - \lambda_{(n+l')s'}) t] d_0^{(n+l)s} d_0^{(n+l')s'} d_n^{(n+l)s} d_n^{(n+l')s'}
\end{aligned} \tag{D.21}$$

and

$$\begin{aligned}
{}_b\langle l | \rho_b(t) | l' \rangle_b &= \frac{e^{-\nu}}{m! L_m(-\nu)} \sum_{n_{\min}}^{\infty} \sum_{s=0}^{n+l} \sum_{s'=0}^{n+l'} \frac{\sqrt{(n+l)!(n+l')!} (\alpha)^{n+l-m} (\alpha^*)^{n+l'-m}}{(n+l-m)!(n+l'-m)!} \\
&\times \exp[-i(\lambda_{Ns} - \lambda_{N's'}) t] d_0^{(n+l)s} d_0^{(n+l')s'} d_l^{(n+l)s} d_{l'}^{(n+l')s'},
\end{aligned} \tag{D.22}$$

where  $n_{\min} = \max(m-l, m-l')$ .

All the reduced density matrices (with elements given by Eqs. (D.17), (D.18), (D.21) and (D.22)) are hermitian. They are diagonalized numerically, and their eigenvalues are used to compute the entropies  $S_k(t)$  and  $\delta_k(t)$  given by Eqs. (5.8). In the case of infinite-dimensional matrices, convergence in numerical computation is provided by the factorials in the denominators of the summands in the expressions derived above for the matrix elements. We use double precision arithmetic with an accuracy of 1 part in  $10^6$ . As mentioned in the text, we use the equality of  $\rho_a(t)$  and  $\rho_b(t)$  as one of the checks on the numerical computations. Other checks include the condition  $\rho^2(t) = \rho(t)$  for the density matrix of the total system, as we are only dealing with pure states.

## BIBLIOGRAPHY

- [1] F. Haake. *Quantum Signatures of Chaos*. Springer-Verlag, 1991.
- [2] M. V. Berry and M. Tabor. *Level clustering in the regular spectrum*. Proc. R. Soc. Lond. A **356**, 375–394 (1977).
- [3] M. V. Berry and M. Tabor. *Closed orbits and the regular bound spectrum*. Proc. R. Soc. Lond. A **349**, 101–123 (1976).
- [4] M. V. Berry. *Semiclassical mechanics of regular and irregular motion*. In *Chaotic Behavior of Deterministic Systems*, Editors G. Iooss, R. H. G. Helleman, and R. Stora, Les Houches Session XXXVI (1981), North-Holland, 1983.
- [5] A. Peres. *Stability of quantum motion in chaotic and regular systems*. Phys. Rev. A **30**, 1610–1615 (1984).
- [6] I. Sh. Averbukh and N. F. Perelman. *The dynamics of wave packets of highly-excited atoms and molecules*. Sov. Phys. Usp. **34**, 572–591 (1991).
- [7] R. Bluhm, V. A. Kostelecky and J. Porter. *The evolution and revival structure of localized quantum wave packets*. Am. J. Phys. **64**, 944–953 (1996).
- [8] R. W. Robinett. *Quantum wave packet revivals*. Phys. Rep. **392**, 1–119 (2004).
- [9] V. V. Dodonov. *‘Non-classical’ states in quantum optics: a ‘squeezed’ review of the first 75 years*. J. Opt. B: Quant. Semiclass. Opt. **4**, R1–R33 (2002).
- [10] J. B. Keller and W. Streifer. *Complex rays with an application to Gaussian beams*. J. Opt. Soc. Am. **61**, 40–43 (1971).
- [11] G. A. Deschamps. *Ray techniques in electromagnetics*. Proc. IEEE **60**, 1022–1035 (1972).
- [12] R. G. Littlejohn. *The semiclassical evolution of wave packets*. Phys. Rep. **138**, 193–291 (1986).
- [13] K. Tara, G.S Agarwal and S. Chaturvedi. *Production of Schrödinger macroscopic quantum-superposition states in a Kerr medium*. Phys. Rev. A **47**, 5024–5029 (1993).
- [14] M. Nauenberg, C. Stroud and J. Yeazell. *The classical limit of an atom*. Sci. Am. **270**, 44–49 (1994).
- [15] M. V. Berry and S. Klein. *Integer, fractional, and fractal Talbot effects*. J. Mod. Opt. **43**, 2139–2164 (1996).

- [16] K. Banaszek, K. Wódkiewicz and W. P. Schleich. *Fractional Talbot effects in phase space: A compact summation formula*. Opt. Exp. **2**, 169–172 (1998).
- [17] D. F. Styer. *The motion of wave packets through their expectation values and uncertainties*. Am. J. Phys. **58**, 742–744 (1990).
- [18] C. Sudheesh, S. Lakshmibala and V. Balakrishnan. *Manifestations of wave packet revivals in the moments of observables*. Phys. Lett. A **329**, 14–21 (2004).
- [19] I. Sh. Averbukh and N. F. Perelman. *Fractional revivals: Universality in the long-term evolution of quantum wave packets beyond the correspondence principle dynamics*. Phys. Lett. A **139**, 449–453 (1989).
- [20] J. Parker and C. R. Stroud Jr. *Coherence and decay of Rydberg wave Packets*. Phys. Rev. Lett. **56**, 716–719 (1986).
- [21] J. A. Yeazell, M. Mallalieu and C. R. Stroud Jr. *Observation of the collapse and revival of a Rydberg electronic wave packet*. Phys. Rev. Lett. **64**, 2007–2010 (1990).
- [22] J. A. Yeazell and C. R. Stroud Jr. *Observation of fractional revivals in the evolution of a Rydberg atomic wave packet*. Phys. Rev. A **43**, 5153–5156 (1991).
- [23] R. Tanas. *Nonclassical states of light propagating in Kerr media*. In *Theory of Non-classical States of Light*, Editors V. V. Dodonov and V. I. Man’Ko, Taylor & Francis, 2003.
- [24] N. J. Cerf, A. Ipe and X. Rottenberg. *Cloning of continuous quantum variables*. Phys. Rev. Lett. **85**, 1754–1757 (2000).
- [25] E. A. Shapiro, M. Spanner and M. Y. Ivanov. *Quantum logic approach to wave packet control*. Phys. Rev. Lett. **91**, 237901 (2003).
- [26] S. J. van Enk. *Entanglement capabilities in infinite dimensions: Multidimensional entangled coherent states*. Phys. Rev. Lett. **91**, 017902 (2003).
- [27] A. Zavatta, S. Viciani and M. Bellini. *Quantum-to-classical transition with single-photon-added coherent states of light*. Science **306**, 660–662 (2004).
- [28] C. Sudheesh, S. Lakshmibala and V. Balakrishnan. *Wave packet dynamics of photon-added coherent states*. Europhys. Lett. **71**, 744–750 (2005).
- [29] C. Sudheesh, S. Lakshmibala and V. Balakrishnan. *Squeezing and higher-order squeezing of photon-added coherent states propagating in a Kerr-like medium*. J. Opt. B: Quant. Semiclass. Opt. **7**, S728–S735 (2005).
- [30] A. Kenfack and K. Życzkowski. *Negativity of the Wigner function as an indicator of non-classicality*. J. Opt. B: Quant. Semiclass. Opt. **6**, 396–404 (2004).



- [31] A. I. Lvovsky, H. Hansen, T. Aichele, O. Benson, J. Mlynek and S. Schiller. *Quantum state reconstruction of the single-photon Fock state*. Phys. Rev. Lett. **87**, 050402 (2001).
- [32] L. Mandel and E. Wolf. *Optical Coherence and Quantum Optics*. Cambridge University Press, 1995.
- [33] L. Sanz, R. M. Angelo and K. Furuya. *Entanglement dynamics in a two-mode nonlinear bosonic Hamiltonian*. J. Phys. A **36**, 9737–9754 (2003).
- [34] G. S. Agarwal and R. R. Puri. *Collapse and revival phenomenon in the evolution of a resonant field in a Kerr-like medium*. Phys. Rev. A **39**, 2969–2977 (1989).
- [35] H. D. I. Abarbanel. *Analysis of Observed Chaotic Data*. Springer, 1995.
- [36] P. Grassberger and I. Procaccia. *Characterization of strange attractors*. Phys. Rev. Lett. **50**, 346–349 (1983).
- [37] A. M. Fraser and H. L. Swinney. *Independent coordinates for strange attractors from mutual information*. Phys. Rev. A **33**, 1134–1140 (1986).
- [38] C. Sudheesh, S. Lakshmibala and V. Balakrishnan. *Ergodicity properties of entangled two-mode states*. (Submitted for publication).
- [39] R. W. Robinett. *Visualizing the collapse and revival of wavepackets in the infinite square well using expectation values*. Am. J. Phys. **68**, 410–420 (2000).
- [40] M. A. Doncheski and R. W. Robinett. *Expectation value analysis of wave packet solutions for the quantum bouncer: Short-term classical and long-term revival behaviors*. Am. J. Phys. **69**, 1084–1090 (2001).
- [41] G. S. Agarwal and K. Tara. *Nonclassical properties of states generated by the excitations on a coherent state*. Phys. Rev. A **43**, 492–497 (1991).
- [42] M. Kitagawa and Y. Yamamoto. *Number-phase minimum-uncertainty state with reduced number uncertainty in a Kerr nonlinear interferometer*. Phys. Rev. A **34**, 3974–3988 (1986).
- [43] M. Greiner, O. Mandel, T. W. Hänsch and I. Bloch. *Collapse and revival of the matter wave field of a Bose-Einstein condensate*. Nature **419**, 51–54 (2002).
- [44] S. Sivakumar. *Photon-added coherent states as nonlinear coherent states*. J. Phys. A **32**, 3441–3447 (1999).
- [45] W. Schleich, R. J. Horowicz and S. Varro. *Bifurcation in the phase probability distribution of a highly squeezed state*. Phys. Rev. A **40**, 7405–7408 (1989).
- [46] D. F. Walls and P. Zoller. *Reduced quantum fluctuations in resonance fluorescence*. Phys. Rev. Lett. **47**, 709–711 (1981).

- [47] D. F. Walls. *Squeezed states of light*. Nature **306**, 141–146 (1983).
- [48] R. Loudon and P. L. Knight. *Squeezed light*. J. Mod. Opt. **34**, 709–759 (1987).
- [49] C. K. Hong and L. Mandel. *Generation of higher-order squeezing of quantum electromagnetic fields*. Phys. Rev. A **32**, 974–982 (1985).
- [50] M. Hillery. *Amplitude-squared squeezing of the electromagnetic field*. Phys. Rev. A **36**, 3796–3802 (1987).
- [51] Z. Zhang, L. Xu, J. Chai and F. Li. *A new kind of higher-order squeezing of radiation field*. Phys. Lett. A **150**, 27–30 (1990).
- [52] V. V. Dodonov, M. A. Marchiolli, Y. A. Korennoy, V. I. Man’ko and Y. A. Moukhin. *Dynamical squeezing of photon-added coherent states*. Phys. Rev. A **58**, 4087–4094 (1998).
- [53] B. Yurke and D. Stoler. *Generating quantum mechanical superpositions of macroscopically distinguishable states via amplitude dispersion*. Phys. Rev. Lett **57**, 13–16 (1986).
- [54] C. Gerry and S. Rodrigues. *Higher-order squeezing from an anharmonic oscillator*. Phys. Rev. A **35**, 4440–4442 (1987).
- [55] S.-D. Du and C.-D. Gong. *Higher-order squeezing for the quantized light field:  $K$ th-power amplitude squeezing*. Phys. Rev. A **48**, 2198–2212 (1993).
- [56] J. Perina. *Quantum Statistics of Linear and Nonlinear Optical Phenomena*. Reidel, 1984.
- [57] M. Brune, S. Haroche, J. M. Raimond, L. Davidovich and N. Zagury. *Manipulation of photons in a cavity by dispersive atom-field coupling: Quantum-nondemolition measurements and generation of “Schrödinger cat” states*. Phys. Rev. A **45**, 5193–5214 (1992).
- [58] C. C. Gerry and P. L. Knight. *Introductory Quantum Optics*. Cambridge University Press, 2005.
- [59] G. Breitenbach and S. Schiller. *Homodyne tomography of classical and non-classical light*. J. Mod. Opt. **44**, 2207–2225 (1997).
- [60] C. Sudheesh, S. Lakshmi-bala and V. Balakrishnan. *Entanglement dynamics in the propagation of a single-mode field through a nonlinear medium*. Topical Conference on Atomic, Molecular and Optical Physics, Indian Association for the Cultivation of Science, Kolkata, December 2005.
- [61] F. Takens. *Detecting strange attractors in turbulence*. In *Dynamical Systems and Turbulence*, Editors D. Rand and L. S. Young, Springer, 1981.
- [62] M. T. Rosenstein, J. J. Collins and C. J. D. Luca. *A practical method for calculating largest Lyapunov exponents from small data sets*. Physica D **65**, 117–134 (1993).

- [63] H. Kantz. *A robust method to estimate the maximal Lyapunov exponent of a time series*. Phys. Lett. A **185**, 77–87 (1994).
- [64] P. Bocchieri and A. Loinger. *Quantum recurrence theorem*. Phys. Rev. **107**, 337–338 (1957).
- [65] T. Hogg and B. A. Huberman. *Recurrence phenomena in quantum dynamics*. Phys. Rev. Lett. **48**, 711–714 (1982).
- [66] S. Seshadri, S. Lakshmibala and V. Balakrishnan. *Quantum revivals, geometric phases and circle map recurrences*. Phys. Lett. A **256**, 15–19 (1999).
- [67] E. Fermi, J. Pasta and S. Ulam. *Studies in nonlinear problems*. In *Collected Papers of Enrico Fermi*, Vol. II, Editor E. Segrè, University of Chicago Press, 1965.
- [68] V. A. Ermoshin, M. Erdmann and V. Engel. *Fermi-Pasta-Ulam recurrences, normal modes and wave-packet revivals*. Chem. Phys. Lett. **356**, 29–35 (2002).
- [69] L. E. Ballentine, Y. Yang and J. P. Zibin. *Inadequacy of Ehrenfest’s theorem to characterize the classical regime*. Phys. Rev. A **50**, 2854–2859 (1994).
- [70] S. Habib, K. Jacobs and K. Shizume. *The quantum emergence of chaos*. arXiv: quant-ph/0412159; Phys. Rev. Lett. (to appear) (2005).
- [71] W. P. Schleich. *Quantum Optics in Phase Space*. Wiley-VCH, 2001.
- [72] I. S. Gradshteyn and I. M. Ryzhik. *Table of Integrals, Series, and Products*. Academic Press, 1980.
- [73] W. H. Press, S. A. Teukolsky, W. T. Vetterling and B. P. Flannery. *Numerical Recipes in C*. Cambridge University Press, pp. 475-481, 2001.
- [74] M. Galassi, J. Davies, J. Theiler, B. Gough, G. Jungman, M. Booth and F. Rossi. *GNU Scientific Library*. GNU Software, 2005.

# LIST OF PAPERS BASED ON THESIS

## Papers in refereed journals

1. C. Sudheesh, S. Lakshmibala and V. Balakrishnan,  
*Manifestations of wave packet revivals in the moments of observables.*  
Phys. Lett. A **329**, 14-21 (2004).
2. C. Sudheesh, S. Lakshmibala and V. Balakrishnan,  
*Wave packet dynamics of photon-added coherent states.*  
Europhys. Lett. **71**, 744-750 (2005).
3. C. Sudheesh, S. Lakshmibala and V. Balakrishnan,  
*Squeezing and higher-order squeezing of photon-added coherent states propagating in a Kerr-like medium.*  
J. Opt. B: Quant. Semiclass. Opt. **7**, S728-S735 (2005).
4. C. Sudheesh, S. Lakshmibala and V. Balakrishnan,  
*Wave packet dynamics of entangled two-mode states.*  
J. Phys. B: At. Mol. Opt. Phys. **39**, 3345-3359 (2006).

## Presentations in conferences

1. C. Sudheesh, S. Lakshmibala and V. Balakrishnan,  
*Dynamical squeezing and higher-order squeezing in wave packet propagation in a Kerr-like medium.*  
ICSSUR'05: 9th International Conference on Squeezed States and Uncertainty Relations, Besançon, France, May 2005.
2. C. Sudheesh, S. Lakshmibala and V. Balakrishnan,  
*Dynamics of a wave packet governed by a nonlinear quantum Hamiltonian: Classical correspondence.*  
II National Conference on Nonlinear Systems and Dynamics, Aligarh Muslim University, Aligarh, February 2005.
3. C. Sudheesh, S. Lakshmibala and V. Balakrishnan,  
*Entanglement dynamics in the propagation of a single-mode field through a nonlinear medium.*  
Topical Conference on Atomic, Molecular and Optical Physics, Indian Association for the Cultivation of Science, Kolkata, December 2005.

## Submitted for publication

C. Sudheesh, S. Lakshmibala and V. Balakrishnan,

*Ergodicity properties of quantum expectation values in entangled two-mode states, arXiv:0706.2954 (2007).*

# CURRICULUM VITAE

**Name** : C. Sudheesh  
**Date of Birth** : 25.05.1977  
**Nationality** : Indian  
**Permanent Address** : Chethil House, Iringal PO  
Vadakara, Kozhikode 673 521.  
**Present Address** : Postdoctoral Fellow  
Theoretical Physics Division  
Physical Research Laboratory  
Ahmedabad 380 009.  
**Email** : chethil.sudheesh@gmail.com

## Academic Record:

- B.Sc (Physics), I Class (1st Rank in College), Govt. Madappally College, University of Calicut, (1997).
- M.Sc (Physics), Indian Institute of Technology, Madras (2001).
- Qualified in GATE (Physics), 97.71 percentile (2001).
- Qualified for Lecturership in the CSIR-UGC National Eligibility Test (NET), (2001).

## Conferences attended:

- II National Conference on Nonlinear Systems and Dynamics, Aligarh Muslim University, Aligarh, February 2005.
- ICSSUR'05: 9th International Conference on Squeezed States and Uncertainty Relations, Besançon, France, May 2005.
- III National Conference on Nonlinear Systems and Dynamics, Ramanujan Institute for Advanced Study in Mathematics, University of Madras, Chennai, February 2006.

**Schools attended:**

- IV School on Physics of Beams, Centre for Advanced Technology, Indore (27 Dec. 1999 to 7 Jan. 2000).
- SERC School on Quantum Information and Quantum Optics, Physical Research Laboratory, Ahmedabad (February 1-14, 2004).
- SERC School on Statistical Physics, Tata Institute of Fundamental Research, Mumbai (February 16-28, 2004).